Refining molecular stratigraphy through mass spectrometry imaging of sediments at sub-millimeter resolution

Dissertation
zur Erlangung des Doktorgrades
der Naturwissenschaften
- Dr. rer. nat. -

Am Fachbereich Geowissenschaften der
Universität Bremen

vorgelegt von

Susanne Alfken

Bremen
Oktober 2019

Diese Doktorarbeit wurde in der Zeit von Januar 2016 bis Oktober 2019 in der Arbeitsgruppe Organische Geochemie am MARUM – Zentrum für Marine Umweltwissenschaften und Fachbereich Geowissenschaften der Universität Bremen angefertigt.

This doctoral thesis was conducted from January 2016 to October 2019 in the working group Organic Geochemistry at MARUM – Center for Marine Environmental Sciences and faculty of Geosciences of the University of Bremen.

Gutachter/Reviewers:

Prof. Dr. Kai-Uwe Hinrichs

Prof. Dr. Anna Nele Meckler

CONTENTS

ABSTRACT

Lipid biomarkers are unique recorders of past climate variability. Deriving from membrane lipids of microorganisms that once inhabited the water column they reflect the prevailing conditions in which they developed. Retrieval of these molecular fossils from the sedimentary record with an established age model is a powerful tool for the reconstruction of paleoenvironments. A major constraint to the conventional extraction-based approach of molecular stratigraphy is the high sample requirement, which limits the spatial resolution to the centimeter scale, limiting the resolution in the time domain to decades or more. However, abrupt and drastic environmental transitions as well as high-frequency climate oscillations operate on shorter time-scales and are recorded within the sedimentary matrix at finer scales.

In this dissertation, sedimentary mass spectrometry imaging (MSI) has been established as a novel, extraction-free technique that enables detailed analysis of lipid biomarker distributions on intact sediment surfaces, and thereby initiates the exploration of micrometer-scale (subannual) molecular stratigraphy.

In a first step, sample preparation of sediments, with the option of a complementary elemental mapping, as well as guidelines for successful MSI of a set of molecular biomarkers were defined. MSI strongly benefits from cutting the intact sediment samples into sequential micrometer-thin slices, ideally suited for multiproxy analyses. The required stabilization of the sediment is enabled by embedding of the sample in MSI-compatible media, i.e. a mixture of gelatin and carboxymethyl cellulose. Besides showing that high concentrations of the target compounds facilitate MSI, the evaluation of the influence of artificial matrices and optimization of MS settings revealed that ionization efficiency and analytical quality of target molecules are generally promoted by the natural sedimentary matrix and benefits from narrow m/z ranges.

Applied to modern varved sediments from the Santa Barbara Basin (SBB), off southern California, MSI provided monthly-resolved records of two molecular proxies used for sea surface temperature (SST) reconstruction. The comparison of the high-resolution sedimentary proxy records to 25 years of seasonally measured water column data revealed new insights into the drivers of the proxy signals. The $U^{K'}_{37}$, a proxy derived from the unsaturation degree of long-chain alkenones from haptophyte algae, sensitively recorded the annual SST cycle, while the physiological response to variable nutrient availability dampened the absolute SST amplitude. Actual SST was over- (under-) estimated by the $U^{K'}_{37}$ when surface water nitrate concentrations were above (below) ~2 µmol/L. The CCaT and TEX^{L}_{86} ratios, based on the degree of cyclization of glycerol dibiphytanyl glycerol tetraethers from planktonic Thaumarchaeota, correlated with subsurface oxygen, salinity and nutrient concentrations indicative of the low-frequency upwelling

variability in the California Current System (CCS). Taking into account the results from previous culture studies, these observations cannot be attributed to a physiological response to salinity or oxygen concentrations but are more likely related to the impact of nutrient availability on thaumarchaeal growth rates.

Furthermore, the MSI-based analysis of a ~30 cm SBB record provided high-resolution reconstruction of 20th century variation in SST, upwelling strength and bottom water redox conditions off the southern Californian coast. The $U^{K'}_{37}$ overall reliably recorded subannual SST variation and its interannual modulation by El Niño Southern Oscillation. The ~1 °C temperature increase in the CCS reported by other authors was not detected by this proxy, potentially due to a nutrient effect as described above. Changing physical properties that accompanied the 20th century CCS warming may have led to a lower nutrient availability in the ocean surface and thus to cold-biased alkenone temperatures. The CCaT proxy provided evidence for a composite influence of large-scale Pacific climate oscillations on subsurface upwelling variability. In combination with the redox-sensitive C_{29} stanol/stenol ratio, it also revealed the changing dependencies of upwelling strength and bottom water redox conditions due to a mid-1970s regime shift in the CCS. Before this regime shift, the ventilation effect during strong upwelling was driving the bottom water oxygen content. Afterwards, due to the increasing stratification of the water column, this effect was repealed and replaced by the upwelling-induced productivity increase and subsequent oxygen-consuming remineralization of organic matter.

This thesis emphasizes the potential of MSI to explore a new level of molecular stratigraphy and to deliver unprecedented insights into the information stored in lipid biomarkers.

ZUSAMMENFASSUNG

Lipidbiomarker sind einzigartige Erfasser von vergangenen Klimaschwankungen. Hervorgehend aus Membranlipiden von Mikroorganismen, die zuvor in der Wassersäule lebten, spiegeln sie die vorherrschenden Bedingungen wider, unter denen sie gebildet wurden. Die Entnahme dieser molekularen Fossilien aus datierten Sedimenten ist eine wirkungsvolle Methode zur Rekonstruktion von Paläoumweltbedingungen. Eine deutliche Einschränkung der konventionellen extraktionsbasierten molekularen Stratigraphie stellt der hohe Probenbedarf dar. Hierdurch wird die räumliche Auflösung auf mehrere Zentimeter, und somit die zeitliche Auflösung auf Jahrzehnte oder mehr begrenzt. Abrupte und einschneidende Veränderungen der Umweltbedingungen, sowie hochfrequente Klimaschwankungen erfolgen jedoch auf kürzeren Zeitskalen und werden innerhalb der Sedimentmatrix in feineren Maßstäben erfasst.

In dieser Dissertation wurde die bildgebende Massenspektrometrie (MSI) als neuartige, extraktionsfreie Technik etabliert, mit der eine detaillierte Analyse der Verteilung von Lipidbiomarkern auf intakten Sedimentoberflächen ermöglicht wird, und damit einen Weg zur Erforschung der mikrometergroßen (subjährlichen) molekularen Stratigraphie eröffnet.

In einem ersten Schritt wurde die Probenvorbereitung von Sedimenten mit der Option einer komplementären Elementkartierung, sowie Leitlinien für die erfolgreiche MSI einer Reihe von molekularen Biomarkern definiert. Die Präparation der intakten Sedimente in aufeinanderfolgende mikrometerdünne Schnitte begünstigt MSI und ist ideal für Multiproxyanalysen geeignet. Das Sediment wird durch die Einbettung der Probe in eine MSI-kompatible Mischung aus Gelatine und Carboxymethylcellulose stabilisiert. Hohe Konzentrationen der Zielkomponenten unterstützen die MSI. Zudem ergab die Evaluierung des Einflusses von künstlichen Matrizen und die Optimierung der MS-Einstellungen, dass die Ionisationseffizienz und die analytische Qualität grundsätzlich durch die natürlich vorhandene Sedimentmatrix und von schmalen m/z-Bereichen gefördert wird.

Angewandt auf rezente, gewarvte Sedimente aus dem vor der Küste Südkaliforniens liegenden Santa Barbara Becken (SBB), lieferte MSI monatlich aufgelöste Datensätze von zwei molekularen Proxies, die zur Rekonstruktion der Meeresoberflächentemperatur (SST) verwendet werden. Der Vergleich der hochaufgelösten Proxydaten aus dem Sediment mit 25 Jahren saisonal gemessenen Daten aus der Wassersäule offenbarte neue Erkenntnisse über die Einflussfaktoren der Proxysignale. Der $U_{37}^{K'}$, ein Proxy, der sich aus dem Grad der Unsättigung langkettiger Alkenone aus Haptophyten ableitet, zeichnet deutlich den jährlichen SST-Zyklus auf. Die physiologische Reaktion auf eine variierende Verfügbarkeit von Nährstoffen schwächt die absolute Amplitude der SST jedoch ab. Die tatsächliche SST wurde durch den $U_{37}^{K'}$ zu hoch (zu niedrig) wiedergegeben,

wenn die Nitratkonzentrationen im Oberflächenwasser mehr (weniger) als ~2 µmol/L betrugen. Der CCaT und der TEX_{86}^{L} – Verhältnisse, die auf dem Zyklisierungsgrad von Glyzerol Dibiphytanyl Glyzerol Tetraethern aus planktonischen Thaumarchaeen basieren – korrelierten mit dem Sauerstoff- und Salzgehalt sowie mit Nährstoffkonzentrationen tieferer Wasserschichten, welche auf eine niederfrequente Variabilität des Auftriebes im kalifornischen Meeresstromsystem (CCS) hinweisen. In Anbetracht der Ergebnisse vorangegangener Kultivierungsstudien sind die vorliegenden Ergebnisse nicht auf eine physiologische Reaktion auf Salzgehalte oder Sauerstoffkonzentrationen zurückzuführen, sondern stehen eher im Zusammenhang mit dem Einfluss der Nährstoffverfügbarkeit auf die Wachstumsraten von Thaumarchaeen.

Die MSI-basierte Analyse eines ~30 cm Sedimentkernes aus dem SBB ermöglichte zudem eine hochauflösende Rekonstruktion von Schwankungen in SST, der Auftriebskraft und von Redoxbedingungen im Bodenwasser vor der südkalifornischen Küste während des 20. Jahrhunderts. Insgesamt erfasste der $U_{37}^{K'}$ zuverlässig die subjährliche SST-Veränderung und deren interjährliche Beeinflussung durch die El Niño Southern Oscillation. Der von anderen Autoren berichtete Temperaturanstieg von ~1 °C im CCS wurde von diesem Proxy nicht nachgewiesen, was möglicherweise auf einen, zuvor beschriebenen, Nährstoffeinfluss zurückzuführen ist. Veränderungen der physikalischen Eigenschaften, die mit der Erwärmung des CCS im 20. Jahrhundert einhergingen, können zu einer geringeren Nährstoffverfügbarkeit an der Meeresoberfläche und damit zu einer niedrigeren Alkenontemperatur geführt haben. Der CCaT-Proxy zeigte, dass die Variabilität des Auftriebes in tieferen Wasserschichten von einer Kombination aus großskaligen pazifischen Klimaoszillationen beeinflusst ist. Zusammen mit dem redoxsensitiven C_{29} stanol/stenol-Verhältnis wurde auch die sich ändernde Abhängigkeit von Auftriebsstärke und Bodenwasser-Redoxbedingungen durch eine Mitte der 70er Jahre stattfindende Regimeänderung im CCS aufgezeigt. Vor dieser Regimeänderung hat die Ventilationswirkung von starkem Auftrieb den Sauerstoffgehalt des Bodenwassers beeinflusst. Die zunehmende Stratifizierung der Wassersäule hat diesen Effekt aufgehoben und durch die vom Auftrieb geförderte Steigerung der Produktivität und die anschließende sauerstoffzehrende Remineralisierung der organischen Materie ersetzt.

Diese Doktorarbeit verdeutlicht das erhebliche Potenzial von MSI, die molekulare Stratigraphie auf eine neue Ebene zu bringen und unvergleichliche Einblicke in die gespeicherten Informationen in Lipidbiomarkern zu liefern.

ACKNOWLEDGMENTS

First of all, I want to thank Kai-Uwe Hinrichs for giving me the opportunity of doing my PhD on this exceptional topic and for the great support during all these years. Your motivating enthusiasm for science and encouragement helped me in many moments. A special thanks to Arndt Schimmelmann for being on my thesis committee and supporting me on all my projects with his expert knowledge on the Santa Barbara Basin. I would like to thank Anna Nele Meckler for agreeing to review my thesis, I hope you find it a worthwhile read.

Lars, thanking you for what you have meant during this time is almost impossible. I could not have dreamt of a better support. You were always there when I needed your advice or when I just wanted to chat. Your incredible serenity and realistic view of things has stopped me from panicking every now and then. I am forever grateful to you!

Jenny, besides being the world´s best technician you are also a dear friend I would not want to miss. Thank you for all the support and the sporty breaks.

I also want to thank the other members of the *ZOOMECULAR* team Julius, Heidi, Verena, Marcus, Igor and Tiffany for building a great scientific framework and providing such a wonderful and supporting atmosphere. I have been fortunate to be part of this team as well as the entire Hinrichs Lab with outstanding colleagues who have accompanied me for many years. Thank you, Flo, Xavi, Sarah, Martin, Qing Zeng, Bernhard, Vicente, Rishi, Friederike, Yvonne, Evert, Jonas, Min, Sandra, Rebecca, Niro, Olli, Andreas, Lukas, Janina G., Janina B., Lea, Sebastian, Frederik and Ola. With this I also like to say thanks to all my office mates during the past years. Thank you Thommy, Weichau, Stani, Igor, Charlotte and Kai for providing a great time and for enduring all my moods and occasional swearing. A particular thanks to Marcus for convincing me to join the group as a student assistant in autumn 2010. This moment turned out to be life-changing on many levels.

During my PhD I also strongly appreciated the great support from Jürgen Pätzold with core scanning and X-ray photography and his admirable knowledge on paleoclimatology. Furthermore, I am very thankful for the immense help from Daniel, Felix and HoangAnh of the MARUM workshop, who realized all my strange ideas for unusual sampling devices. Special thanks goes also to Matthias Witt, Corinna Henkel and Jens Fuchser from Bruker Daltonik for all the intensive help with MALDI-FT-ICR-MS and valuable ideas for sample preparation.

Finally, I want to thank my all friends and my family for their support and understanding in all aspects of life.

Mama und Papa, danke, dass ich mich immer auf euch verlassen kann. Ich kann mir keine besseren Eltern wünschen. Sonja und Christopher, danke für all eure Unterstützung und für Henner. Edith und Wilfried, ihr seid die besten zweiten Eltern auf der Welt. Und Matthias, für alles, für immer und dich.

LIST OF ABBREVIATIONS

µ-XRF	micro-X-ray fluorescence
AOM	Anaerobic oxidation of methane
APCI/MS	Atmospheric pressure chemical ionization mass spectrometry
BC	Box core
BHP	Bacteriohopanepolyol
BSTFA	Bis-(trimethylsilyl)trifluoroacetamide
BW	Bottom water
CalCOFI	Californian Oceanic Fisheries Investigation
CASI	Continuous accumulation of selected ions
CCaT	Crenarchaeol-caldarchaeol tetraether index
CCS	California current system
CMC	Carboxymethyl cellulose
DCM	Dichloromethane
DHB	2,5-dihydroxybenzoic acid
ENSO	El Niño Southern Oscillation
ERSST	Extended reconstructed sea surface temperature
FT-ICR-MS	Fourier transform-ion cyclotron resonance-mass spectrometry
GC	Gas chromatography
GDGT	Glycerol dibiphytanyl glycerol tetraether
GTGT	Glycerol trialkyl glycerol tetraether
HCCA	α-cyano-4-hydroxycinnamic acid
HPLC	High performance liquid chromatography
ITO	Indium-tin oxide
m/z	Mass to charge ratio
MALDI	Matrix-assisted laser/desorption ionization
MeOH	Methanol
MS	Mass spectrometry
MSI	Mass spectrometry imaging
NaTFA	Sodium trifluoroacetate
NOAA	National Oceanic and Atmospheric Administration
NPGO	North Pacific Gyre Oscillation
OCT	Tissue Tek optimal cutting temperature compound
OMZ	Oxygen minimum zones
PAHs	Polyaromatic hydrocarbons
PDO	Pacific Decadal Oscillation
qToF-MS	Quadrupole time-of-flight tandem mass spectrometer
RF	Radio frequency
SBB	Santa Barbara Basin

SNR	Signal to noise ratio
SST	Sea surface temperature
TEX_{86}	Tetraether index of tetraethers consisting 86 carbon atoms
TEX_{86}^{L}	TEX index for low temperatures
TLE	Total lipid extract
TMS	Trimethylsilyl
ToF-SIMS	Time-of-flight secondary ion mass spectrometry
$U_{37}^{K'}$	Alkenone unsaturation index
wt%	Weight percent
XRF	X-ray fluorescence

CHAPTER I

INTRODUCTION

I. General introduction

This introduction provides an overview on the importance of high-resolution climate reconstruction and the need for improving the current method of molecular stratigraphy in terms of temporal resolution and signal understanding. The conventional concept of lipid biomarker analysis and its use for paleoclimatology is discussed and how the approach of extraction-free, spatially resolved biomarker analysis has the potential to overcome the limitations of the established methods. Additionally, this section introduces the characteristics of sedimentary archives suitable for high-resolution climate reconstruction with special focus on the Santa Barbara Basin, off Southern California.

I.1. Molecular stratigraphy as a tool for understanding past climate

Understanding the processes and effects of past climate variability is essential for assessing the dynamic variations and future changes of the climate system. The instrumental and historical record can only provide a glimpse into this variability, making it difficult to assess whether observed changes are part of natural re-occurring cycles or abrupt singular events. Extension of the climate record beyond this time can be provided by natural archives such as tree rings, corals, speleothems, ice cores and lacustrine or marine sediments. Given the nature of these different archives, traces of climate change operating on interannual to millennial time-scales are recorded. Whereas some information on climate variability is visibly accessible by e.g. annual growth structures in tree rings and corals, dust layers within glacial ice, or annual lamina couplets in varved sediments, other insights are archived on the molecular level.

These molecular tracers can be organic molecules originating from membrane lipid of pro- and eukaryotes that provide information on their biological origin and the habitat conditions they were produced in. The rather labile intact polar membrane lipids can provide insights into active biochemical processes such as the anaerobic oxidation of methane (AOM, Hinrichs et al., 1999; Boetius et al., 2000) or ammonium (annamox, Kuypers et al., 2003), as well as information on the composition of the microbial community within the deep subseafloor biosphere (e.g., Biddle et al., 2006; Lipp et al., 2008) and the water column (Schubotz et al., 2009). Whereas the polar headgroup of the intact membrane lipid is rapidly lost by hydrolytic cleavage after cell death (White et al., 1979; Harvey et al., 1986) the apolar core of the lipid is preserved as a molecular fossil in the sediment over geological time scales and can be used as a molecular tool for the reconstruction of past environmental conditions.

The term “molecular stratigraphy” was first introduced 1975 by Reed and Mankiewicz and gained in importance for paleoclimate studies when Brassell and colleagues applied this “new tool for climatic assessment” in 1986. The concept of molecular stratigraphy involves the analyses of lipid biomarkers in solvent extracts of samples from sedimentary records with an implemented age model. This approach has provided insights into past sea surface temperature (SST) variations associated with climatic changes during the late Holocene (Sepúlveda et al., 2009a), quaternary glacial terminations (Eglinton et al., 1992), or during the Paleocene/Eocene thermal maximum (Sluijs et al., 2006). Besides SST variation, molecular stratigraphic records have been used to inform on atmospheric carbon dioxide concentrations during the cretaceous (Kuypers et al., 1999) and the recovery of marine primary productivity after the mass extinction event at the Cretaceous-Paleogene boundary (Sepúlveda et al., 2009b).

I.2. Lipid biomarkers and their use for paleoclimatology

The use of lipid biomarkers as indicators of past climate involves the basic principle that these compounds record specific information from their biological source, the habitat conditions they were originally produced in, or the degradational milieu they were deposited in. Analyses of lipid biomarkers from sediment records with favorable conditions for a good preservation of the organic matter can be used to trace back the parameters of the past environments, such as the ecology of marine primary producers, different sources of the organic matter (marine versus terrestrial), habitat condition (temperature, water depth, oxygenation) of the source organism or fluctuations in the redox condition in the depositional setting. In the following, a selection of lipid biomarkers and their application in paleoclimatology are introduced, with the focus on the compounds used in this thesis.

Steroidal alcohols (sterols) are typical biomarkers for eukaryotes and the distribution of the C_{27}, C_{28} and C_{29} compounds in the sediment has been used to obtain information on the source of the organic matter, by using the simplified scheme of aquatic plants as the major source of C_{27} sterols, whereas higher land plants typically produce C_{29} compounds and C_{28} contributes from both sources to the sedimentary signal (Huang and Meinschein, 1976, 1979). The reduction of Δ^5-stenol to 5α(H)-stanols through microbial conversion under anoxic conditions (Rosenfeld and Hellmann, 1971; Eyssen et al., 1973) can be expressed in stanol/stenol ratio and serve as a proxy for redox conditions in the depositional setting (Nishimura and Koyama, 1977; Wakeham, 1989).

The observation that haptophyte algae adapt to changing temperature in their habitat, the ocean surface, by regulating the unsaturation degree in the long-chain alkenones is the basis of the SST proxy $U_{37}^{K'}$ (Brassell et al., 1986; Prahl and Wakeham, 1987, Table 1). The dominant influence of growth temperature on the proportion of di-unsaturated to tri-unsaturated C_{37} alkenones has been confirmed by different culture studies (e.g., Prahl et al., 1988; Marlowe et al., 1990; Volkman et al., 1995; Conte et al., 1998) and in environmental studies of surface waters (e.g., Prahl and Wakeham, 1987; Conte et al., 2001; Conte et al., 2006). Even though temperature is dominating for the sedimentary $U_{37}^{K'}$ signal, genetic and physiological factors (Conte et al., 1998), as well as seasonality (Rosell-Melé and Prahl, 2013) and dissolved nutrients (Conte et al., 1998; Epstein et al., 1998; Prahl et al., 2003) can have some influence on the alkenone unsaturation ratio.

Another widely applied SST proxy originates from the core isoprenoidal glycerol dibiphytanyl glycerol tetraether (GDGTs) of Archaea. The main source of GDGTs in marine sediments is thought to be ammonia-oxidizing planktonic Archaea of the phylum Thaumarchaeota (Brochier-Armanet et al., 2008; Spang et al., 2010). These autotrophic microorganisms oxidize ammonium (NH_4^+) to nitrite (NO_2^-), catalyzed by the archaeal ammonia monooxygenase enzyme

(Könneke et al., 2005). They account for up to 20% of the total picoplankton in the ocean (Karner et al., 2001), with highest abundances near the NO_2^- maximum below the photic zone (e.g., Massana et al., 1997; Murray et al., 1999; Francis et al., 2005; Santoro et al., 2010; Smith et al., 2016).

GDGTs produced by Thaumarchaeota contain from zero up to four cyclopentyl moieties (GDGT-0 to GDGT-4) and, in the case of crenarchaeol, four cyclopentane rings with one additional cyclohexane ring (Sinninghe Damsté et al., 2002, Table 1). A related compound to crenarchaeol is its isomer (Liu et al., 2018; Sinninghe Damsté et al., 2018), which is generally referred to as cren' (Sinninghe Damsté et al., 2002). Their ubiquity and persistence in the sedimentary record over geological time scales holds a strong potential of these lipids for paleoclimate studies (Kuypers et al., 2001; Schouten et al., 2003). The observation that surface sediments from warm and cold regions exhibit different GDGT distributions, with a positive correlation between the number of rings with SST, resulted in the TEX_{86} ratio (TetraEther indeX of tetraethers containing 86 carbon atoms, Schouten et al., 2002) its derivative for colder regions (TEX_{86}^L; Kim et al., 2010), or the CCaT, a proxy based on the ratio of the two major GDGTs (Wörmer et al., 2014).

Even though culture experiments showed that Thaumarchaeota indeed adapt to increasing growth temperature by an increase in cyclization in their GDGT membrane lipids (Wuchter et al., 2004; Elling et al., 2015), the sole dependency to SST has been questioned due to contrary results of TEX_{86} derived temperatures with other SST proxies and actual SSTs (Lee et al., 2008; Leider et al., 2010; Rommerskirchen et al., 2011; Mollenhauer et al., 2015). More recent findings from culture experiments can partly explain the observed mismatches as changes in cyclization have been observed with growth stage (Elling et al., 2014), oxygen concentrations (Qin et al., 2015), taxonomic affiliation of the Thaumarchaeon (Elling et al., 2015) and nutrient availability (Hurley et al., 2016; Evans et al., 2018).

Table 1: *Selection of molecular biomarkers (used in this thesis) and their use for paleoenvironmental reconstruction.*

Compound class	**Source organism**	**Indicator for; *proxy***	**Selected references**
Long-chain alkenones	Haptophyte algae	Sea surface temperature; $U_{37}^{K'}$	Brassell et al. (1986); Prahl and Wakeham (1987)
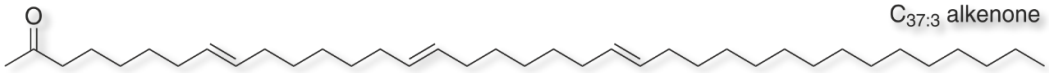			
Isoprenoidal glycerol dibiphytanyl glycerol tetraether (GDGTs)	Planktonic archaea	Sea surface temperature; TEX_{86}, $CCaT$	Schouten et al. (2002); Wörmer et al. (2014)
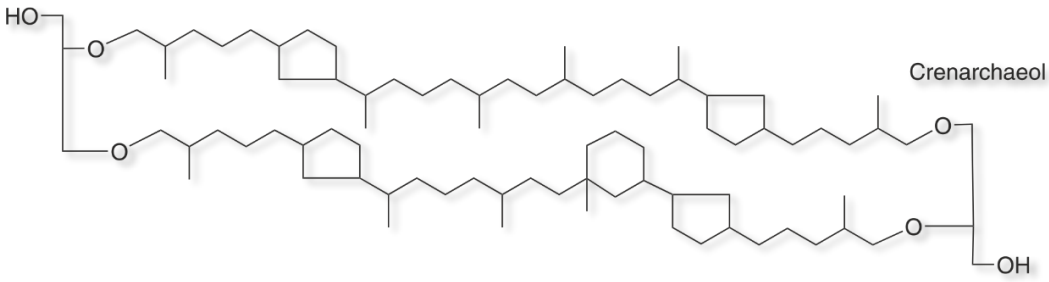			
Sterols	Marine algae, land plants	Redox conditions; *5α(H)-stanol/Δ5-stenol* Community structure	Wakeham (1989) Huang and Meinschein (1979); Volkman et al. (1998)
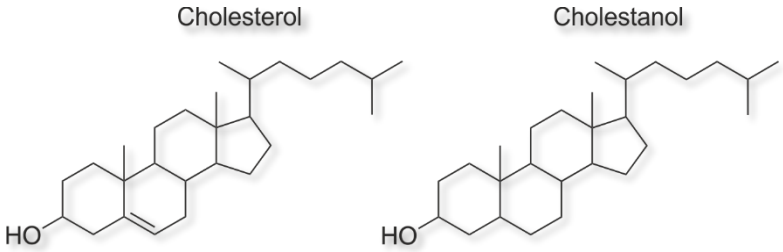			

I.3. High-resolution reconstruction of climatic change

Conventional lipid biomarker analysis with gas or liquid chromatographic methods coupled to mass spectrometers generally implies subsampling of a sediment core into centimeter-sized intervals to obtain sufficient amounts of the lipid extract for the analysis. However, this sample requirement results in a restriction of the temporal resolution as each sample tends to integrate time periods of decades to millennia, depending on the depositional setting. As a result, short term and abrupt climate fluctuations which operate on annual or decadal time scales remain inaccessible by the conventional lipid biomarker approach. Even in depositional settings with high sedimentation rates and preservation of the alternating seasonal input as varves, reconstruction of the potentially archived climate history demands extremely high subsampling rates leading to large sample amounts and major analytical effort. Taking into account those expenses, the obtained results hardly exceed annual averages causing an underrepresentation of e.g. strong warming events associated to the El Niño-Southern Oscillation phenomenon (ENSO) (cf. Kennedy and Brassell, 1992).

In paleoclimatology, decoding information of short-term environmental processes has so far been restricted to high resolution scanning techniques operating on sub millimeter scales such as X-ray fluorescence (XRF). The combination of XRF-scanning with unique lacustrine and marine varved records has provided insights into the timing of the abrupt climate change during the Younger Dryas cooling in Europe (Brauer et al., 2008), hydrological variations through the Holocene (Haug et al., 2001) and even the influence of abrupt drought events on the collapse of the Maya civilization (Haug et al., 2003). Nevertheless, the XRF-scanning approach can only obtain information on the elemental composition of the sediment. Detailed insights into the biochemical response to climate change remains to the tool of molecular stratigraphy. Increasing the spatial resolution of biomarker analysis, without expanding individual sample size would allow to address new and otherwise inaccessible questions related to climatic variability.

I.3.1. Spatially resolved lipid biomarker analysis

Spatially resolved biomarker information was first introduced to the field of geobiology by tracing archaeal lipids from carbonate microbialites or microbial mats using time-of-flight secondary ion mass spectrometry (ToF-SIMS) (Thiel et al., 2007a; Thiel et al., 2007b). Whereas this “molecular mapping” was a pioneering study for small-scale geobiological systems, mass spectrometry imaging (MSI) is a widely applied approach in biomedical research.

One frequently used technique of MSI is matrix-assisted laser/desorption ionization (MALDI). The basic principle of MSI with involves the laser-induced desorption of the analyte from the sample, its subsequent primary ionization during the laser pulse and secondary ionization in

the expanding ion plume, and its detection by mass spectrometry (MS) (Dreisewerd, 2003; Knochenmuss and Zenobi, 2003). With the laser rastering across a sample in a defined pattern, information on the localization of targeted molecules can be obtained (Caprioli et al., 1997). Most often this technique has been used on mammalian tissue sections, providing detailed insights into e.g. the localization of proteins specific for certain regions of the mouse brain or in human brain tumor xenograft sections (Stoeckli et al., 2001). Most MALDI imaging application are performed with a ToF-MS system, which allows for high spatial resolution, but is lacking of mass resolving power. Coupling of Fourier transform-ion cyclotron resonance-mass spectrometry (FT-ICR-MS) allows for accurate identification of different compounds that cannot be distinguished with ToF-based techniques (Taban et al., 2007). Despite differences in the detection of ions, all MALDI application share the need for accurate sample preparation involving a smooth and undisturbed surface of the sample, which is crucial for the successful molecular ion imaging. The typical workflow for a spatial analysis with MALDI MS (Fig. 1) involves the embedding of the sample with a MS-compatible material, its sectioning into micrometer thin slices and the application of ionization-aiding matrix (Heeren et al., 2008).

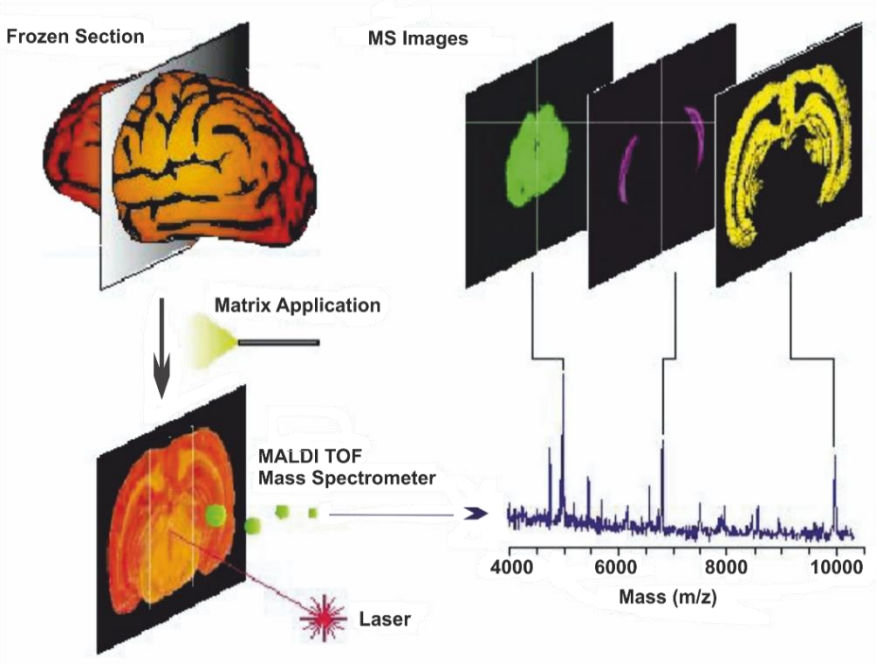

Fig. 1: *Schematic of a typical MALDI MS workflow with mounting of the frozen section and its subsequent coating with ionization-aiding matrix. The impact of a pulsed ultraviolet laser rastering across the sample leads to the desorption and ionization of the analytes from the tissue. With the detection of the m/z values by a time-of-flight analyzer from individual laser spots mass spectrometric images can be generated. From Stoeckli et al. (2001).*

Even though marine sediments are quite different to biological tissues, the general concept of analyzing molecular biomarkers to gain insights into the processes involved into their occurrence and distribution in the sample is very similar. The potential of a direct, extraction-free

analysis of a sample at a high spatial resolution for molecular stratigraphy was shown for the first time by Wörmer et al. (2014). Although the intact sediment sample from an eastern Mediterranean sapropel was still far from an optimal sample for MSI, MALDI-FT-ICR-MS was successfully used to map archaeal lipid biomarkers at a 200 µm resolution. This initial study provided an unprecedented view into the fine patterns of the lipid distribution and extracted paleoenvironmental information on SST variability coupled to solar cycles at a temporal resolution inaccessible to conventional analytical techniques.

I.3.2. Extraction-free molecular stratigraphy with MALDI-FT-ICR-MS

When Wörmer and colleagues (2014) applied MSI to an intact sediment section of the eastern Mediterranean sapropel they introduced a new approach for molecular stratigraphy with the potential to overcome the limitations of extraction-based biomarker analysis (Fig. 3). This first laser-based study focused on the detection of core isoprenoidal glycerol dibiphytanyl glycerol tetraethers (GDGTs) from planktonic Thaumarchaeota, used in the widely applied SST proxy TEX_{86}. Since the MALDI-MS approach does not involve a chromatographic separation of the compounds, the traditional TEX_{86} SST proxy could not be applied because of the identical mass to charge (m/z) values of the major core lipid with four cyclopentane and one cyclohexane ring (GDGT-5) and its isomer GDGT-5', which is included in the original regression. Thus, Wörmer et al., used another ratio known to be sensitive to SST variations (Schouten et al., 2002) based on the two major core lipids, GDGT-0 (caldarchaeol) and GDGT-5 (crenarchaeol) in the form of a crenarchaeol – caldarchaeol tetraether index (CCaT, equation 1). Obtained by MALDI-FT-ICR-MS, GDGT-5 in this index corresponds to the GDGT with 5 double bond equivalents, including cycloalkyl rings, double bonds, stereo/constitutional isomers of the major compound crenarchaeol and any possible combinations thereof (Zhu et al., 2013; Liu et al., 2018). In marine sediments the main component of GDGT-5 is crenarchaeol, followed by the isomer (Liu et al., 2018; Sinninghe Damsté et al., 2018). To account for the detection of this compound by accurate m/z value instead of chromatographic separation it is referred to as GDGT-5_{MS} (Wörmer et al., 2014; Alfken et al., 2019; equation 1).

The SST calibration for the CCaT (Wörmer et al., 2014; Fig. 2B) is based on the global data set by Kim et al. (2010) and its strength is somewhat weaker compared to the original TEX_{86} calibration (Schouten et al., 2002) or its derivates (Kim et al., 2010), probably due to additional factors reflected in the CCaT, i.e. changes in the archaeal community due to the wide distribution of GDGT-0 among Archaea (Schouten et al., 2002). The strong correlation of MALDI-FT-ICR-MS-derived CCaT values with values retrieved from conventional high performance liquid chromatography atmospheric pressure chemical ionization mass spectrometry (HPLC/APCI-MS) demonstrates the robustness of MALDI-FT-ICR-MS to ionize and detect GDGTs (Fig. 2A).

Equation 1: $$\text{CCaT} = \frac{\text{GDGT-5}_{\text{MS}}}{\text{GDGT-0} + \text{GDGT-5}_{\text{MS}}}$$

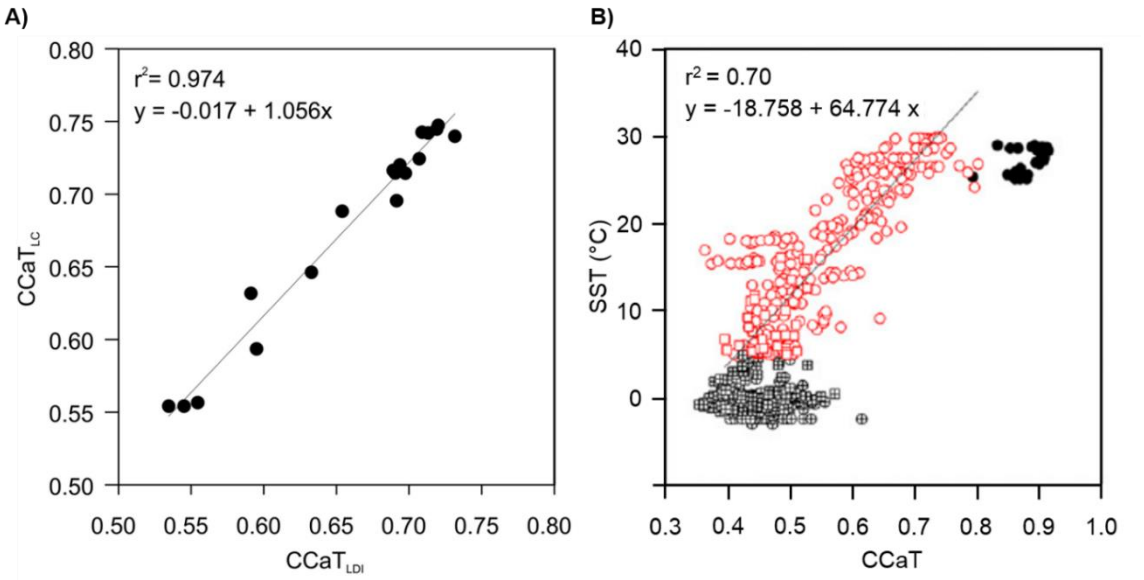

Fig. 2: *(A) Correlation between MALDI-FT-ICR-MS ($CCaT_{LDI}$) and HPLC/APCI-MS ($CCaT_{LC}$) based measurements of the CCaT. (B) Calibration for the CCaT proxy. CCaT values obtained from core top data (c.f. Kim et al., 2010; Ho et al., 2014) were correlated with satellite-derived SST. Data from the Red Sea (black circles) as well as those below 5 °C (crossed symbols) were excluded from the calibration. Both figures from Wörmer et al. (2014).*

Compared to the more conventional application of MALDI MS on tissue samples, the first study on a marine sediment was facilitated without the application of an artificial matrix, as the GDGTs were readily detected as sodium- (Na^+) adducts, leading to the conclusion that sediments serve as a natural matrix. Besides the amenability of sediments to MALDI MS the study by Wörmer et al. (2014) also showed the importance of ultra-high mass resolving power for the accurate identification of the compound of interest. For GDGTs the *m/z* value of the second isotopic peak of a GDGT with *n* cycloalkyl rings (e.g. GDGT-2 with 2 x ^{13}C), will be very close to the *m/z* value of a GDGT with n-1 cycloalkyl moieties (e.g. GDGT-1; Fig.3C). The best separation of the analytes of interests is given by the high mass resolving power of FT-ICR-MS.

Besides showing the suitability and robustness of MALDI-FT-ICR-MS for analyzing archaeal core lipids in marine sediments, the initial study by Wörmer and colleagues (2014) paved the way for addressing high-resolution climate fluctuations with molecular stratigraphy. In the Mediterranean sapropel, the laser-based analysis resulted in a temporal resolution of ~3 years. In some sedimentary records, such as laminated or varved marine and lacustrine records with high sedimentation rates, this approach can technically achieve a subannual resolution.

The basic concept of FT-ICR-MS involves that the generated ions are transferred into a spatially uniform static magnetic field where they rotate around that field at a cyclotron frequency proportional to their charge and mass. The ions are trapped in the ICR cell by small voltages of the same polarity and are further excited using an externally amplified radio frequency (RF) signal to generate spatially coherent ion packages of the same m/z. The motion of these ion packages in the circular orbit between the detection plates creates a time-domain waveform that can be transformed to a frequency domain by fast Fourier transform and further into the m/z domain (Marshall and Hendrickson, 2008).

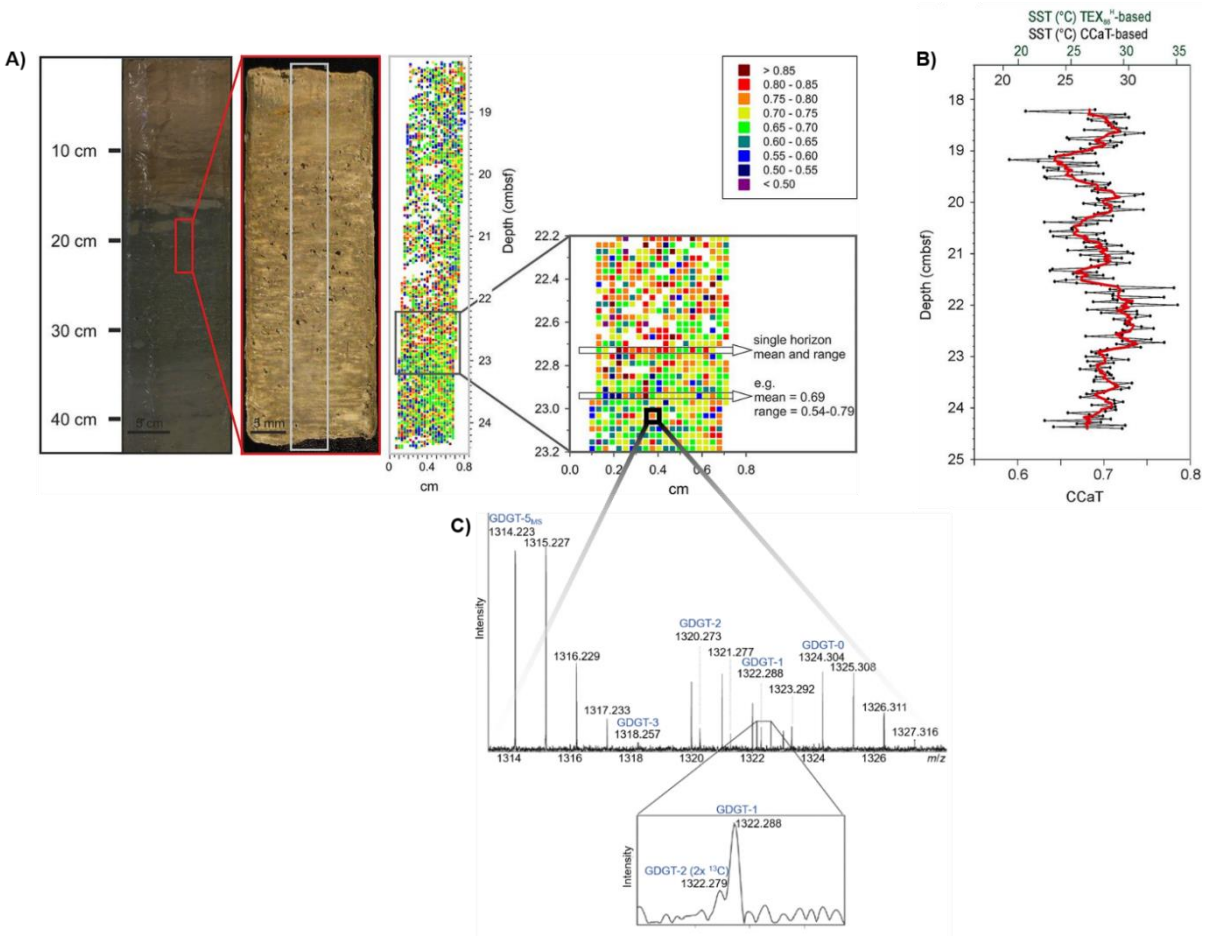

Fig. 3: *(A) Photograph of the segment from eastern Mediterranean core GeoB15103-1 used for high-resolution MALDI-FT-ICR-MS analysis. The section analysed with MALDI-FT-ICR-MS is shown in red and corresponds to the upper part of sapropel 1. The colored map shows CCaT values for each analysed spot with an exemplary zoom-in, as well as average and range values for selected horizontal layers. (B) 200 µm-resolved profile of averaged CCaT values, translated into CCaT- and TEX_{86}–based temperatures. Red line shows the 7-point running average. (C) Single FT-ICR-MS spectra showing the detected GDGTs as Na^+-adducts. Enlargement shows the capacity to differentiate GDGT-1 (m/z = 1322.289) and the isotopologue of GDGT-2 containing two ^{13}C (m/z=1322.280). Modified after Wörmer et al. (2014).*

I.4. Sediment archives suitable for high-resolution molecular stratigraphy

Ideal sedimentary records for high-resolution molecular stratigraphy are finely laminated marine and lacustrine sediments with a cyclic sedimentation pattern driven by the annual climate variability. Such varved sediments represent natural archives of paleoenvironmental conditions at a high temporal resolution with an accurate time control. The overview of modern and Quaternary varve sites (Fig. 4) shows the close proximity of marine varves to the shore, whereas varved lacustrine sediments occur globally.

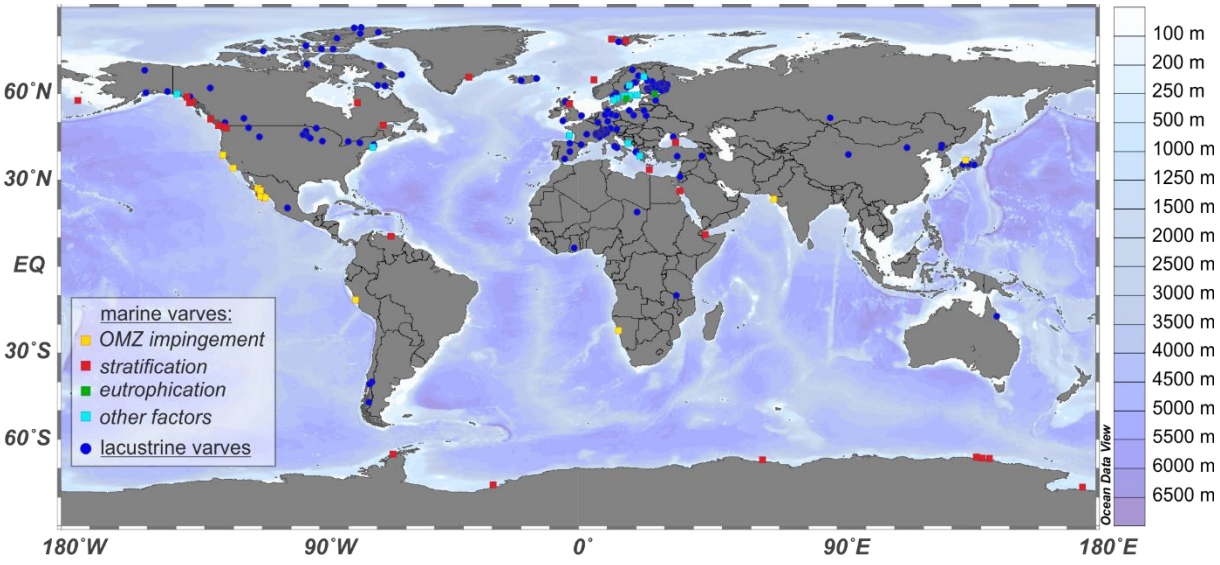

Fig. 4: *Global occurrence of reported Quaternary marine (squares) and published lacustrine varves (blue circles) compiled from Schimmelmann et al. (2016) and Zolitschka et al. (2015), respectively. For marine varves the primary formation processes are distinguished with different colors. Bathymetry is shown on the right. Map has been generated using Ocean Data View (Schlitzer, ODV5, http://odv.awi.de).*

For the formation and preservation of varved sediments in lacustrine and marine environments oxygen-depleted bottom waters are a prerequisite, as they prevent bioturbation from macrobenthos. Eutrophic conditions in lakes promote varve preservation, as they foster organic matter production and its subsequent microbial oxidation enhances bottom water anoxia. Lacustrine varves are more likely to form in deeper lakes (<10 m) with a small surface area, surrounded by an elevated terrain and protected from wind-driven mixing of the water column by forests. The seasonally alternating biological production and/or sediment fluxes from the catchment area, as well as precipitation of minerals from the supersaturated water column during strong evaporation results in different types of varved sediments (reviewed by Zolitschka et al., 2015).

In marine environments bottom water anoxia and varve formation is driven by different oceanographic factors (Fig. 4). In fjords or glacial embayments the strong freshwater input

together with denser ocean water supply over a sill leads to permanent density stratification of the water column and the remineralization of organic matter to a depletion of oxygen in the bottom water. Density stratification also occurs in brine-filled deep basins, such as the Shaban Deep in the Red Sea, and can also develop due to seasonal freezing of seawater. Eutrophication, as observed in the Baltic Sea, leads to increased primary productivity and consumption of dissolved oxygen in deeper water layers. Another process aiding varve formation is the impingement of oxygen minimum zones (OMZ) on the shelf or into near coastal basins presenting sill depths within the OMZ. In these settings hypoxic to anoxic bottom water conditions can even be enhanced and stabilized due to coastal upwelling of nutrient-rich waters intensifying productivity in the photic zone and increasing export production. Other reasons for varve formation in marine sediments can be a restricted hydrological connection to the ocean like in lagoons or estuaries, a stratification breakdown due to a major diatom flux after a bloom during water column stratification and its sudden deposition in fall/winter with water column mixing, or in general high sedimentation rates that overwhelm low bioturbation (reviewed by Schimmelmann et al., 2016).

Due to their connection to the open ocean marine varves represent archives for detailed information on large-scale ocean and atmospheric climate phenomena such as monsoon intensity (Lückge et al., 2001) or El Niño Southern Oscillation (ENSO) (Kennedy and Brassell, 1992). Meanwhile, lacustrine varves are very sensitive to regional environmental variability like increased wind strength over a German maar lake associated to the abrupt change in the North Atlantic westerlies during the Younger Dryas cooling (Brauer et al., 2008).

I.5. Santa Barbara Basin – an ideal study site

Laminated and varved sediments from the deep center of the Santa Barbara Basin (SBB) off Southern California provide a unique archive for high-resolution climate reconstruction and have been used in a large number of studies; from the reconstruction of pacific sardine and anchovy populations for the past two millennia (Baumgartner et al., 1992), to the investigation of changes in marine productivity in relation to modern large-scale oceanic events like El Niño (Lange et al., 1987; Lange et al., 1997), or the reconstruction of the ENSO-scale variability in the past (Bull et al., 2000; Nederbragt and Thurow, 2005) and its influence on the Californian hydroclimate variability (Hendy et al., 2015; Napier et al., 2018).

Additionally, physical and biological properties in the California current system (CCS) and the SBB have been monitored since 1949 by the Californian Oceanic Fisheries Investigation (CalCOFI) program, as a response to the collapse of the sardine population off California. Whereas the data coverage for the station located in the center of the SBB (station 81.8 46.9., Fig. 5A) is

rather patchy until 1984, a continuous seasonal monitoring of various water properties over the entire water column exists from this year onwards. Besides oxygen concentrations, which are shown from 1984 to 2009 as a contour plot in Fig. 5C, other properties such as temperature, salinity, oxygen and nutrient concentrations are available from this monitoring program.

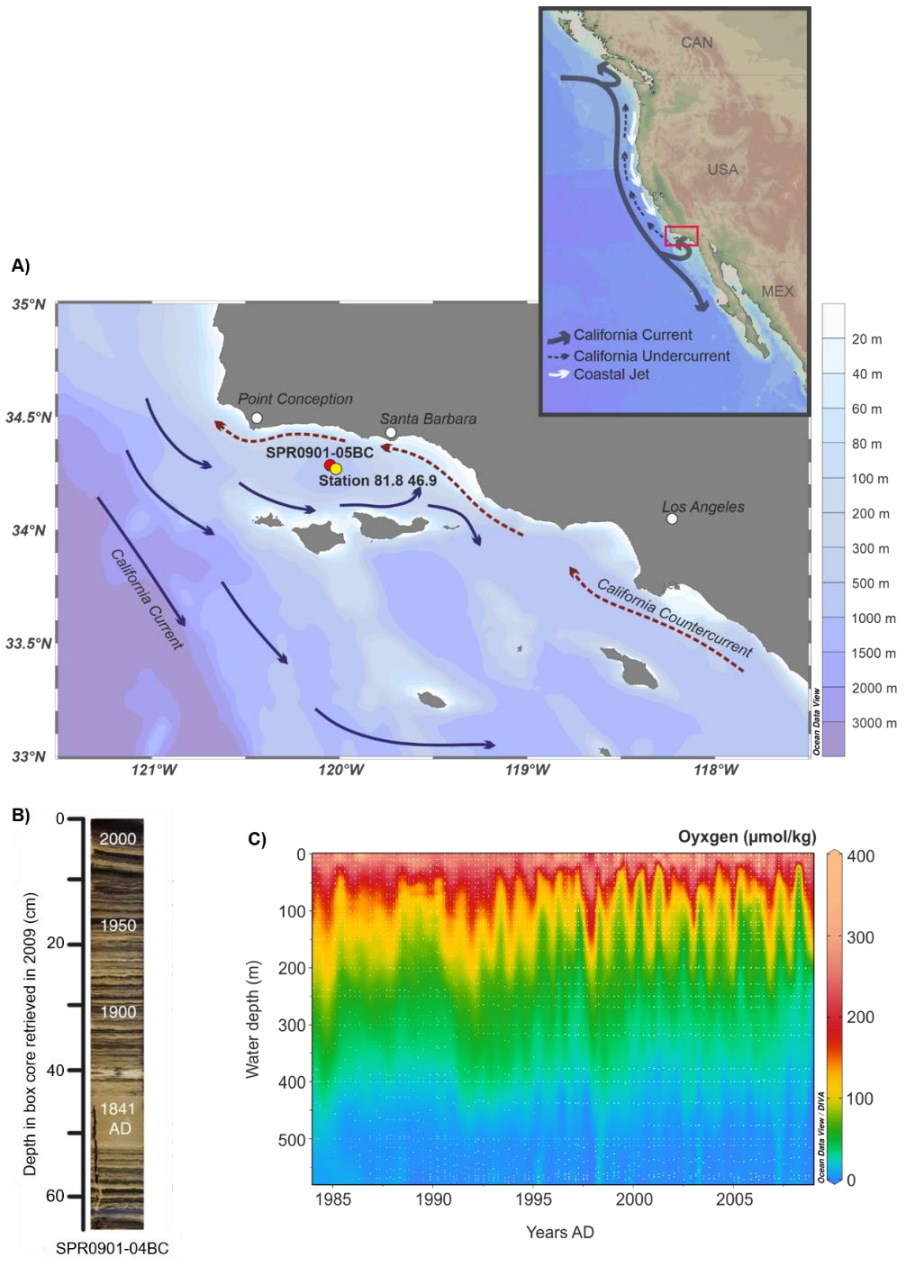

Fig. 5: *(A) Map of the Santa Barbara Basin (SBB) and its location within the California Current System. Currents are adapted from Checkley and Barth (2009) and Hendy et al. (2013). Red rectangle in overview map shows the location of the SBB. The location of the box core used this thesis (SPR0901-05BC) is marked with a red dot. The CalCOFI station 81.8 46.9. is shown by the yellow dot. (B) Photograph of modern varves exemplarily shown for the neighboring box core SPR0901-04BC taken from Schimmelmann et al., 2013. (C) Oxygen concentrations for the entire water column at CalCOFI station 81.8 46.9. from 1984 to 2009 A.D. White dots show CalCOFI measurements. Maps have been generated using Ocean Data View (Schlitzer, ODV5, http://odv.awi.de).*

The suboxic conditions in the bottom waters (Fig. 5C) of the SBB together with high sedimentation rates of seasonally alternating input leads to the formation of laminated sediments. Ocean ventilation is prevented by a deep topographic sill in the west, currently at 475 m depth, which separates the SBB from the open ocean (Emery and Hülsemann, 1961). Occasional flushing events can lead to a mixing, but not to a complete oxygenation of the bottom water (Goericke et al., 2015). The dense and oxygenated water enters the basin over its western sill by strong seasonal upwelling during winter and spring north off Point Conception (Reimers et al., 1990; Bograd et al., 2002; Goericke et al., 2015). Varves in the SBB are composed of clastic dominated dark laminae related to fall/winter precipitation and the associated silt input from river runoff and a light biogenic diatom-ooze (Fig. 5B), which is produced during the spring-summer period when surface productivity increases as a result of enhanced upwelling (e.g., Emery and Hülsemann, 1961; Soutar and Crill, 1977; Thunell et al., 1995; Thunell, 1998). Varve formation is also supported by sulfur oxidizing filamentous bacterial mats (*Beggiatoa spp*.), which frequently cover the sediment surface forming an adhesive layer binding organic and inorganic particle and protecting the topmost laminae from erosion by weak bottom currents (Soutar and Crill, 1977).

Laminated sediments have been deposited throughout most of the Holocene and warm interglacials or interstadials, whereas the lower sill depth and stronger ventilation of the basin during glacial stages resulted in bioturbated sediments (Behl and Kennett, 1996). From the present down to ~ 1700 AD laminated sediments from the center of the basin reveal annual varve couplets with a thickness from 0.5 to 3 mm. Prior to ~ 1700 AD many laminations are not annual varves, potentially due to lacking terrestrial clastic seasonal input as a result of low riverine input and infrequent winter storm activity, erosion of the topmost layer by density currents or bottom water oxygenation (Schimmelmann et al., 2013).

Oceanographic conditions in the SBB are strongly influenced by the California Current System (CCS) including the equatorward California Current, the poleward offshore California Undercurrent, extending north off Point Conception, and the inshore southern California Countercurrent (Fig. 5; Hickey, 1979; Hendershott and Winant, 1996). Variability of CCS is controlled by the large-scale winds associated to the North Pacific High, the Aleutian Low and the continental thermal low-pressure over central California to northern Mexico. The strength of the southward flowing California Current and its embedded intense jets are controlled by the seasonal changes of the intensity and position of the North Pacific High. During winter the North Pacific High weakness and is displaced equatorward, whereas the Aleutian Low intensifies, directing storms into Northern California. During summer the North Pacific High strengthens and migrates to its most northerly position in August, whereas the adjacent continental thermal Low deepens. The resulting pressure gradient drives equatorward winds off California, which are strongest in

early summer. As a result, the summertime equatorward alongshore wind stress induces net transport in the surface Ekman layer, leading to upwelling of nutrient-rich, cold and salty deep water (Huyer, 1983; Checkley and Barth, 2009). During upwelling a counterclockwise surface circulation exists in the basin (Hendershott and Winant, 1996), which can be observed in ascending isotherms during April to June (e.g. Thunell, 1998).

The CCS and thereby the circulation within the SBB are influenced by large-scale climate phenomena on interannual to decadal time scales. In the flowing these low-frequency climate fluctuations and their influence on the SBB will be described.

i. El Niño Southern Oscillation (ENSO; Fig 6A) is the dominant coupled atmosphere-ocean phenomena affecting the tropical Pacific, oscillating between its warm, cold and neutral state with periods of 2 to 7 years. During the neutral ENSO state warm and moist air masses rise over the western tropical Pacific into the atmosphere, bringing along strong precipitation. The air masses flow poleward towards the subtropical oceans and sink into the regions of high surface pressure. In turn, this Hadley circulation is closed by surface air drawn in from the subtropical high pressure towards the equator. Due to the Coriolis effect, these equatorward flowing surface air masses are deflected westward and become easterly trade winds. The trade winds drive the westward surface flow of the South Equatorial Current, piling up warm surface water in the western Pacific, and draining it from the eastern Pacific. Consequently, the thermocline subsides in the west, whereas the shallow thermocline in the eastern Pacific facilitates upwelling of cold and nutrient-rich water. The emerged east-west temperature gradient reinforces trade winds, which in turn pick up heat and moisture from the ocean on their east-west track. The resulting warm and humid air masses rise again over the western Pacific and close this Walker circulation.

   During the warm state this circulation pattern changes as trade winds weaken when the atmospheric pressure rises in the west and becomes lower in the east. The weakened trade winds generate interior ocean waves radiating along the equator leading to an elevation of the thermocline in the west and deepening in the east. Consequently, upwelling along the eastern Pacific is strongly reduced and SSTs increase. This warm ENSO state, called El Niño typically persists for 12 – 18 months.

   The cold ENSO state, called La Niña, exhibits opposite patterns which can be described as an intensification of the neutral conditions with stronger than normal trade winds, a shallow thermocline in the east with strong upwelling and cool SSTs (McPhaden, 2002).
   ENSO is usually characterized by SST anomalies averaged over a defined region in the equatorial Pacific. The region from 5°N – 5°S, 170° - 120°W defines the two most commonly used indices, Niño 3.4 index (Trenberth, 1997), and the Oceanic Niño Index (ONI) produced

by the National Oceanic and Atmospheric Administration (NOAA). When SST anomalies in the Niño 3.4 exceed ±0.4 °C for a period of at least six months the ENSO state is defined as an El Niño or La Niña event (Trenberth, 1997).

The effects of ENSO on the CCS can be profound, especially in its southern region (Lluch-Cota et al., 2001). During an El Niño event upwelling intensity in the SBB decreases and the equatorward transport of cold water from the California Current diminishes, whereas the strength of the warm California Undercurrent increases (Lynn et al., 1995; Bograd and Lynn, 2001; Jacox et al., 2015) leading to a reduction in primary productivity (Thunell 1998; Venrick 2012).

ii. Pacific Decadal Oscillation (PDO, Fig. 6B) describes an interdecadal variability affecting the CCS with most energetic periodicities from 15 – 25 years and 50 – 70 years. It can be characterized by the first mode of variation of SST within the North Pacific (north of 20°N) and has been described as a "long-lived El Niño-like pattern" (Mantua et al., 1997; Hare and Mantua 2000). The PDO and its influence on the CCS are divided in two phases, i.e. the warm (positive) and cold (negative). During the positive PDO the Aleutian Low intensifies and the coastal thermocline in the CCS deepens, resulting in lower upwelling and marine productivity. Similar to ENSO, the negative phase shows a reverse pattern leading to higher productivity (Chavez et al., 2003). Two complete PDO cycles existed during the past century. Negative (cool) phases of the PDO existed from 1890 – 1924 and 1947 – 1976, while the positive (warm) PDO regime was prevailing from 1925 – 1946 and from 1977 onwards, though after the strong 1997/98 El Niño a shift to the cold phase may have occurred (Mantua and Hare 2001).

iii. North Pacific Gyre Oscillation (NPGO; Fig. 6C) is the second mode of variation of sea surface height in the North Pacific and correlates with CalCOFI measurements of nutrient, salinity and chlorophyll *a* fluctuations associated to the wind-driven upwelling between 38°N and 30°N. In this region the NPGO can explain some changes in primary productivity that are not captured by the PDO (Di Lorenzo et al., 2008).

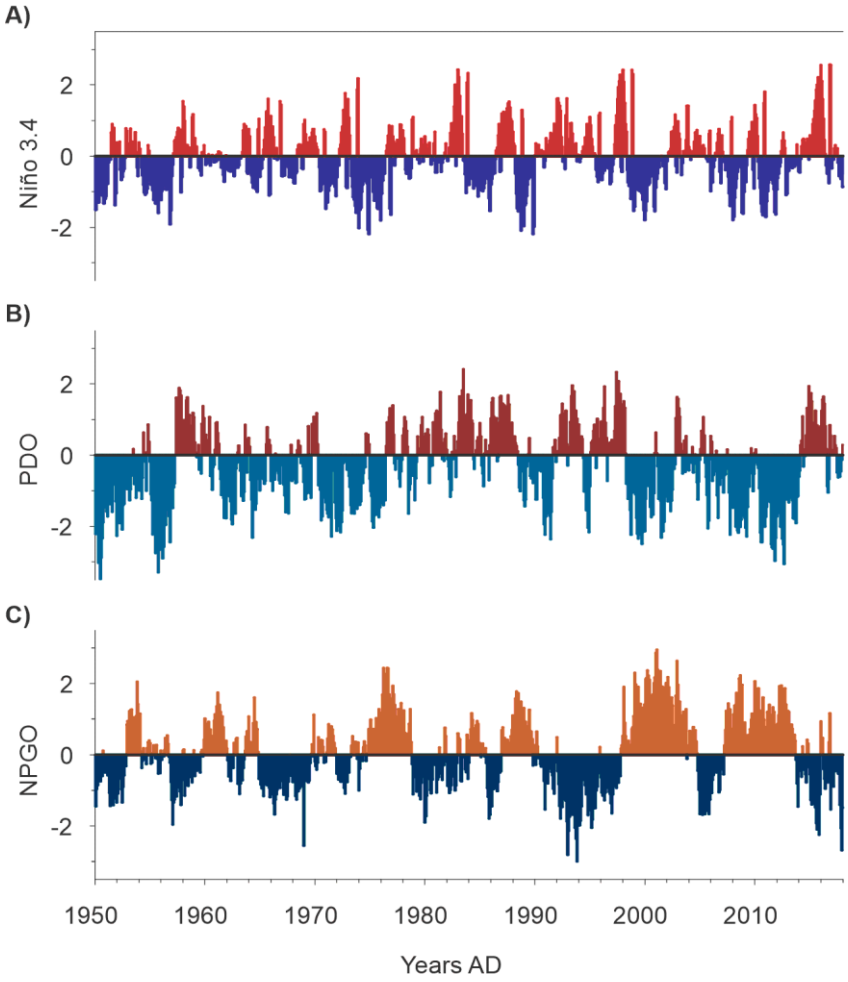

Fig. 6: *Time series of Pacific climate indices since AD 1950. A) El Niño Southern Oscillation expressed as the Niño 3.4 anomalies. B) Pacific Decadal Oscillation (PDO) and C) North Pacific Gyre Oscillation (NPGO).*

Pacific climate variability associated to these large-scale climate fluctuations is reflected in the oceanographic and atmospheric conditions in the SBB area, affects marine production as well as coastal runoff and hence is archived in the varved and laminated sedimentary record. Sub-millimeter molecular stratigraphy using MSI potentially provides the tool to access this information and gain a better understanding of how these large-scale climate fluctuations evolved in the past, which is crucial for assessing their future behavior and the effect of climate change. Additionally, existence of seasonally resolved instrumental data allows for direct evaluation of molecular proxy records in the modern SBB.

I.6. Structure and main objectives of this thesis

In this thesis a new, extraction-free method for spatially resolved lipid biomarker analysis on intact sediments was implemented as a tool for molecular stratigraphy at unprecedented temporal resolution. This approach allowed for detailed understanding of the lipid proxy signal and the climate history archived in the sediments of the Santa Barbara Basin (SBB), off Southern California.

The first part of this dissertation includes two peer-reviewed published manuscripts (CHAPTER II and CHAPTER III) that establish the guidelines for MSI of sedimentary biomarkers, from sample preparation to generation of micrometer-scale lipid biomarker maps and multiproxy records.

Research questions:

- *How can sediment samples be prepared in order to exploit the whole potential of MSI for high-resolution molecular stratigraphy?*
- *Can MSI be combined with other spatially resolved methods such as elemental analysis?*
- *How robust and reproducible are the resulting laser-based proxy records?*
- *Is it possible to extend the set of lipid biomarkers detectable by MALDI-FT-ICR-MS and use MSI in multiproxy studies?*

In CHAPTER IV modern varved sediment from the SBB were used to create monthly-resolved records of the alkenone-based $U^{K'}_{37}$ and the GDGT-based CCaT proxies. The direct comparison of these SST sensitive proxy signals to 25 years of seasonally measured water column properties reveals previously inaccessible insights into the factors driving their composition.

Research questions:

- *Is MSI capable of resolving fine-scaled differences between these two proxies?*
- *Do alkenone and GDGT-based proxies mirror actual sea surface temperature or are they influenced by physiological responses to other water column properties?*
- *If so, can these proxies be used to gain additional information on the variable oceanographic conditions in the SBB?*

CHAPTER V investigates the climate history of the past century in the SBB. The high-resolution multiproxy study of a ~30 cm sediment box core from the SBB informs on high-frequency SST changes, upwelling variability linked to large-scale climate oscillations and insights into variations of bottom water redox conditions.

Research questions:

- *Is the reported 20th century warming along the Southern Californian coast archived in the SBB sedimentary record?*
- *How did the upwelling intensity change during the past century and which large-scale Pacific climate phenomena influenced its variability?*
- *How do bottom water redox conditions change in the scenario of warming ocean temperatures and increasing stratification?*

CHAPTER II

MICROMETER SCALE IMAGING OF SEDIMENTARY CLIMATE ARCHIVES – SAMPLE PREPARATION FOR COMBINED ELEMENTAL AND LIPID BIOMARKER ANALYSIS

Susanne Alfken[a*], Lars Wörmer[a], Julius S. Lipp[a], Jenny Wendt[a], Heidi Taubner[a], Arndt Schimmelmann[b], Kai-Uwe Hinrichs[a]

Published in *Organic Geochemistry*

Vol: 127 January 2019, pages 81-91,

https://doi.org/10.1016/j.orggeochem.2018.11.002

[a] Organic Geochemistry Group, MARUM – Center for Marine Environmental Sciences and Faculty of Geosciences, University of Bremen, Leobener Str. 8, 28359 Bremen, Germany

[b] Department of Earth and Atmospheric Sciences, Indiana University, 1001 E 10th Street, Bloomington, IN 47405-1405, USA

[*] Corresponding author: E-mail address: salfken@marum.de

Abstract

Mass spectrometry imaging (MSI) can be used for the µm-scale mapping of target molecules on intact sample surfaces. Recently we demonstrated that MSI of non-disturbed sediments can be used for paleoenvironmental studies; using matrix-assisted laser desorption/ionization coupled to Fourier transform-ion cyclotron resonance-mass spectrometry we visualized the spatial distributions of archaeal glycerol dibiphytanyl glycerol tetraether (GDGT) lipids. There is a pressing need for implementing sample preparation procedures that allow exploiting the full potential of sediment MSI. Here we present a suite of sample preparation steps, optimized for the analysis of GDGTs in marine sediments. It considers the crucial requirements for successful MSI and optional combination with elemental imaging via micro X-Ray Fluorescence Spectroscopy (µ-XRF). Preservation of the sediment's spatial distribution is achieved with freeze-drying and subsequent embedding in a mixture of gelatin and carboxymethyl cellulose. This enables sectioning the sample into sequential slices from 20 to 500 µm in thickness. Thinner sections showed enhanced signal intensity in MSI, but elemental mapping by µ-XRF is more accurate for thicker sections; 100 µm thick slices provide satisfactory results for both analyses and are recommended for congruent elemental and biomarker imaging. When applied to the uppermost ~5 cm of marine sediment from a Santa Barbara Basin box core, the optimized sample preparation yields reproducible ultra-high-resolution GDGT records from sequential slices, thus demonstrating the robustness of the method. Congruent µ-XRF results aid the establishment of a contextual framework regarding supply of terrigenous and marine detritus as well as the assignment of molecular data to annual layers.

II.1. Introduction

Molecular fossils in marine sediments are largely derived from the membrane lipids of microorganisms that once inhabited the overlying water column. Since membrane lipids play an important role in the regulation of membrane fluidity and its adaption to habitat conditions, such as temperature and pH, these fossil biomarkers encode valuable information about the environmental conditions under which they were produced. Retrieval of this information from a sedimentary record with an established age model has been termed molecular stratigraphy (Brassell et al., 1986), and has helped to understand and reconstruct paleoenvironmental conditions and ecosystems (Hinrichs et al., 2003; Kuypers et al., 2003; Sepúlveda et al., 2009b).

One example of such biomarkers with a widely recognized potential for paleoenvironmental studies is the glycerol dibiphytanyl glycerol tetraethers (GDGTs), whose main source is planktonic, ammonia-oxidizing Thaumarchaeota. These compounds are ubiquitous, they persist in the sedimentary record over geological times (Kuypers et al., 2001; Schouten et al., 2003) and their sensitivity to record past sea surface temperature is used in the paleo sea surface temperature (SST) proxy TEX_{86} (Schouten et al., 2002). This proxy is based on the assumption that planktonic archaea increase the cyclization in the isoprenoidal GDGTs to adapt to higher habitat temperatures (Schouten et al., 2002). Even though it has been applied successfully in various studies, trends in reconstructed SSTs can also disagree with instrumental water temperatures and other proxy data (Pearson and Ingalls, 2013; Schouten et al., 2013). For instance, TEX_{86}-derived temperatures are systematically lower in upwelling regions, which has been explained by subsurface and/or seasonal production (Huguet et al., 2007; Lee et al., 2008; Lopes dos Santos et al., 2010; Chen et al., 2014).

To disentangle the factors influencing the cyclization of GDGTs, culture studies have been used and were able to show that the number of cyclopentyl moieties increases at higher temperatures (Wuchter et al., 2004; Schouten et al., 2007; Elling et al., 2015; Qin et al., 2015). Other factors, such as growth stage (Elling et al., 2014), oxygen availability (Qin et al., 2015) and the ammonia oxidation rate (Hurley et al., 2016; Evans et al., 2018) were also found to have an effect on GDGT cyclization. Especially the latter provides a clue towards the discrepancies in upwelling systems where cold proxy temperatures can result from higher growth rates due to higher ammonium supply (Hurley et al., 2016; Hurley et al., 2018).

In order to create a GDGT-based SST record, usually gram-sized sediment samples are needed for the extraction of the targeted compounds and their analysis by high performance liquid chromatography-mass spectrometry (HPLC-MS) methods (Hopmans et al., 2000; Becker et al., 2015). However, subsampling of sediment cores for extraction restricts the temporal

resolution because each sample tends to integrate across time periods of decades to millennia, depending on the depositional setting. Even laminated or varved sediments with high sedimentation rates traditionally limit the achievable time-resolution due to sample size and analytical effort. Thus, short-term climate fluctuations, which operate on annual to decadal time scales such as the El Niño Southern Oscillation (ENSO; Trenberth, 1997), the North Atlantic Oscillation (Lamb and Peppler, 1987; Hurrell, 1995) or the Pacific Decadal Oscillation (PDO; Mantua and Hare, 2002), remain inaccessible to, or at least difficult to resolve by the conventional lipid biomarker approach (Kennedy and Brassell, 1992) and were usually restricted to high-resolution scanning techniques such as X-Ray Fluorescence spectroscopy (XRF).

The application of XRF scanning techniques at millimeter to micrometer resolution on high-resolution sedimentary archives has been an excellent tool to gain information on, for example, Holocene climate and abrupt events such as the Younger Dryas in northern South America (Haug et al., 2001) and Europe (Brauer et al., 2008), as well as in droughts and flooding events in southern California associated with ENSO and PDO in the 20th century (Hendy et al., 2015) and Termination V (Napier et al., 2018).

Improving the sampling resolution for lipid biomarker analyses to a scale similar to XRF would give novel insights into these abrupt environmental processes. In 2014 we introduced a new, extraction-free method to detect archaeal biomarkers in marine sediment at an unprecedented spatial resolution (Wörmer et al., 2014). We used matrix-assisted laser/desorption ionization coupled to a Fourier transform-ion cyclotron resonance-mass spectrometer (MALDI-FT-ICR-MS) to create µm-scale images of GDGT distributions from the surface of an intact sediment core section. Successful ionization was achieved without application of an artificial matrix, because the natural sedimentary matrix facilitated ionization. The resulting proxy record of the newly introduced crenarchaeol-caldarchaeol tetraether index (CCaT) provided unprecedented insights into small-scale biomarker distribution and revealed a temporal SST variation potentially influenced by solar cycles.

This study provided an initial step towards the implementation of mass spectrometry imaging (MSI) in molecular stratigraphy and showed that MSI of lipid biomarkers in marine sediment can provide new and valuable information on past short-term climate and ecosystem variability. Such short-term variability can ideally be decoded at high temporal resolution from laminated or even varved sediments deposited in oxygen-deficient marine or lacustrine settings (Kennedy and Brassell, 1992; Zolitschka et al., 2015; Schimmelmann et al., 2016), which may allow the establishment of meaningful biomarker records of environmental variations on sub-annual time scales.

From MSI of tissue samples, mainly in the field of biomedical research (Schwartz et al., 2003; Heeren et al., 2009; Goodwin, 2012), but also plant science (Dong et al., 2016), it is known that sample preparation is crucial to the quality of the analysis. For the FT-ICR-MS instrument, ionization in the MALDI source occurs under vacuum. Consequently, dryness of the sample is a fundamental requirement, paired with a smooth, even, non-disturbed and stable surface to ensure high quality signals. Moreover, it is imperative that the biomarker distribution as well as the sedimentary fine structure and thus the spatial resolution are not compromised by sample preparation. Our goal was to implement a sample preparation sequence for sediment that satisfies the quality criteria of both MSI and elemental mapping with micro-X-Ray Fluorescence spectroscopy (µ-XRF).

Here we present a protocol that focuses on the optimized detection of GDGTs, but is also applicable to MSI of other analytes (Wörmer et al., 2019) such as alkenones, which would provide complementary information on SST (Brassell et al., 1986), or sterols that may provide insight into the ecology of eukaryotic primary producers (Huang and Meinschein, 1979; Volkman et al., 1998). Besides the development of a scheme for the routine investigation of GDGTs, this study also outlines a practical protocol for the acquisition of congruent molecular and elemental maps of sediment slices. Prior to biomarker analysis, the non-destructive analysis of the sample with µ-XRF provides valuable complementary information of the sediment property related to the depositional conditions and its changes due to hydrological variability and enables the investigation of biomarkers in the context of their sedimentary matrix.

II.2. Material and Methods

II.2.1. Sediment samples

A homogenized mixture of eastern Mediterranean sapropels S4, S5 and S6 from core GeoB15103-2 (Zabel et al., 2012) served as a test sediment for the different steps of sample preparation. The depths intervals used for this mixture are 363 – 389 cm (S4), 435 – 455 cm (S5), 550 – 557 cm (S6) and 595 – 599 cm (S6). According to the cruise report (Zabel et al., 2012), the core contains five sapropel layers, which were correlated based on their sizes and relative position to sapropels S1, S3, S4, S5 and S6 as identified by Calvert and Fontugne (2011).

Cylindrical pellets of this sediment mixture with a size of ~8 × 16 mm (height × diameter) and weighing ~2 g wet (~1 g dry) were shaped with 10 mL plastic syringes without a bottom. These pellets were used for experiments towards optimizing the sample preparation and measurements.

Additionally, an intact sediment slab from box core SPR0901-05BC retrieved in 2009 from the Santa Barbara Basin (SBB) served as a test to evaluate whether the proposed embedding and sectioning techniques are applicable to non-disrupted laminated sediment segments. The chosen segment from the 30 cm long slab covers the topmost ~5 cm from a box core that had significantly compacted since 2009. The interior sediment of the slab remained anoxic. The segment was sampled using double L channels (Nakagawa and Suigetsu 2006 project members, 2014) resulting in a width of 1.5 cm and 0.7 cm thickness. Sediments from the SBB are a unique archive and well-known for their ability to record high-resolution paleoclimate oscillations (Schimmelmann and Lange, 1996; Schimmelmann et al., 2016). Seasonally varying fluxes of lithogenic (winter) and biogenic (spring-summer) material combined with suboxic bottom water conditions result in the formation of annual varve couplets (Emery and Hülsemann, 1961; Soutar and Crill, 1977; Thunell et al., 1995; Thunell, 1998). For visualization of laminae, the intact section was X-radiographed with a Faxitron 43855A X-ray cabinet (Hewlett-Packard). X-ray photographs were taken using AGFA Strukturix D4 FW film and parameter settings of 45 kV and 3 mA at an exposure time of 7 min.

II.2.1. Chemicals

Noble agar, gelatin from bovine and porcine bones, sodium carboxymethyl cellulose (CMC), Tissue Tek optimal cutting temperature (OCT) compound, acetone, 2-propanol, and trifluoroacetic acid (TFA) were purchased from Sigma Aldrich Chemie GmbH (Munich, Germany). Methanol was supplied by Dewert Labortechnik e.K. (Rödinghausen, Germany), sodium hydroxide by VWR International GmbH (Hannover, Germany) and the indium-tin oxide-coated (ITO) glass slides by Bruker Daltonik GmbH (Bremen, Germany).

Sodium trifluoroacetate (NaTFA) as a tune/calibration solution for positive-ion electrospray ionization was prepared according to Moini et al. (1998). The solution was diluted to 50 vol% with 2-propanol instead of acetonitrile.

II.2.2. Dehydration of wet sediment slabs

To preserve the spatial structure and minimize possible changes and delocalization of compounds in the sediment during subsequent preparation steps, the sample and its spatial structure need to be stabilized. Three drying conditions were evaluated: Oven-drying of pellets at 40 °C, and freeze-drying after freezing the sediment pellets at -20 °C and -80 °C. Two freezing temperatures were tested adopting the instrumental parameters of the ALPHA 1-4 LD freeze dryer (Christ, Osterode am Harz, Germany) in a vacuum of 1 – 0.1 Pa. Optimal sublimation of ice occurs between -20 °C and -80 °C (Boës and Fagel, 2005).

Reduction of sample size during drying was measured with a caliper. Migration of soluble salts in brine to the exposed sample surface during drying was assessed by measuring the elemental composition of the pellet's surface with µ-XRF, scraping off the uppermost layer (~2 mm), and re-measuring with µ-XRF.

II.2.3. Embedding of freeze-dried sediment

Freeze-dried sediments are not sufficiently stable during handling and easily disintegrate when attempting to obtain thin sediment slices. Therefore, embedding the sediment in MSI-compatible media was considered to improve the preparation of sediment samples and facilitate cryosectioning. Our choice was constrained by the need to avoid organic solvents to prevent an extraction or delocalization of lipid biomarkers. Consequently, the conventional preparation of thin sections from sediments using epoxy resin for impregnation (Camuti and McGuire, 1999; Tiljander et al., 2002; Boës and Fagel, 2005) was considered impractical.

Three pure media with different concentrations and mixtures thereof were found to be suitable and were further evaluated for embedding of intact freeze-dried sediment samples (Table 1). Media were prepared and tested according to (Nelson et al., 2013). Each pure medium and mixture of media were prepared by adding solid(s) to a glass flask, followed by addition of deionized water (MilliQ) at room temperature. Each medium was gently heated up to ~60 °C and constantly agitated by a magnetic stir bar until completely dissolved.

Polystyrene beakers (12.5 mL) were used for embedding of sediment pellets. Prior to embedding, each beaker was filled ~1 cm high with warm embedding medium and placed in a freezer at -20 °C for a few minutes to cool down the medium. This created a solidified base for the sediment to prevent it from sticking to the bottom of the beaker. The remaining warm medium was allowed to cool slightly to ~40 °C. The beaker was filled up with the medium and the freeze-dried sediment pellets were placed carefully on the medium using forceps or by letting them slide from a piece of pre-annealed aluminum foil. Depending on the viscosity of the medium or mixture of media and the sediment density, sediment pellets sank spontaneously or needed to be pushed into the medium. Beakers containing submerged sediment were placed into a freezer at -20 °C for solidification prior to sectioning. Different embedding media were evaluated according to their physical properties in frozen condition, which influenced the sectioning efficiency, and in liquid stage if it had a noticeable effect on the embedding quality. Additionally, the stability of the sediment in the embedding media and the quality of the resulting slices during sectioning and when mounting onto ITO slides were taken into account.

Embedding of the ~5 cm section of SBB sediment was performed following the same procedure and using a rectangular silicone mold (8 × 4.5 × 2.5 cm; length × width × height).

Table 1: *Comparison of embedding media for MSI-based analysis of sediment samples. CMC: sodium carboxymethyl cellulose. Overall suitability classified as: optimal (+), acceptable (o) and poor (-).*

Embedding media (wt%)	**Media property (frozen; liquid)**	**Sample stability**	**Amenable to sectioning**	**Quality of slices**	**Overall suitability (+ o –)**
1% noble agar	Hard, waxy, brittle	Disintegrated	N.T.	N.T.	–
CMC (5%, 2%)	Hard, semi hard	Disintegrated	N.T.	N.T.	–
Gelatin (10%, 5%)	Hard	Stable	Optimal	Flaking	o
1% noble agar + gelatin (10%, 5%)	Hard, semi hard, brittle	Partial disintegration	N.T.	N.T.	–
5% CMC + gelatin (10%, 5%)	Semi hard; very viscous	Incomplete embedding	N.T.	N.T	–
5% gelatin + 2% CMC	Semi hard	Stable	Optimal	Optimal	+
10% gelatin + 2% CMC	Semi hard; very viscous	Incomplete embedding	Poor, disintegration	N.T.	–

N.T.: medium not tested due to poor sample stability and low quality of cryomicrotome slices

II.2.4. Cryosectioning of embedded sediment

The embedded and frozen sediment was removed from the beaker after slight warming of the beaker's plastic and placed in the cryomicrotome (Microm HM 505 E Cryostat, GMI, Ramsey, Minnesota, USA) at -15 °C or -20 °C, depending on the embedding medium, for at least 30 min for temperature equilibration. Each frozen block was attached to the specimen holder using a small amount of Tissue Tek optimal cutting temperature (OCT) compound and oriented with the sediment surface facing to the front. Sections of 20, 60, 100, 150, 200 and 500 µm thickness were cut from each test pellet and placed onto ITO glass slides. Sediment slices were adhered by a slight warming of the back of the ITO slide using the ball of the thumb and dried in a desiccator for 30 min to 2 h, depending on their thickness. Sections with defined thickness were prepared in

triplicate and evaluated for elemental distribution and MSI quality. Presented data are average values of triplicates with corresponding standard deviations.

II.2.5. Elemental distribution: micro-X-Ray Fluorescence

A Bruker M4 Tornado µ-XRF mapping system (version 1.3.0.3273, Bruker Nano GmbH, Berlin, Germany) was used for µ-XRF analysis. The instrument was equipped with a micro-focused Rh source (50 kV, 600 µA) with a poly-capillary optic (25 µm spot size). The detection of fluorescence radiation was performed by an energy dispersive detector (silicon drift detector). Data were processed with M4 Tornado Software version 1.3.

XRF spectra for the sapropel mixture were collected under vacuum (2 kPa) with 1 ms/pixel for 5 cycles. The step size for the µ-XRF spatial map was 25 µm and the mapped area on each cryomicrotome-section from sediment pellets measured 13.5 × 13.5 mm, resulting in a total number of 291,600 pixels for each analysis. Since the analyzed map area included parts of the embedding medium along the rim of the cut sediment section, a smaller area of ~17,000 pixels without fractures or regions without sediment was selected to determine the relative abundance of the spectrum elements in weight percent (wt%). Areas of 4 × 4 mm (25,600 pixels) were mapped to evaluate changes of the elemental composition in response to different drying procedures.

µ-XRF analysis of SBB sediment utilized an area of 5.0 × 46.7 mm with a step size of 50 µm (93,400 pixels). XRF spectra were collected under vacuum (2 kPa) with 5 ms/pixel for 4 cycles. Visualization of µ-XRF results was performed using MATLAB R2016a (The MathWorks, Natick, USA) with the Image Processing Toolbox. The enhancement encompassed the following steps: (1) adjustment of brightness and contrast with the *imadjust* function, (2) image binarization with *imbinarize* using the adaptive algorithm, (3) blur with Gaussian filter using sigma = 2 and *imgaussfilt*, and (4) display with the *imagesc* function.

II.2.6. Spatially resolved biomarker analysis: MALDI-FT-ICR-MS

Laser-based lipid biomarker analysis was performed on a 7 T solariX XR FT-ICR-MS coupled to a MALDI source equipped with a Smartbeam II laser (Bruker Daltonik, Bremen, Germany). Data sizes of one megaword were acquired for the mass range m/z 150 – 2000. The FT-ICR-MS was run in continuous accumulation of selected ions (CASI) mode (isolation m/z = 1320; isolation width = 80) to improve the signal to noise ratio (SNR) in the m/z range of isoprenoidal GDGTs. For the eastern Mediterranean sapropel mixture, 900 spectra were generated on every section with a raster width of 200 µm. Each single spectrum was generated by 500 laser shots at a laser frequency of 1000 Hz using a large laser focus with 35% laser power. About 9500 spectra at a raster width of 200 µm were generated on each of the intact sediment

slices from the upper 5 cm of SBB sediment. The number of laser shots, frequency and laser focus were consistent with the settings from the sapropel mixture and laser power was slightly increased to 40% for best signal intensities.

External mass calibration was done using a NaTFA solution (Moini et al., 1998) in electrospray ionization mode followed by an internal lock mass calibration using the m/z value 1314.22636 in DataAnalysis 4.4 SR1 (Bruker Daltonik). This m/z value corresponds to the Na^+ adduct of the GDGT with 5 double bond equivalents, which may include compounds with cycloalkyl rings, double bonds, stereo/constitutional isomers of the major compound crenarchaeol and any possible combinations thereof (Zhu et al., 2013; Liu et al., 2018). To describe that this component is detected on the basis of the accurate m/z value by FT-ICR-MS rather than by chromatographic separation, it will be referred to as GDGT-5_{MS}. In marine environments, the main component of GDGT-5_{MS} is crenarchaeol (Sinninghe Damsté et al., 2002) followed by the isomer (Liu et al., 2018; Sinninghe Damsté et al., 2018). This has been also confirmed by conventional HPLC-MS analysis of sediment extracts from the samples used in this study (data not shown).

For the sapropel mixture, the lock mass calibration improved the average mass accuracy of the GDGT-0 Na^+-ion (m/z 1324.30461) from -1.04 ppm to 0.61 ppm. For the SBB sediment, the highest average deviation of the GDGT-0 Na^+-ion with 6.72 ppm was improved to 2.36 ppm. The used calibration procedure based on infusion of NaTFA covering the m/z range 150 – 2000 and subsequent internal lock mass calibration of each mass spectrum on a known compound in the narrow m/z range of the CASI window is applicable to other biomarkers (Wörmer et al., 2019). The profile spectra were exported from DataAnalysis for further analysis in MATLAB R2015a using a DataAnalysis Script File. To assure high data quality and avoid misjudging the results due to instrumental noise, full profile spectra were filtered for a SNR of the CCaT-relevant GDGTs of ≥8 or, as for the analysis of the SBB sediment slices, used with a 95% data reduction during data acquisition in ftmsControl 2.1.0 (Bruker Daltonik).

The CCaT was calculated for successful spectra (SNR ≥ 8 or 95% data reduction) according to Wörmer et al. (2014). As the CCaT is calculated in this study solely for spectra generated by FT-ICR-MS we expand its definition with the term GDGT-5_{MS}.

$$\text{CCaT} = \frac{\text{GDGT-5}_{\text{MS}}}{\text{GDGT-0} + \text{GDGT-5}_{\text{MS}}}$$

Statistical analysis with SigmaPlot for Windows Version 11.0 (Systat Software, San Jose, CA) included one-way repeated measures analysis of variance with the Holm-Sidak test for pairwise comparison.

II.3. Results and Discussion

The quality of MSI analysis of lipid biomarkers with the option of a congruent elemental mapping with µ-XRF is strongly dependent on sample preparation. In the following the basic requirements of a dry, stable sample with a smooth surface and an undisturbed fine structure have been optimized.

II.3.1. Dehydration: integrity of dimensional and sedimentary fine structure

Oven- and freeze-drying were compared for the preservation of spatial integrity and the sedimentary fine structure prior to embedding. Volume changes resulting from different drying techniques show the advantage of freeze-drying over oven-drying in terms of dimensional stability (Fig. 1A). The volume of the oven-dried pellets was reduced by 54 ± 4% on average, whereas samples frozen at -20 °C and -80 °C and subsequently freeze-dried lost only 5 ± 4.3% and 8 ± 2.4% of their volume, respectively.

Oven-drying, as employed in the initial study by Wörmer et al (2014), resulted in the capillary movement of salty pore water and the accumulation of salt on the sample surface (1st layer), as shown by high contributions of sodium (33 ± 0.6 wt% Na) and chlorine (29 ± 1.2 wt% Cl) (Fig. 1B). Removal of the surface layer exposed a deeper layer (2nd layer) with far lower contents of Na (2 ± 0.3 wt%) and Cl (3 ± 0.3 wt%). In comparison, freeze-drying caused only a minor displacement of brine with limited accumulation of Na and Cl on the dry surface. In the sediment frozen at -20 °C, a change from 4 ± 0.3 wt% to 3 ± 0.5 wt% for Na and 8 ± 0.4 wt% to 6 ± 0.6 wt% for Cl can be observed. The freeze-dried sediment with prior freezing at -80 °C shows slightly larger changes in the Na and Cl contents. The surface layer exhibits Na and Cl contributions of 8 ± 0.3 wt% and 10 ± 0.2 wt%, respectively. In the underlying 2nd layer the amount of Na decreases to 4 ± 0.1 wt% and the content of Cl to 6 ± 0.4 wt%. Freeze-drying is thus recommended for superior dimensional and elemental stability. For the following experiments freeze-dried sediments frozen at -20 °C were used.

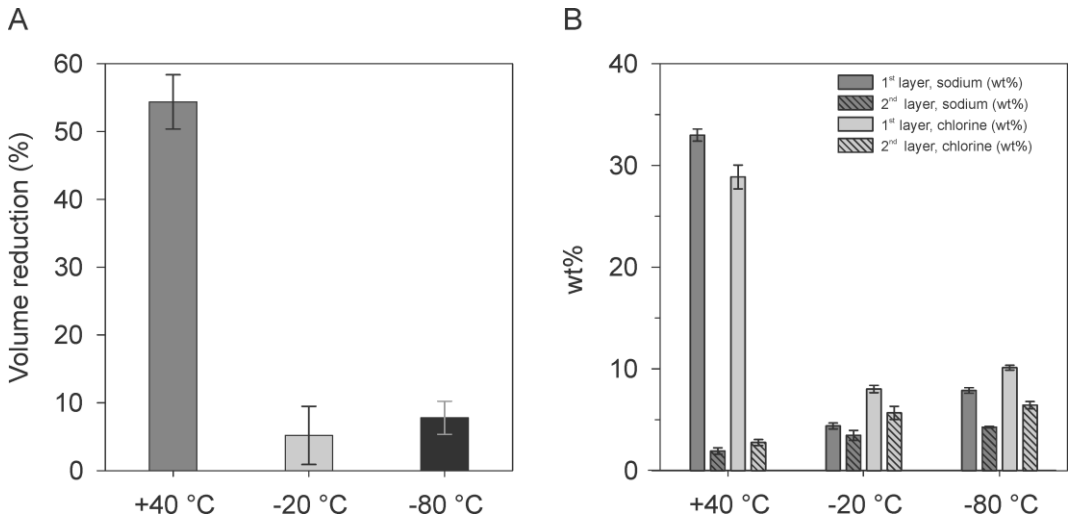

Fig. 1: *Volume reduction (A) and change in the contributions of sodium and chlorine on the sediment surface after drying (1st layer) and on the underlying 2nd layer (B). The presented results are averages of triplicate measurements with corresponding standard deviations.*

II.3.2. Sediment embedding for MSI

Freeze-dried sediments do not exhibit a high stability during handling and easily disintegrate when attempting to obtain thin sediment slices. Therefore, embedding the sediment in MSI-compatible media was considered to improve the preparation of sediment samples and assist sectioning with a cryomicrotome. To find an optimal embedding medium for MALDI-MSI of sediments, eleven different media were tested (Table 1). A study by Nelson et al. (2013) described a broad variety of solvent-free media for the embedding of whole-body zebrafish and served as a guide for our initial choice of embedding media.

The properties and impact of different media on sample integrity are described in Table 1. Media properties are generally described for each frozen medium. A description of the liquid medium is offered only if it had a noteworthy effect on the embedding quality, i.e., when high viscosity caused incomplete embedding. In general, all frozen media were semi-hard to hard. Stability of the sediment describes its integrity from the moment it was placed into the medium. This criterion ranges from 'disintegrated' (i.e. crumbling of the sediment pellet and formation of a slurry) to 'partially disintegrated' (i.e. slight disintegration near the rims of the pellet), to 'stable'. In some cases, incomplete embedding was observed. Sediment pellets did not sink into 5% CMC mixed with gelatin. The high viscosity of 10% gelatin with 2% CMC prevented embedding of the inner part of the sediment pellet, which led to disintegration during the subsequent sectioning with a cryomicrotome. Amenability to cryomicrotome sectioning, quality of slices when drying on ITO slides, and overall media suitability are listed separately (Table 1). Only gelatin and gelatin-CMC mixtures yielded sufficient stability of embedded samples. Pure gelatin, either 5% or 10%, and a mixture of 5% gelatin with 2% CMC maintained structural integrity for slices prepared by

cryomicrotome sectioning. Section quality of pure gelatin-embedded sediment increased after adjusting the cryomicrotome temperature from -20 °C to -15 °C.

Mounting of slices prepared by cryomicrotome sectioning on ITO slides and subsequent drying revealed the disadvantage of pure gelatin over 5% gelatin mixed with 2% CMC. The gelatin-only embedded sections failed to adhere to the ITO slide due to flaking of the gelatin, whereas the 5% gelatin +2% CMC mixture had optimal properties in terms of sediment stability during embedding, sectioning quality and adhering to ITO slides.

None of the tested gelatin and CMC-based media exhibited ion-suppression (Nelson et al., 2013) and thus they are all suitable for embedding. We additionally performed an MSI measurement over an area of about 650 spectra covering the embedding media and the sediment sample (Fig. 2A) to assess the specific influence on ionization and detection of GDGTs. The images of ion abundances corresponding to Na^+-adducts of GDGT-5_{MS} and GDGT-0 in Fig. 2B visualize the clear localization of these components in the sample. Thus, the embedding procedure did not delocalize the biomarkers in the embedding media. The comparison of the average spectra acquired from embedding media without sediment (upper panels in Fig. 2C and D) and the sample (lower panels in Fig. 2C and D) demonstrates the suitability of the mixture of gelatin (5%) and CMC (2%) for sample stabilization. The embedding media had no influence on ionization and detection in the high m/z range (>1000), which is crucial for the analysis of GDGTs (Fig. 2C). The average broadband mode spectra of embedding media without sediment exhibit minor contributions in the lower m/z range that need to be taken into account in future analyses of smaller target molecules (Fig. 2D).

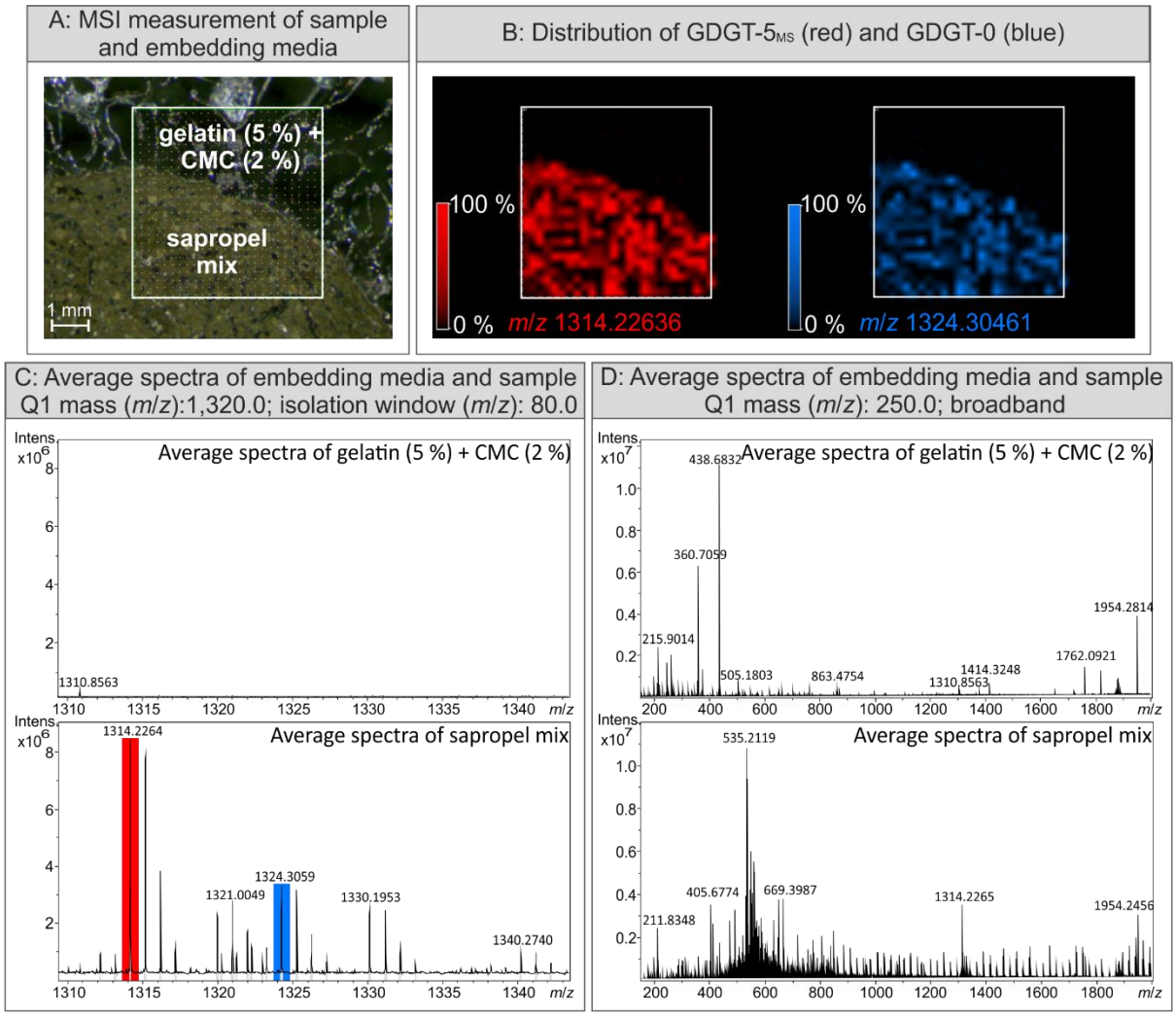

Fig. 2: *Influence of embedding media on ionization and detection of GDGTs. A: MSI measurement area. B: Images of the abundance of the m/z value of the Na⁺-adduct corresponding to GDGT-5$_{MS}$ (red) and GDGT-0 (blue). C: Average spectra of embedding media (upper spectra) and sample (lower spectra) acquired in continuous accumulation of selective ions (CASI) mode with quadrupole 1 set to 1,320 (m/z) with an isolation window of 80 (m/z). The m/z values of CCaT-relevant GDGTs as Na⁺-adducts are highlighted in their corresponding colors. D: Average spectra of embedding media (upper spectra) and sample (lower spectra) acquired in broadband mode with quadrupole 1 set to 250 (m/z).*

II.3.3. Section thickness and its influence on congruent elemental and biomarker analysis

The embedded sediment pellets were sectioned into sub-mm slices with a cryomicrotome. Overall six different thicknesses (20, 60, 100, 150, 200, 500 µm) were prepared in triplicate and analyzed by µ-XRF and MALDI-FT-ICR-MS to evaluate the influence of the section thickness on both analytical methods (Fig. 3). Slicing of round sediment pellets with the cryomicrotome caused stretching of sections thicker than 100 µm to an oval shape (Fig. 3D).

Non-destructive µ-XRF was used for characterizing embedded sediment prior to applying MSI to detect the two major GDGTs. In comparison to MALDI, with an estimated penetration depth of ~1 µm, the penetration depth in µ-XRF analysis is largely dependent on the X-ray energy. The intensity and response depth of the emergent fluorescent radiation is closely linked to the atomic number, with progressively increasing response depth for heavier elements (Croudace and Rothwell, 2015). Therefore, section thickness for µ-XRF analysis must exceed a certain threshold to limit or avoid signal contributions from the sample holder.

Elemental compositions (in wt%) for different section thicknesses are compared with the signal produced from an empty ITO slide and a ~1 cm thick reference sediment pellet in Fig. 3A. Even though the sediment can always be differentiated from the background signal of the ITO slide, a relatively constant elemental composition of embedded slices on ITO slides resembling the sediment reference was only observed in sections ≥100 µm.

Section thickness and its influence on the quality of lipid biomarker data was evaluated by the consistency of CCaT data and signal intensity of GDGT-0 and GDGT-5_{MS} (Fig. 3B and C, respectively). Section thickness had no significant influence on the difference between calculated CCaT values ($P = 0.244$) and the number of successful spectra ($P = 0.464$) (Fig. 3B). The MALDI-based CCaT, which varied between 0.651 (20 µm) and 0.655 (200 µm), as well as the proportion of successful spectra, with 80.5% (500 µm) to 89.3% (60 µm), are both highly consistent. The success rate even exceeded the rate reported by Wörmer et al. (2014) who observed ~75% of successful spectra in a S1 layer.

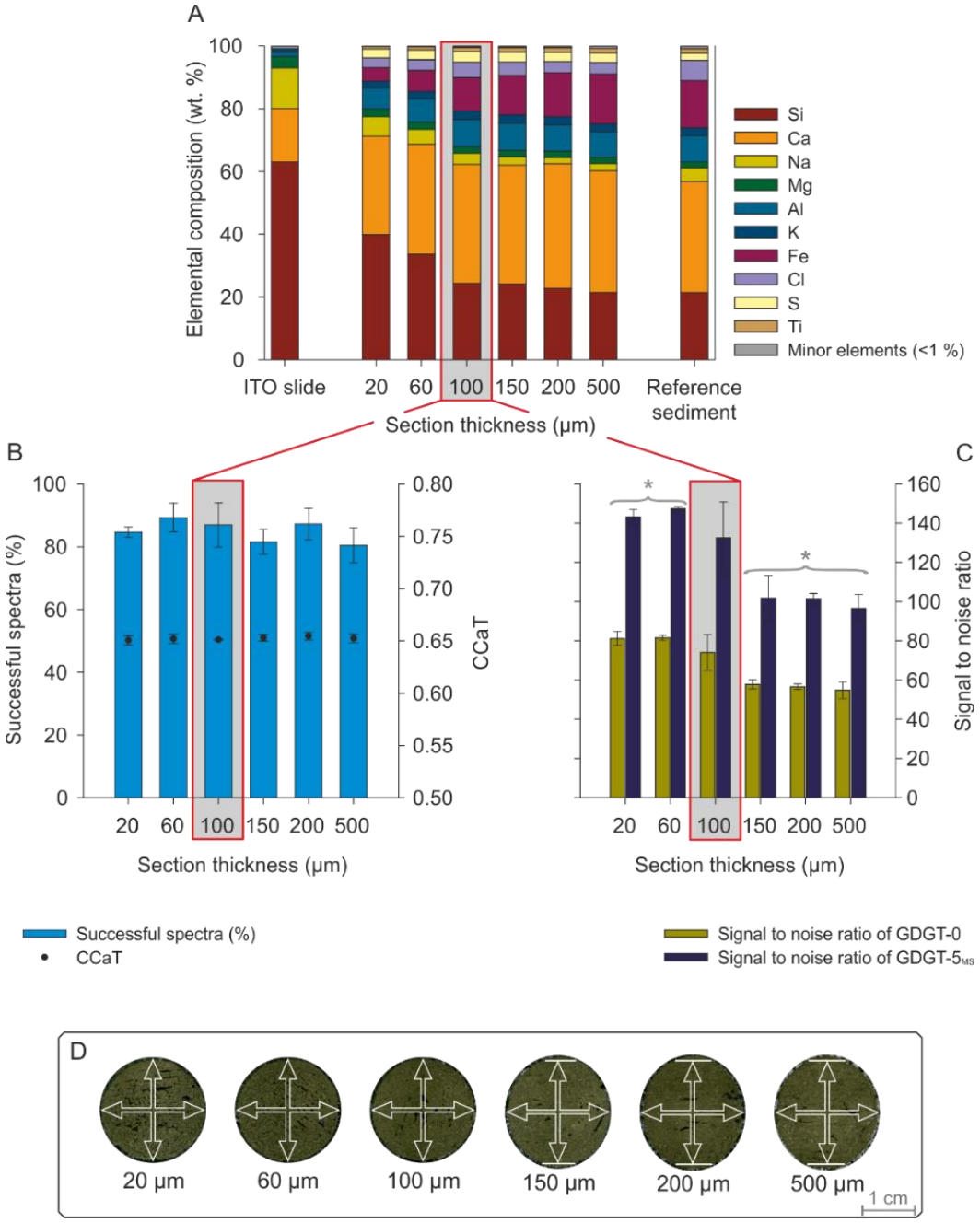

Fig. 3: *Influence of section thickness on µ-XRF (A) and MALDI-FT-ICR-MS (B, C) analyses and on dimensional stability of slices (D). Grey boxes indicate the optimal section thickness for combined molecular and elemental imaging analysis. The indium tin oxide (ITO) coated glass slide in A is the background µ-XRF signal of the sample holder and a ~1 cm thick sediment pellet serves as the µ-XRF reference for the elemental composition of the sapropel mix. Successful spectra (B) are defined as spectra in which GDGT-0 and GDGT-5$_{MS}$ are detected with a signal to noise ratio of ≥ 8. About 900 spectra per section were generated by MALDI-FT-ICR-MS. * in C shows section thicknesses for which no significant differences could be observed according to post hoc pairwise comparison (Holm-Sidak). Samples were prepared and analyzed in triplicate. The presented results are average values of triplicates with corresponding standard deviations. D shows the round-shaped slices derived from embedded sapropel mix sliced with a cryomicrotome to thicknesses from 20 to 500 µm. The arrows indicate the stretching from circular to oval slices with thicknesses ≥ 150 µm. The resulting excess is indicated by horizontal white lines.*

Signal intensities, represented as average SNRs (Fig. 3C), are highest for the 20 and 60 µm sections with values of ~145 for GDGT-5_{MS} and ~80 for GDGT-0. The thicknesses of these two sections yield highly similar results and the pairwise comparison procedure (Holm-Sidak method, overall significance level 0.05) shows no significant difference for GDGT-0 and GDGT-5MS. However, thicker sections show a decrease in SNR values. Slightly lower SNR values of 74 (GDGT-0) and 132 (GDGT-5_{MS}) were recorded for the 100 µm section, while for sections thicker than 150 µm SNRs decrease to ~55 (GDGT-0) and ~100 (GDGT-5_{MS}). The SNRs of sections with thicknesses of 150, 200, and 500 µm show no statistically significant difference.

In contrast, the different SNR of the 100 µm section represents an intermediate case between the high SNRs of the thin and the lower SNRs of the thicker sections. The weaker performance of thicker sections might be a result of an insulating effect between the sediment and the conductive ITO slide. Similar results have been shown for the detection of proteins in mammalian tissue by Sugiura et al. (2006). They recommend sections with 5 – 20 µm thickness for low molecular weight proteins (m/z 3000 – 9000) and even thinner sections (< 5 µm) for high molecular weight proteins (m/z > 9000). Considering the experiences from biological tissues, thinner sediment sections could result in even higher detection efficiency, but sample handling, especially section stability, would be drastically affected for sediment sections <20 µm. Thus, for MSI of sediments, section thicknesses between 20 µm and 60 µm are suggested for the biomarker analysis with MALDI-FT-ICR-MS. In combination with elemental mapping by µ-XRF, a section thickness of 100 µm is needed to produce reliable results with both methods.

II.3.4. Sequence of sample preparation

We propose the following optimized sample preparation sequence for imaging of lipid biomarkers and congruent elemental mapping (Fig. 4). The sediment core should ideally be sampled with a double-L (LL) channel (Nakagawa and Suigetsu 2006 project members, 2014). X-radiography is recommended for visualization of possible laminae and their orientation in the sediment. Afterwards, ~5 cm long subsamples are frozen and freeze-dried, followed by embedding in a mixture of 5% gelatin and 2% CMC. While cutting thin sections with the cryomicrotome, the section thickness needs to be chosen depending on the analyses to be performed. As µ-XRF results are more reliable for thicker samples, 100 µm thick sections are a good compromise for obtaining congruent elemental and biomarker imaging data of high quality. However, it is recommended to obtain an additional µ-XRF analysis of the same sediment as reference before embedding and sectioning. For analysis of isoprenoidal GDGTs without parallel µ-XRF analysis, thinner sections of 20 – 60 µm are beneficial in terms of signal intensity.

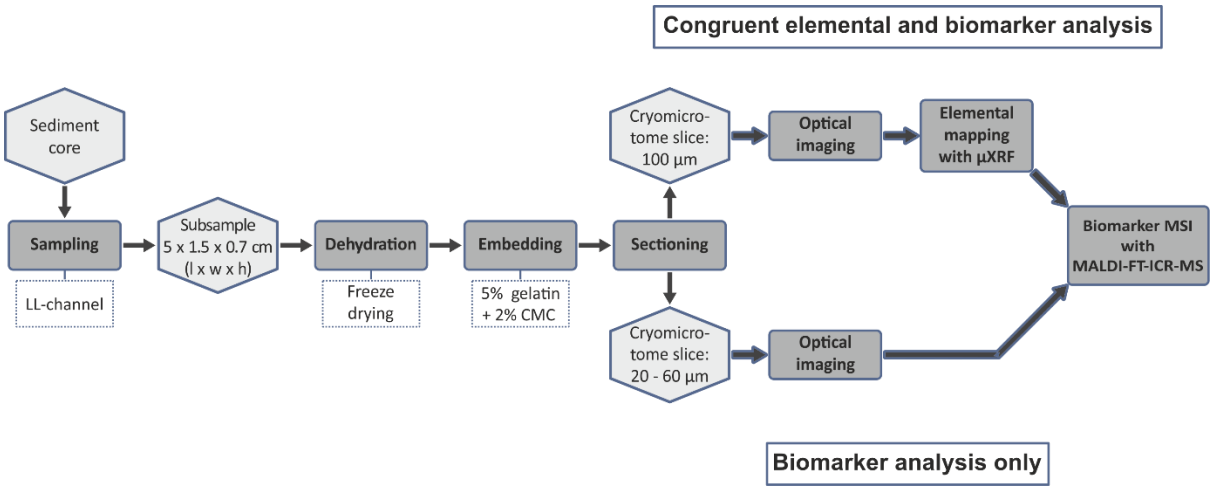

Fig. 4: *Proposed sequence of sample preparation for optimized analysis of isoprenoidal GDGTs with the option of non-destructive µ-XRF analysis prior to MSI to achieve congruent elemental and biomarker information.*

II.3.5. Sequential ultra-high-resolution CCaT records

The uppermost ~5 cm of SBB box core SPR0901-05BC was used to illustrate the proposed sample preparation for MSI of intact sediment samples. The sediment slab of the box core was subsampled using an LL-channel and X-radiographed for accurate visual identification of laminae (Schimmelmann et al., 1990; Pike and Kemp, 1996). Mineral-rich laminae with a reduced porosity are shown as dark bands on the positive contact print of the X-radiograph (Fig. 5A). Correlation of the X-radiographic pattern with diagnostic laminae from older, dated SBB cores suggests that the bottom of this section dates to about 1995. Cryomicrotome slices of this sediment section were prepared with a thickness of 100 µm for elemental analysis, and two 60 µm slices for biomarker analysis. Scanning time for the µ-XRF analysis was about 45 min and the ~9500 spectra recorded on each slide with MALDI-FT-ICR-MS required about 4 h.

Calcium (Ca) and silicon (Si) are associated with organisms that produce $CaCO_3$ and biogenic silica respectively, whereas titanium (Ti) is derived from mineral detritus. Elemental ratios such as Ca/Ti and Si/Ti will be used to trace depositional changes of terrigenous and biogenic sources in the SBB (Hendy et al., 2015) and will thus establish an independent layer of information that complements the molecular record. Fig. 5D shows the normalized µ-XRF images of Ca/Ti and Si/Ti of the 100 µm cryomicrotome slice. The results visualize how higher values of both ratios coincide with predominantly biogenic laminae of the sediment, shown by light colors of the image recorded by µ-XRF (Fig. 5C). Moreover, the images show that laminae are slightly tilted as a result of subsampling from the box core. In addition to the paleoenvironmental information to be gleaned from µ-XRF-derived elemental data, these can provide useful

independent support in establishing an age model in settings such as the SBB where the annual laminae in the analyzed sample specimen are often hard to identify by visual inspection.

The digital data from high-resolution molecular and elemental analysis will need to be further processed and transformed into a down-core profile by averaging along the horizontal layers. One promising option is image warping of the X-radiograph picture and applying the resulting transformed matrix on the subsequent elemental and biomarker data from µ-XRF and MALDI-FT-ICR-MS, respectively. For illustrative purposes, we applied a shifting vector with a slope of 0.4, which transforms the inclined horizon into one that is almost perpendicular to the depth (length) axis (Fig. 5C). In-depth description of the extensive data processing routines would go beyond the aim of this manuscript, which is intended to focus on the analytical front end, i.e., sample preparation.

MSI data for the CCaT-relevant GDGTs of the two sequential cryomicrotome slices indicate 85.2% and 83.8% yields of successful spectra for slices A and B, respectively. Visualization of the CCaT proxy on the slices (Fig. 5E) shows the positioning of congruent CCaT values along the inclined laminae of the sediment. Thus, applying the horizontal transformation, according to the X-ray and µ-XRF results, leads to an almost horizontal distribution of the CCaT values (Fig. 5E). The resulting CCaT data of the two slices can be used to create downcore profiles, as values are averaged along the quasi-horizontal layers with 200 µm resolution. To increase the data quality, CCaT values were only averaged if ten or more values were available per horizon (cf. Wörmer et al., 2019).

The reproducibility of data can be assessed by replicates in the form of different slices. The 2D distribution (Fig. 5E) and downcore profiles at 200 µm resolution of two slices closely resemble each other (Fig. 5F); matching the two downcore profiles without any additional tie points using the software AnalySeries 1.1 (Paillard et al., 1996) results in a correlation coefficient of 0.769.

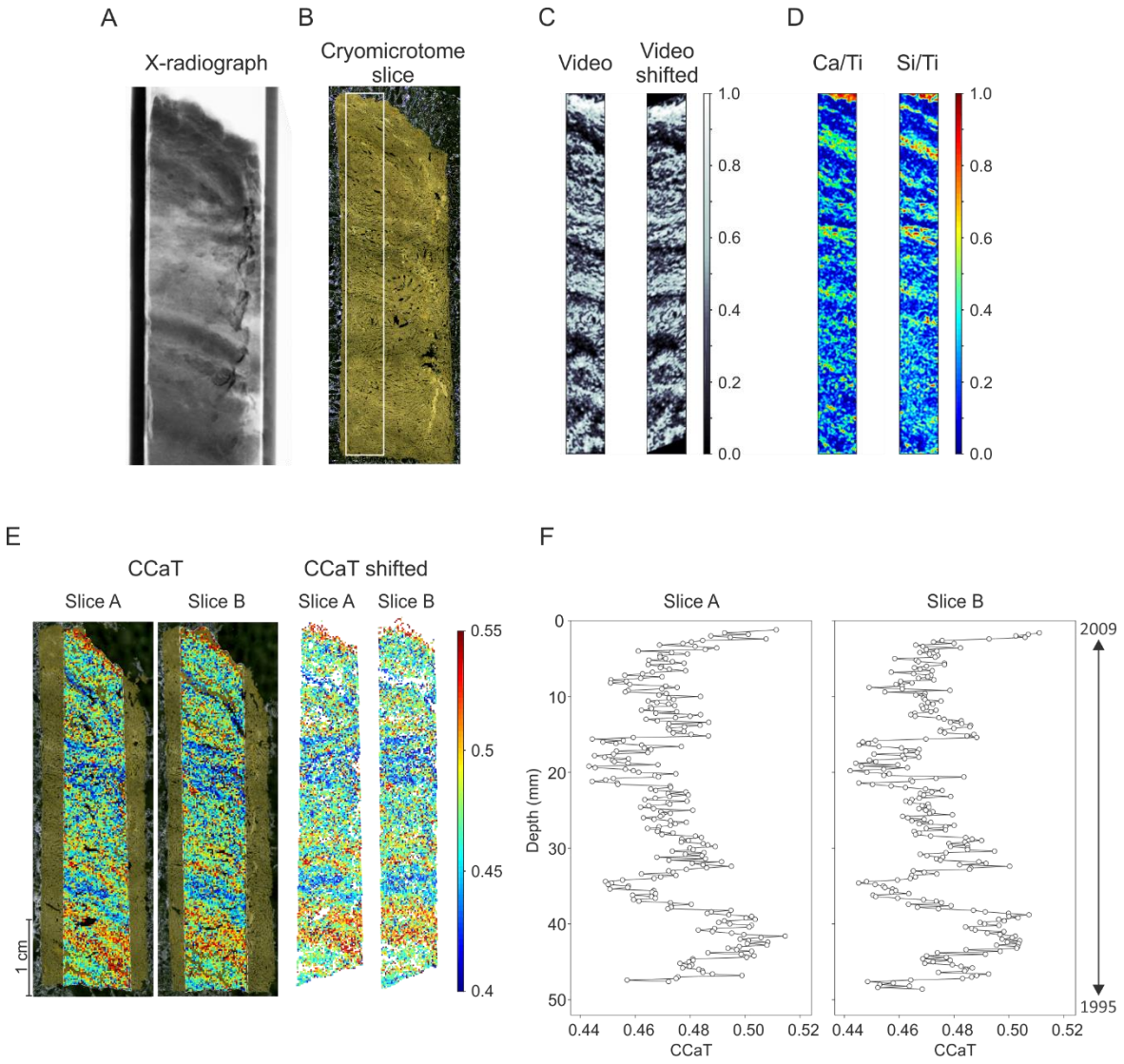

Fig. 5: *Congruent elemental and biomarker analyses of the uppermost ~5 cm of SBB core SPR0901-05BC. (A) X-radiograph (positive) of the subsample taken with a LL-channel. (B) 100 µm cryomicrotome slice and µ-XRF measurement area (white rectangle). (C) Video image recorded by µ-XRF and further processed using MATLAB with original (left) and horizontally shifted (right) layers. (D) Distribution of normalized µ-XRF-derived elemental ratios. (E) Original distribution of CCaT values on two 60 µm sediment slices (left) and horizontally shifted (right). (F) 200 µm resolution downcore CCaT profile from sequential cryomicrotome slices (slices A and B). CCaT values were averaged for horizons with at least ten CCaT values. The time interval most likely covered in this sediment section is indicated by the arrow in F.*

The significance of the CCaT profile will require further study since, as for TEX_{86} (Pearson and Ingalls, 2013; Schouten et al., 2013), not just temperature (Wörmer et al., 2014) influences the ratio. Indeed, the influence of growth rate, already observed for TEX_{86} (Hurley et al., 2016), appears to be amplified for CCaT (Evans et al., 2018), making this ratio potentially more sensitive to changes in upwelling intensity and possibly useful for tracking changes in the nutrient availability connected with upwelling regimes and thus ENSO variability. Additionally, through

the wide distribution of GDGT-0 among archaea, the CCaT may be more sensitive to varying archaeal lipid sources than the TEX_{86}, which is based on the minor GDGTs thought to be taxonomically specific for marine planktonic archaea (Schouten et al., 2002), in particular the Thaumarchaeota.

Earlier conventional TEX_{86}-based SSTs in the Santa Barbara Basin recorded colder than instrumental SSTs, which was explained by production in subsurface waters (Huguet et al., 2007). Using the CCaT-SST transformation from Wörmer et al., (2014), the CCaT values in the 200 µm resolution downcore profile correspond to SSTs from 10.4 °C to 15.3 °C. As in the study by Huguet et al. (2007), this is slightly lower than seasonally averaged instrumental temperatures for 0 – 25 m water depth of the SBB. For the 1995 – 2009 period these vary between 10.8 and 21.0 °C (CalCOFI, 2018).

To what degree the CCaT record is influenced by production of Thaumarchaeota in subsurface waters (cf. Huguet et al., 2007) and/or by factors such as ammonium supply (Evans et al., 2018) cannot be addressed in this study. However, considering that the analyzed core section originates from a box core retrieved in 2009 and comprises about 14 years, we suggest that the maximum observed SST in both slices at ~40 mm (Fig. 5F) represents the 1997/1998 El Niño event when reduced upwelling caused elevated SST (Schimmelmann and Lange, 1996; Schimmelmann et al., 2016).

The exemplary 200 µm resolution record demonstrates the potential of MSI of marine sediments for ultra-high-resolution paleoclimate studies. Future temporal extension of the record and, for example, combination of several SST sensitive proxies (e.g., CCaT, TEX_{86}^{L} (Kim et al., 2010)) and the alkenone-based $U_{37}^{K'}$ at µm-scale resolution will provide unprecedented insights into the formation of the proxy signal and might help to achieve a better understanding of the sensitivity of the cyclization of isoprenoidal GDGTs to environmental factors other than SST. For the SBB, Kennedy and Brassell (1992) showed that the $U_{37}^{K'}$ can be used to identify El Niño events. Their study was based on one of the most highly resolved molecular stratigraphic sampling approaches with an average sampling frequency of 3 mm and thus annual resolution. By contrast, MSI with its 200 µm resolution will result in roughly monthly resolution.

II.4. Conclusions

This study establishes an optimized sample preparation sequence for analysis of archaeal tetraether lipids with MALDI-FT-ICR-MS, as well as for the acquisition of congruent elemental and biomarker information. The proposed preparation improves the dimensional and elemental stability of the sediment sample. Compared to the first application of MSI in marine sediments (Wörmer et al., 2014), the freeze-drying step prevents the sediment from shrinking and thus preserves the original depth to age correlation of the sediment. Additional embedding of freeze-dried sediment allows cryomicrotome sectioning into thin sediment slices ideally suited for biomarker MSI and also applicable to non-destructive µ-XRF analysis prior to MSI. Combining these two spatially highly resolved methods on the same sediment section provides detailed information on the sediment structure, its depositional setting and the interdependence between lipid biomarkers and the sedimentary matrix. Besides the observation that thin cryomicrotome slices improve signal intensities of MSI, the developed protocol is also transferable to other biomarkers of interest and allows the application of matrices on the sample surface by conventional spraying or sublimation techniques. By generating multiple congruent thin slices, replication of experiments and parallel analyses of multiple biomarkers from the same sample are possible. Replicate 200 µm resolution CCaT records obtained from the uppermost ~5 cm of sediment from the Santa Barbara Basin showed remarkable similarity and demonstrated the reproducibility of MSI of marine sediments and its ability to capture high frequency environmental variations.

Acknowledgments

The authors thank Corinna Henkel, Matthias Witt and Jens Fuchser from Bruker Daltonik Bremen for their support with sample preparation including the use of their laboratory infrastructure at an early stage of the experimental design. Special thanks to Jürgen Pätzold for support with the X-radiographs. The study was funded by the European Research Council under the European Union's Horizon 2020 Research and Innovation Programme (grant agreement No. 670115 ZOOMECULAR; PI Kai-Uwe Hinrichs). The µ-XRF system was financed by the Deutsche Forschungsgemeinschaft with funds dedicated to the acquisition of large instrumentation granted to the University of Bremen in the framework of the Excellence Initiative. We thank Jaap Sinninghe Damsté and Jaime Toney for their constructive comments and suggestions that helped to improve an earlier version of this manuscript.

CHAPTER III

TOWARDS MULTIPROXY, ULTRA-HIGH RESOLUTION MOLECULAR STRATIGRAPHY: ENABLING LASER-INDUCED MASS SPECTROMETRY IMAGING OF DIVERSE MOLECULAR BIOMARKERS IN SEDIMENTS

Lars Wörmer[a*], Jenny Wendt[a], Susanne Alfken[a], Jin-Xiang Wang[a], Marcus Elvert[a], Verena B. Heuer[a], Kai-Uwe Hinrichs[a]

Published in *Organic Geochemistry*

Vol: 127 January 2019, pages 136-145,

https://doi.org/10.1016/j.orggeochem.2018.11.009

[a] Organic Geochemistry Group, MARUM – Center for Marine Environmental Sciences and Faculty of Geosciences, University of Bremen, Leobener Str. 8, 28359 Bremen, Germany

* Corresponding author: E-mail address: lwoermer@marum.de

Abstract

Mass spectrometry imaging (MSI) collects mass spectra of organic compounds from individual micrometer-sized spots and yields high-resolution images of the spatial distribution of target analytes on sample surfaces. MSI can potentially open a new avenue to ultra-high resolution molecular stratigraphy by resolving the fine-scale distribution of molecular biomarkers in geological records. However, ionization of organic molecules within their sediment matrix remains a critical challenge. Building on the recent introduction of MSI of archaeal tetraether lipids, we have extended the analytical spectrum to additional biomarkers and provide guidelines for the generation of multiproxy, ultra-high resolution paleoenvironmental records. We evaluated the addition of artificial matrices to promote ionization, defined the most suitable MS settings, and increased analytical complexity from pure compounds to their investigation in sediment. Most compounds relevant to molecular stratigraphy are not properly ionized in the presence of conventional matrices, but require atypical ones, such as those based on carbon or silver. Sediments serve as a natural matrix, directly allowing detection of many of these compounds. However, the sediment matrix also inhibits some reactions that otherwise promote detection, such as derivatization of alkenones or silver-mediated ionization of *n*-alkanes. The robustness of MSI-based molecular stratigraphy is enhanced by analysis of target compounds in narrow m/z ranges, and by summation of mass spectra from several coeval measurement spots. We present an initial inventory of compounds readily detected in the sediment tested, including long chain alkenones and diols, sterols, and pigments, and provide an outlook into the use of MSI in multiproxy studies.

III.1. Introduction

Mass spectrometry imaging (MSI) has gained relevance as a technique that visualizes the detailed, sub-mm spatial distribution of analytes, thus enabling the exploration of target compounds at an unprecedented fine scale and level of detail. Initially developed mainly for applications in life science, it has now closed the gap to a diversity of fields, and it is also firmly established in microbiological research (Watrous and Dorrestein, 2011). In the field of geobiology, (Thiel et al., 2007a; Thiel et al., 2007b) pioneered the notion that archaeal lipids are spatially traceable from carbonate microbialites or microbial mats at high resolution using time-of-flight secondary ion mass spectrometry (ToF-SIMS). Following this line of investigation, we recently introduced MSI for the reconstruction of annual-to-decadal changes in sea surface temperatures (SST). We analyzed the environmental information archived in archaeal glycerol dialkyl glycerol tetraether (GDGT) lipids and their fine-scale spatial analysis in marine sediment cores with matrix-assisted laser desorption/ionization coupled to Fourier transform-ion cyclotron resonance-mass spectrometry (MALDI-FT-ICR-MS; Wörmer et al., 2014). This technique is based on the laser-induced desorption of the analyte from the sediment matrix, its subsequent ionization due to primary and secondary ionization processes in the ion plume (Dreisewerd, 2003; Knochenmuss and Zenobi, 2003) and its detection by ultra-high resolution mass spectrometry. When the finely focused laser beam scans across the targeted sample section, individual mass spectra are recorded for every micrometer-sized spot.

While our initial MALDI-FT-ICR-MS study focused on only one group of organic molecules, a wealth of compound classes exists that can be used as diagnostic biomarkers for environmental conditions and processes, to describe the composition of microbial communities or to provide evidence for biogeochemical reactions (Table 1). Qualitative, quantitative and isotopic analyses of such molecular biomarkers in well-dated sedimentary records open a window to past environments and ecosystems (i.e., molecular stratigraphy; Brassell et al., 1986).

While conventional analysis of these biomarkers is hampered by the requirement for relatively large, cm-sized samples, the µm resolution of MSI may reveal fine-scale temporal variability of past environments. In combination with other spatially resolved techniques, it may also prove effective in understanding the mechanisms underlying signal deposition and transformation into long-term sedimentary archives. However, MSI of lipid biomarkers in geological samples is still at its initial stage, ionization of chemical species within their natural sediment matrix remains a critical challenge, and methods need to be developed ab initio for various compound classes that are relevant to paleoenvironmental reconstruction (Table 1, Fig. 1). So far, these relatively persistent compounds have escaped the interest of MSI in other

scientific fields, where the focus resides in the more polar, functionalized and reactive intact polar lipids, proteins or metabolites (e.g. Zaima et al., 2010).

Table 1: *Selection of molecular biomarkers investigated in this study and their use as environmental proxies in sedimentary systems.*

Compound class	**Structure ID (Figure 1)**	**Proxy potential (selected):**	**Selected references**
n-Alkanes	1	Paleovegetation, terrigenous input	Eglinton and Hamilton (1967); Cranwell (1973); Volkman et al. (1980); Pancost and Boo (2004)
PAHs	2	Natural or anthropogenic combustion	Youngblood and Blumer (1975); Lima et al. (2005)
Sterols	3	Ecosystem structure, source indicator, paleoredox conditions	Nishimura and Koyama (1977); Huang and Meinschein (1979); Volkman (1986); Wakeham (1989)
Long-chain alkenones	4	SST	Brassell et al. (1986); Prahl and Wakeham (1987)
Long-chain diols	5	SST, ecosystem structure, riverine input	Versteegh et al. (1997); Rampen et al. (2012); Lattaud et al. (2017)
GDGTs	6,7	SST, terrigenous input	Schouten et al. (2002); Hopmans et al. (2004); Talbot and Farrimond (2007); Weijers et al. (2007)
BHPs	8	Bacterial community composition	Talbot and Farrimond (2007)
Fatty acids	9	Ecosystem structure, source indicator	Perry et al. (1979); Volkman et al. (1980); Kaneda (1991)
Carotenoids and pheopigments	10, 11	Ecosystem structure, primary productivity	Sanger (1988); Repeta et al. (1989); Bianchi et al. (2000)

Abbreviations: PAH, polycyclic aromatic hydrocarbon; GDGT, glycerol dialkyl glycerol tetraether; BHP, bacteriohopanepolyol; SST, sea surface temperature. For structure ID, see Fig. 1.

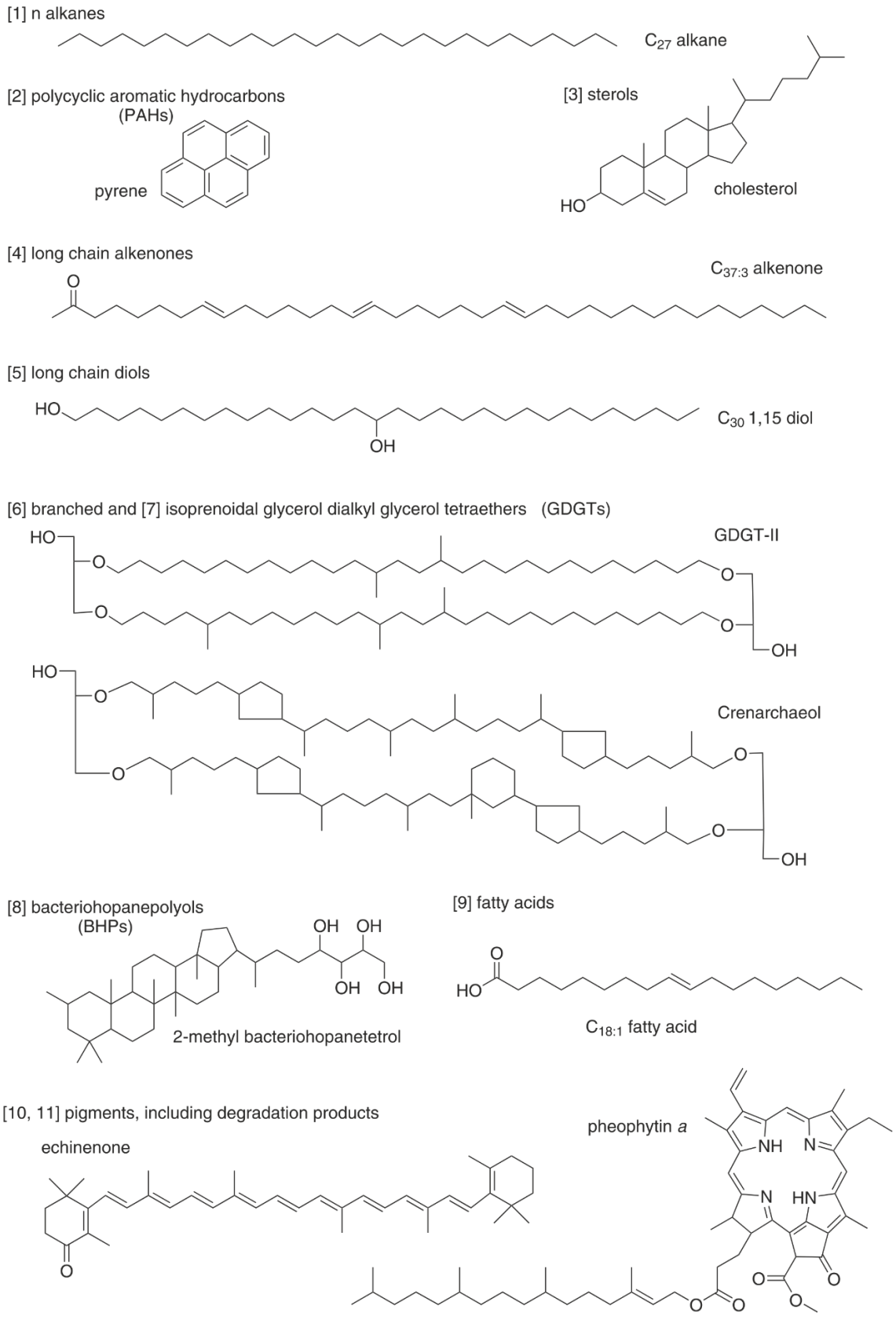

Fig. 1: *Chemical structures corresponding to a selection of molecular biomarkers investigated in this study. Numbering corresponds to table 1.*

The present study aimed to enable MSI for lipid biomarkers that bear information on paleoenvironments. Using samples of different complexity, ranging from pure standards to environmental samples, we specifically optimized laser-based desorption and ionization, as well as mass spectrometric detection. The successful application of the optimized MSI method for the investigation of Santa Barbara Basin (SBB) sediment demonstrates its potential for ultra-high resolution molecular stratigraphy and for constraining the interrelationship between physical forcings such as SST and aquatic ecosystem properties with unprecedented temporal resolution.

III.2. Material and Methods

III.2.1. Sediment samples

Pure standards for the investigated molecular biomarkers were purchased from Sigma-Aldrich, Fluka, Dr. Ehrenstorfer GmbH and Cayman Chemical (see Supplementary Table S1 for detailed information). Prof. Roger Summons (Massachusetts Institute of Technology, Cambridge, MA, USA) kindly provided bacteriohopanepolyol (BHP) standards and Prof. Ian Bull (University of Bristol, UK) the long-chain alkenone standards. GDGTs were purified in our laboratory by preparative HPLC from an *Archaeoglobus fulgidus* culture.

A sediment test sample for method optimization was prepared by pooling different organic-rich sapropel layers from a gravity core retrieved in the eastern Mediterranean Sea (Site GeoB15103; Zabel et al., 2012). A sapropel section had been previously analyzed for GDGTs by MALDI-FT-ICR-MS (Wörmer et al., 2014) and these samples were thus considered ideal for the development and testing of biomarker MSI. We used the solid sample to investigate biomarker detectability in the sediment matrix and a lipid extract to assess the precision of the MSI signal. The final methods were applied to the uppermost ~5 cm of an intact slab of laminated sediment from the SBB (Box core SPR0901-05BC; Arndt Schimmelmann) in order to demonstrate their potential for ultra-high resolution molecular stratigraphy.

MSI generally relies on the addition of artificial matrices to aid desorption and ionization. In the present study we tested two of the most frequently employed MALDI matrices, namely 2,5-dihydroxybenzoic acid (DHB) and α-cyano-4-hydroxycinnamic acid (HCCA). As opposed to these conventional matrices, we also tested more unconventional ones: graphite, fullerite (as a combination of C_{60} and C_{70}) and silver nitrate ($AgNO_3$). Previous studies, for example, dealing with plant tissue or crude oil, had identified carbon materials and silver-based additives to be suitable for the analysis of carbohydrates (Gholipour et al., 2008), sterols (Montsko et al., 2009; Perdian et al., 2010)), fatty acids (Cha et al., 2008; Cha et al., 2009) and *n*-alkanes (Dutta and Harayama, 2001; Cha et al., 2008). All matrices were obtained as solids from Sigma Aldrich. Girard-T, a

derivatization reagent efficient in the in situ derivatization of ketone groups (Kim et al., 2015), was also obtained from Sigma-Aldrich.

III.2.2. Biomarker MSI – sample preparation

III.2.2.1. Preparation of pure compounds for MSI

Pure standards of 45 compounds (see Supplementary Table S1) were tested for their ionization with different matrices and analyzed in positive and negative ionization mode. Two conventional matrices (DHB, HCCA), two unconventional ones (graphite, $AgNO_3$) and one derivatization agent (Girard-T) were used. The standard dried droplet method was chosen for sample application to a Bruker multi-well target plate (MSP 96 target polished steel BC, Bruker Daltonik). In short, 10 µL of the standard (10 µg mL^{-1}) dissolved in a suitable solvent were mixed with an equal volume of matrix.

We observed that a matrix concentration of 1 mg mL^{-1} already resulted in high peak intensities for target compounds, while minimizing the risk of ion suppression. The resulting matrix:analyte ratio of 100:1 is at the lower end of the range typically employed in MALDI analysis (Hillenkamp et al., 2014). Girard-T was applied in a concentration of 5 mg mL^{-1} in combination with DHB (1 mg mL^{-1}). The DHB, HCCA and graphite matrices were further doped with NaCl to a final concentration of 1 mM to aid ionization and promote formation of Na+-adducts in positive mode. The standard matrix mixture (0.7 µL) was then applied as a single drop and allowed to completely dry before analysis. For each treatment and analysis mode, three such droplets were prepared and measured.

III.2.2.2. Preparation of the total lipid extract for MSI

In order to determine the precision of biomarker MSI, a lipid extract obtained from the sapropel test sample (see Section 2.4 for extraction protocol) was sprayed on an aluminum plate. The lipid extract was applied with an ImagePrep system (Bruker Daltonik), a matrix deposition device that uses vibrational vaporization technology to provide fully automated and highly reproducible matrix preparations for MALDI. Three concentration levels were used, resulting in a theoretical amount of targeted crenarchaeol of 1.44, 14.4 and 144 fg per spot.

III.2.2.3. Preparation of sediment samples for MSI

In order to explore the analyzability of natural biomarker mixtures, the sapropel test sample was prepared for MSI as described in Alfken et al., (2019). In short, sediment pellets were formed with cut 10 mL syringes. These pellets were frozen and freeze-dried, embedded in a gelatin-carboxymethyl cellulose mixture and sectioned into a series of 60 µm slices on a cryomicrotome (HM 505 E Cryostat). The slices were deposited on indium-tin oxide (ITO) coated

glass slides (Bruker Daltonik). Subsequently, fullerite, $AgNO_3$ and DHB matrices and the derivatization agent Girard-T were applied to these slices by the Image Prep system.

Matrices had been selected according to the results from the pure-compound experiments. Fullerite (C_{60} and C_{70}) replaced graphite powder, which had been used for pure compounds, as it provided a much cleaner mass spectrum. Alternatively, with the purpose of minimizing matrix signals, use of colloidal graphite could also be explored (Warren et al., 2016). A diluted (6 µg mL^{-1}) and a concentrated (60 µg mL^{-1}) fullerite solution was prepared and sprayed for 20 cycles in the case of the diluted and for 10, 20 and 50 cycles in case of the concentrated one. For $AgNO_3$, DHB and Girard-T, four concentration levels (6, 60, 600 and 6000 µg mL^{-1}) were tested. Standard spray cycles consisted of 3 s of spraying and 30 s of drying time, but may be modified depending on the sprayed solvent and the time required for drying of deposited droplets.

The ~5 cm sediment section from the SBB was prepared in a similar fashion as the pellets of the sapropel test sample. The section was subsampled from a short LL-channel, frozen and freeze-dried, embedded and cut into 60 µm thick slices with the cryomicrotome. Each of these slices was immediately mounted on an ITO slide. For details on the preparation of this sample see Alfken et al. (2019). No artificial matrix was added.

III.2.3. Biomarker MSI – MALDI-FT-ICR-MS measurements

All analyses were carried out on a 7 T solariX XR FT-ICR-MS coupled to a DUAL source with a Smartbeam II laser (Bruker Daltonik). Data were acquired in a m/z range from 150 to 2000 with a data size of one megaword. For the ultra-high resolution molecular stratigraphy on SBB sediments, data were acquired with 95% reduction. External data calibration was performed weekly with a sodium trifluoroacetate (NaTFA) solution (Moini et al., 1998) followed by an internal lock mass calibration using the calculated m/z value of matrix peaks or known compounds as described in the results and discussion section. A list of suitable calibrants is given in Supplementary Table S2.

FT-ICR-MS settings for the m/z ranges of different target compounds were optimized by infusion and electrospray ionization of the tuning solution (NaTFA), lipid extracts and pure compounds, and confirmed by MALDI-FT-ICR-MS analyses of pure compounds. Special attention was paid to the ion transfer parameters time-of-flight, frequency and collision energy voltage, which were tuned for maximum signal intensity of the target compounds. CASI (continuous accumulation of selected ions) mode was chosen to enhance sensitivity in specific m/z ranges.

III.2.3.1. MSI of pure compounds

For the analysis of pure standards as dried droplets, three methods were established for the CASI ranges 300 ± 150, 600 ± 300 and 1200 ± 250. Data were acquired in triplicate, and in positive and negative ionization mode. Each measurement consisted of 48 scans. The scans were performed by randomly rastering the laser over the dried droplet, and the obtained data were directly averaged to one single mass spectrum. Each scan recorded the ions generated by 40 laser shots with 24% laser power. Laser size was set to medium, accounting for a diameter of ~60 µm. Identification of target compounds, including the different adducts, and quantification were carried out with Data Analysis 4.4 (Bruker Daltonik).

III.2.3.2. MSI of the lipid extract

For the MSI reproducibility test, the sapropel lipid extract, sprayed on aluminum plates, was measured in a 1320 ± 35 m/z range targeting isoprenoidal GDGTs in positive mode. The laser (500 shots at 40% laser power and a medium laser size) was set to raster across the sample plate in a regular pattern. In this manner, about 200 spectra were generated and recorded individually.

III.2.3.3. MSI of sediment samples

To assess the MSI-based detection of different biomarkers in a natural sediment sample, data were obtained from the sapropel test pellets for a regular laser pattern with 200 µm resolution. Laser settings were optimized for every target compound, matrix and sample, but generally accounted for 500 shots per spot, a large focus (~120 µm) and a laser power of 30 - 40%. MSI was performed over an area of ~10 - 20 mm^2 so that ~300 scans were recorded for each measurement. The effect of fullerite addition was evaluated in duplicate and in the three broad CASI ranges described above. Additional measurements were performed with narrower CASI windows, as will be described in the results and discussion section, to improve sensitivity for selected compounds. In the case of silver and DHB addition, and Girard-T derivatization, narrow CASI windows for the specific analysis of *n*-alkanes (Ag matrix), pheopigments (DHB matrix), sterols (Ag and DHB matrices) and long-chain alkenones (derivatization) were selected.

For the ultra-high resolution molecular stratigraphy on SBB sediments, dedicated measurements of targeted compounds were conducted on ~48 × 8 mm areas with CASI windows set at 450 ± 75 and 550 ± 30, resulting in more than 9000 spectra per area. For each CASI window, a dedicated slice was used.

All spatially resolved measurements were carried out using FlexImaging (Bruker Daltonik) and evaluated with Matlab 2015R (TheMathWorks) after exporting mass spectra in the region of interest from Data Analysis 4.4 (Bruker Daltonik). The export routine generates a comma separated file including spot position, m/z, intensity and signal to noise ratio (SNR) for every

measured position. The first step of the Matlab routine consisted of selecting the targeted m/z values. A suitable m/z window (0.005 units or less depending on the measurement quality) was identified for every single analysis by assessing mass accuracy in Data Analysis (mass position chromatogram of the selected target compound). When data had not been reduced during acquisition, a SNR threshold of 5 was applied. Proxy data were automatically calculated for each spot based on these filtered data.

III.2.3.4. Conventional biomarker analysis

An extract from the sapropel test sample was required to guide us in the identification of potential target compounds, to assess their abundance, and in order to perform the MSI reproducibility test with sprayed extract. The sample was sonicated and extracted into a mixture of methanol, dichloromethane (DCM) and aqueous buffer (2:1:0.8, v/v/v) following a modified Bligh and Dyer protocol (Sturt et al., 2004a; Wörmer et al., 2015). A monopotassium phosphate buffer (8.7 g l^{-1} KH_2PO_4, pH 7.4) was used for the first two steps and a trichloroacetic acid buffer (50 g l^{-1}, pH 2) for the final two steps.

After centrifugation, the supernatants were combined in a separatory funnel and DCM and water added in order to allow phase separation. After washing with MilliQ water, the lipid extract was dried under a gentle nitrogen flow and stored at -20 °C. The total lipid extract was analyzed by liquid chromatography coupled to mass spectrometry (LC–MS) (Wörmer et al., 2013; Becker et al., 2015) and, after derivatization, by gas chromatography coupled to mass spectrometry (GC–MS) (Schmidt et al., 2010; Elvert et al., 2016). Target compounds were quantified by comparison to added internal standards: C_{46} GTGT and squalane.

III.3. Results and Discussion

III.3.1. Laser-induced, matrix-assisted detection of pure compounds

Our tests revealed the need to carefully adjust sample preparation and analytical settings to the target compounds. Optimized methods, including measurement in the CASI mode, were sufficient to enable detection of all compounds at the tested concentration (Table 2). All compounds except fatty acids showed higher signal intensities in positive ionization method. This is in accordance with the known suitability of fatty acids for soft, negative-ion mass spectrometry (e.g. Kerwin et al., 1996).

Matrix application drastically improved detection of pure standards, with the exception of polyaromatic hydrocarbons (PAHs) in positive and fatty acids in negative mode, for which response was not further increased by matrix addition. In the case of PAHs, the molecules themselves are possibly acting as the laser-absorbing matrix (Hankin et al., 1996), which directly

results in the formation of radical ions. Matrix addition has been the key to the wide success of MALDI, as it enables the relatively soft desorption and ionization of non-volatile, fragile molecules.

Most biochemical applications use chemical matrices: small, typically aromatic, organic molecules, applied in excess over the analyte, to absorb the laser energy and drive co-desorption and ionization of the analyte (Hillenkamp et al., 2014). Among the tested compound classes, only the most polar one, the chlorophyll-related pheopigments, is ideally suited for analysis with these conventional MALDI matrices, and both DHB or HCCA led to very efficient protonation. This is in accordance with previous studies, which showed the benefits of terthiophene and 3-aminoquinoline to efficiently ionize intact chlorophylls without releasing the central metal ion (Suzuki et al 2009).

For all other less functionalized compound classes, application of graphite or silver offered best results. According to Hillenkamp et al. (2014), in so-called physical matrices (e.g. graphite-based) thermal desorption is the main process responsible for analyte ablation and ionization. The biomarkers typically employed in molecular stratigraphy possibly are stable enough to prevent the fragmentation potentially associated with these processes. Actually, it was only for some sterols that significant fragmentation, namely a loss of H_2O, was observed. This fragmentation, at least under the given analytical conditions, was most prominent without matrix addition or with conventional matrices, but weakest with silver addition.

The dominance of Na^+-adduct formation demonstrates the efficiency of cationization vs protonation and the importance of NaCl doping in order to prevent the target signal being distributed among several cation adducts. In the case of Ag application, ions in the expanding plume seem to be acting as a very efficient cationizing reagent for nonpolar or slightly polar lipids (Kahr and Wilkins, 1993), as evidenced in the preferential formation of Ag-adducts.

Table 2: *Detectability of molecular biomarker classes as pure standards by MALDI-FT-ICR-MS and main ionic species formed (in brackets). Spectrum quality is presented in semi-quantitative categories based on the signal to noise ratio (SNR) data from several compounds (cf. Table S1) in the same class (traces: 0 < SNR < 50, +: 50 < SNR < 250, ++: 250 < SNR < 1000, +++: SNR > 1000).*

	No matrix	**Conventional**		**Unconventional**		**Other**
		DHB	**HCCA**	**graphite**	**$AgNO_3$**	
n-Alkanes	Traces ($M+Na^+$)	Traces ($M+Na^+$)	-	Traces ($M+Na^+$)	+++ ($M+Ag^+$)	-
n-Alcohols	Traces ($M+Na^+$)	+ ($M+Na^+$)	-	++ ($M+Na^+$)	+++ ($M+Ag^+$)	-
PAHs	+++ (M^+)	-	-	+++ (M^+)	+++ (M^+, $M+Ag^+$)	-
Sterols	++ ($M+Na^+$)	++ ($M+Na^+$)	++ ($M+Na^+$)	++ ($M+Na^+$)	+++ ($M+Ag^+$)	-
C_{37} Alkenones	++ ($M+Na^+$,$+K^+$)	Traces ($M+Na^+$)	-	+++ ($M+Na^+$)	+ ($M+Ag^+$)	++ Derivati-zation*
Isoprenoidal GDGTs	Traces ($M+Na^+$)	-	-	++ ($M+Na^+$)	Traces ($M+Na^+$, Ag^+)	-
BHPs	++ ($M+Na^+$)	++ ($M+Na^+$)	+ ($M+Na^+$)	+++ ($M+Na^+$)	+++ ($M+Na^+$, Ag^+)	-
Fatty acids	++ ($M+Na^+$)	++ ($M+Na^+$)	Traces ($M+Na^+$)	++ ($M+Na^+$)	+++ ($M+Ag^+$)	+++ ($M-H^-$)
Carotenoids	-	++ ($M+Na^+$)	++ (M^+, $M+Na^+$)	+++ ($M+Na^+$)	+ ($M+Ag^+$)	
Pheopigments	+ (M^+)	+++ ($M+H^+$)	+++ ($M+H^+$)	++ ($M+Na^+$)	+ (M^+)	

*Derivatization with Girard-T.

The ionization efficiency of some compound classes may be especially noteworthy: *n*-alkanes are not detected, except when silver is added (Fig. 2). This is consistent with Ag-enabled analysis of these compounds in plant material (Cha et al., 2009; Jun et al., 2010) and oil (Dutta and Harayama, 2001) and defines the conditions under which MSI of sedimentary n-alkanes could be feasible. In the case of archaeal isoprenoidal GDGTs, detection is only possible in the presence of graphite. Interestingly, GDGTs were analyzed in our first approach to MSI of sediments without artificial matrix addition (Wörmer et al., 2014). At that time, considering that neither DHB or HCCA improved detection of these compounds, we hypothesized that marine sediments already contain abundant compounds that may act as natural, ionization-facilitating matrix, as well as NaCl that might support cationization. The present data suggest that the organic-rich sapropel layer analyzed may have been acting analogously to graphite.

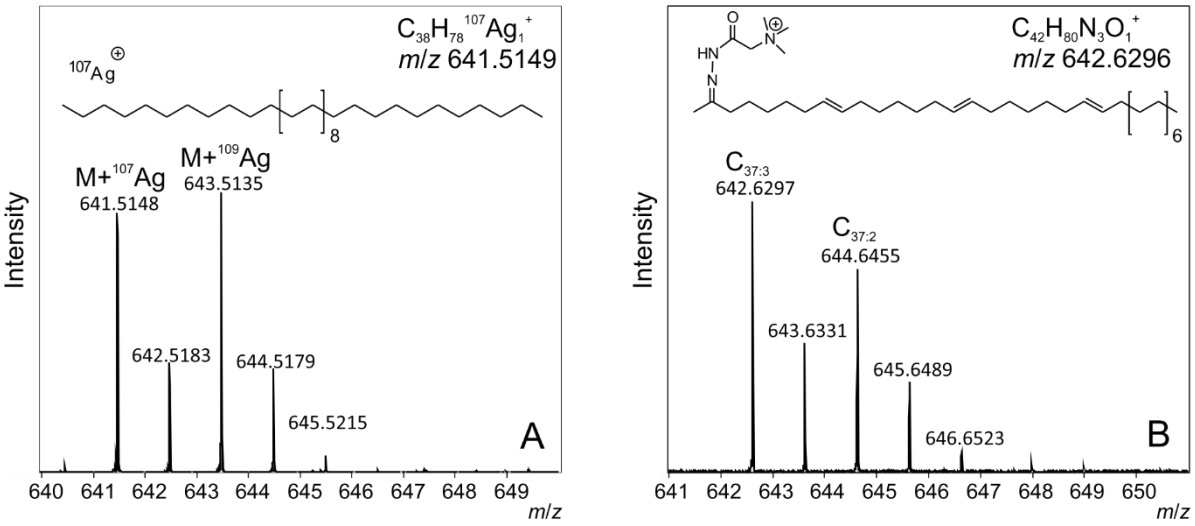

Fig. 2: *Mass spectra of standards obtained by MALDI-FT-ICR-MS for: (A) Ag adducts of the C_{38} n-alkane, and (B) C_{37} alkenones derivatized with Girard T.*

Another compound class used as an SST proxy, the long-chain alkenones, is also best detected in the presence of graphite. Even though it is not as efficient as graphite, derivatization with Girard T can also be a viable option for the analysis of these compounds. The derivatization reagent is specifically targeting the keto-group and results in a permanent positive charge (Fig. 2). In the present study the positive effect was not as dramatic as observed, for example, by Kim et al. (2015) for the derivatization of homoserine lactones. However, the specificity of the performed reaction may be of interest in complex samples in order to maximize ion yield, provided in situ derivatization can be efficiently implemented on the sample. This was unfortunately not the case, as will be shown below, in the organic-rich sediment tested.

III.3.2. Optimizing laser-induced detection of molecular biomarkers in sedimentary systems

Based on the results shown above, we selected four treatments to be implemented on sediment samples: fullerite, Ag and DHB addition and in situ derivatization with Girard T. Fullerite was considered the most versatile of the matrices tested, providing excellent results for standards of all compound classes except *n*-alkanes. Therefore, analyses were carried out in three broad CASI windows that covered a wide m/z range and were suitable for non-targeted identification of relevant compounds. Interestingly, for fullerite-amenable compounds, as hypothesized in Wörmer et al. (2014), the sapropelic sediment matrix already seems to be offering a chemical environment suitable for proper ionization. Consequently, signal intensity only slightly improved by fullerite addition and actually got quickly suppressed when increasing the amount of matrix (Fig. 3). However, we cannot rule out that addition of fullerite may be more beneficial in other systems, for example, in organic lean sediments. Even in the present case, matrix addition offers some additional benefits: ionization conditions are expected to be more homogeneous and an optimal way for mass calibration is provided. Fullerite is detected as two dominant peaks (m/z 719.9994 for C_{60} and 839.9994 for C_{70}), which can be used when working in the corresponding m/z range, while double charged molecular ions (m/z 359.9994 and 419.9994) may be suitable for smaller molecules.

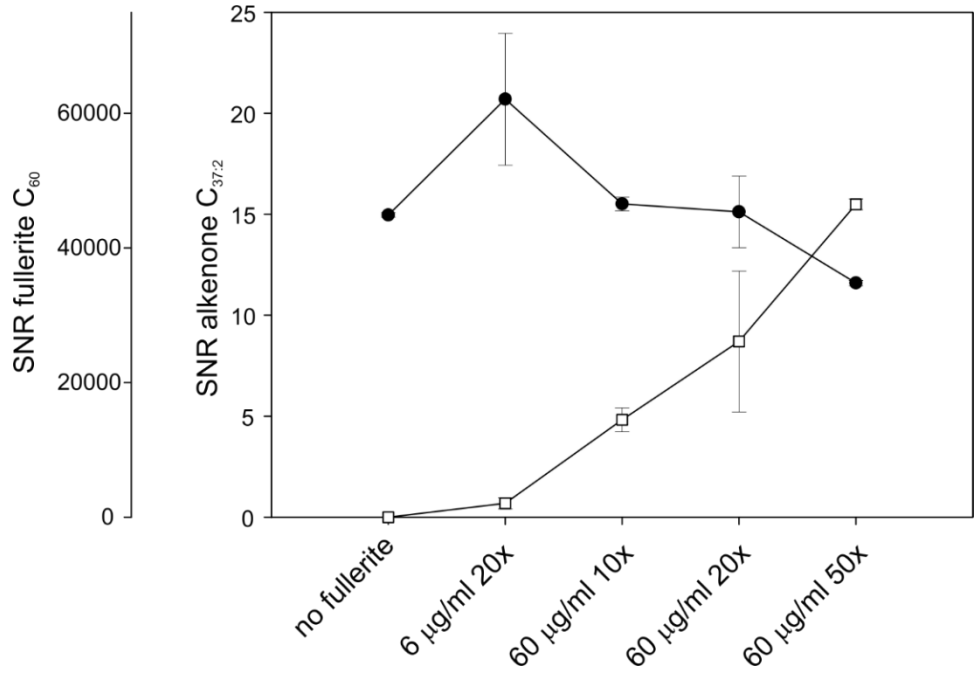

Fig. 3: *Signal to noise ratio (SNR) of matrix peaks (C_{60} fullerite, white squares) and the C37:2 alkenone biomarker (black dots) in 60 µm thin slices of the sapropel test sample (GeoB15103) to which increasing amounts of fullerite were applied. Each datapoint represents average and standard deviation values of two measurements; each measurement consists of 300 - 400 individual mass spectra obtained with 200 µm resolution.*

A wide range of compounds could be unambiguously identified after applying the diluted fullerite solution (6 µg mL^{-1}, 20 cycles), including long-chain alkenones, isoprenoidal GDGTs, long-chain diols and fatty acids. However, when targeting some of the less abundant compounds, it became obvious that the broad CASI windows employed for pure compounds were no longer suitable. Target compounds are easily suppressed by other more abundant signals, being present in the sample and ionized in MALDI-FT-ICR-MS. This phenomenon could be compensated by choosing narrower CASI windows (<100), which increased the percentage of successful spectra by up to a factor of four and consistently doubled the SNR of successfully detected compounds (Fig. 4). We therefore recommend to establish dedicated methods for each compound class, with MS parameters optimized for the respective molecular size, and a CASI window as narrow as possible to fit the relevant compounds with their corresponding adducts. This approach was chosen for all analyses described below.

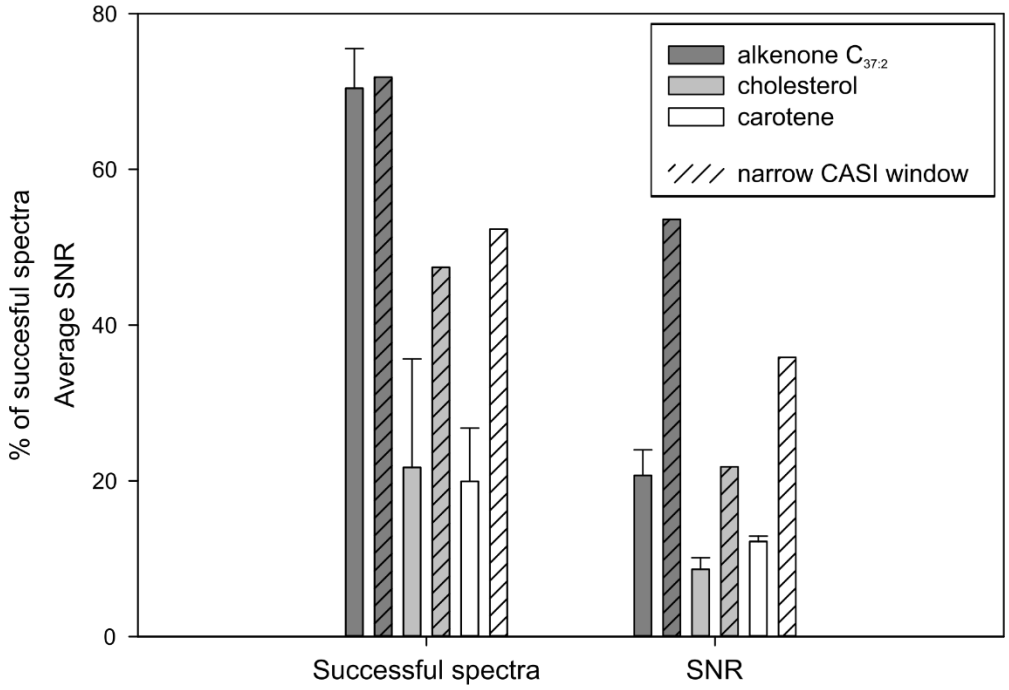

Fig. 4: *Percentage of successful spectra, defined as the fraction of measured spots at which the target compounds could be detected with a signal to noise ratio (SNR) higher than 5, and average SNR in these successful measurements. Shown data are for MSI of selected biomarkers ($C_{37:2}$ alkenone, cholesterol and carotene) in 60 µm thin slices of the test sediment (pooled sapropel layers, GeoB15103) with broad (300, no pattern, duplicate measurements) and narrow (<100, dashed patterns, single measurements) CASI windows respectively.*

Although MSI was already successful without matrix addition or in presence of fullerite, signal intensity of pheopigments (e.g. pyropheophorbide *a*) was slightly improved by addition of DHB, as could be expected based on the results from the pure compound experiments. In comparison to fullerite, larger amounts of DHB seem necessary. We recommend a concentration

of 6 mg mL^{-1}, applied for 50 cycles. Interestingly, in these analyses the Na^+-adduct was dominant, while protonation had been most abundant when working with pure compounds, which is possibly explained by a massive presence of Na-containing salts in marine sediments.

The use of an Ag matrix to facilitate ionization of *n*-alkanes in marine sediment turned out to be more difficult than in our experiments with pure compounds or previous studies of crude oil (Dutta and Harayama, 2001). Even though matrix concentrations over four orders of magnitude were tested, *n*-alkanes were only detected sporadically in our test sample. Despite intense matrix peaks (Ag^{3+} and Ag^{5+}) confirming presence and ionization of Ag molecules, Ag-mediated ionization of *n*-alkanes seems to be outcompeted by other processes with a higher ion yield. For studies of distributions of wax compounds from higher land plants in sediments, it may thus be more effective to track the more easily detectable *n*-alcohols instead of *n*-alkanes.

In situ derivatization with Girard-T was tested for detection of long-chain alkenones, given the specificity of this reaction for ketones. The conventional matrix application procedure, i.e., nebulization and deposition of fine droplets followed by rapid drying, was not successful, as alkenones continued to be detected in their underivatized form. Only when "flooding" the sample by increasing the time of spraying and preventing proper sample drying between cycles, were intense signals of alkenone derivatives detected. However, such flooding led to a massive delocalization of analytes, which were also detected outside of the sediment slice. Derivatization thus seems to require analyte extraction and a liquid phase, a procedure not feasible on intact sediment surfaces without compromising the fine-scale spatial distribution of analytes.

Our data thus suggest that MSI analysis of biomarkers in sediment samples will only moderately benefit from matrix application. At least in the organic-rich marine samples tested here, measurement without addition of artificial matrix is a viable option, as is the addition of low quantities of fullerite. DHB or similar conventional matrices may be useful when targeting specific, rather polar compounds such as pheopigments, as might be doping with Na^+-sources in freshwater sediments. Proper sample preparation (Alfken et al., 2019) and use of specific MS methods and narrow CASI ranges for individual compound classes on the other side are mandatory for successful MSI.

The analysis of the test sample provides an initial overview of the portfolio of biomarkers amenable to MSI and ultra-high resolution molecular stratigraphy in eastern Mediterranean sapropels (Fig. 5). It has to be noted that, as no chromatographic separation is employed in MSI, compound identification relies exclusively on highly accurate molecular mass determination. Isomers (i.e., compounds with the same molecular formula but different structure) can thus not be separated from each other. Conventional analysis, and if possible MSI-derived MS^2 scans,

should be employed to validate the assignment of molecular formulas to specific compounds. Unspecific formulas should be avoided for interpretation of sediment-derived MSI. The compounds shown in Fig. 5 and Supplementary Table S2 reflect only a minor fraction of the hundreds of peaks in each CASI window, many of which remain unidentified, and of the many more compounds expected in other sediments and m/z windows. However, even this initial assessment reveals a suite of compounds that may be useful to track changes in past climate and corresponding ecosystem response on a previously unattainable scale.

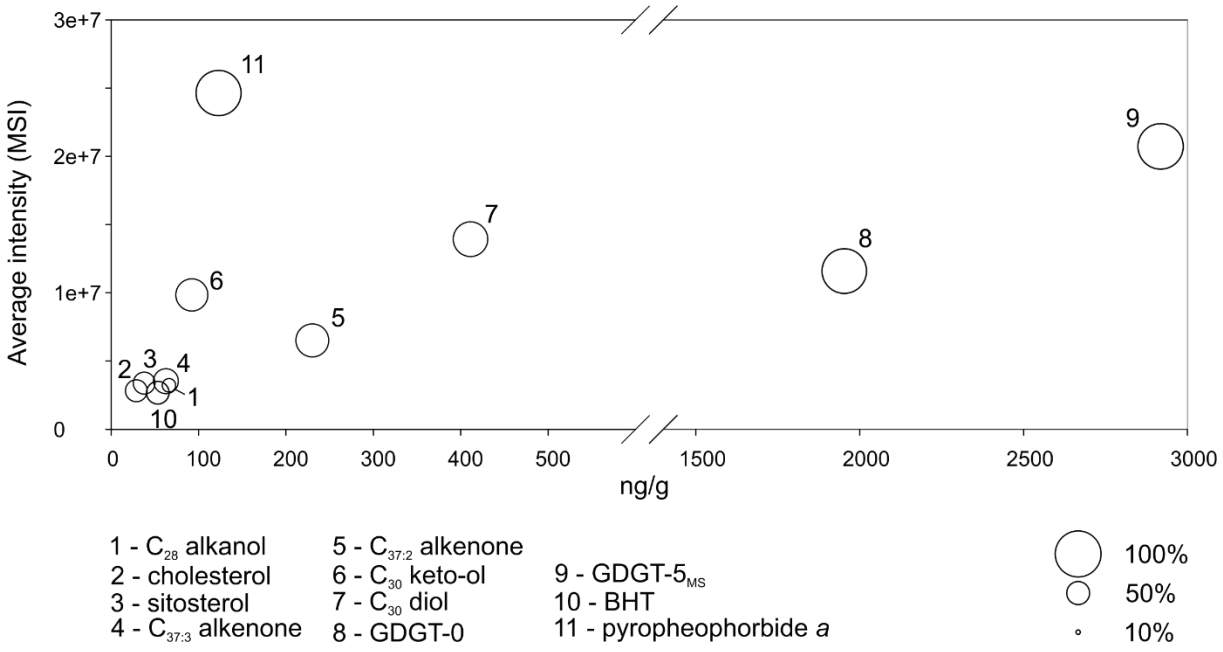

Fig. 5: *Selection of MSI-amenable molecular biomarkers with proxy potential, their average intensity (~400 single spectra) and concentration obtained by conventional GC-MS or HPLC-MS methods. Circle size indicates % of spectra in which the target compounds could be successfully detected. While we consider that this percentage is mostly indicative of compound concentration and ionization efficiency, it may also reflect heterogeneity of analyte distribution. GDGT-5_{MS} stands for the sum of isoprenoidal GDGTs with 5 double bond equivalents, including the major compound crenarchaeol and its isomers.*

Average intensity for most of the compounds is in accordance with concentration determined by GC-MS or HPLC-MS analysis after extraction. Only the relatively polar pyropheophorbide *a* shows a drastically increased relative intensity, evidencing the preferential ionization of the highly functionalized pheopigments compared to other target molecules (Fig. 5). A more complete list of detected compounds, including some prominent matrix or contamination peaks (e.g. plasticizers) that may be used as calibrants is provided as Supplementary Table S2.

III.3.3. Application of MSI for molecular proxy research

In dated, non-bioturbated sediments, high spatial resolution patterns of biomarker abundance and corresponding proxy values are potentially highly informative regarding the environmental conditions during sediment deposition. In conventional molecular stratigraphy, the examination of extracts from sediment samples on GC- or LC-based systems provide information on a large number of analytes that are present at the ng scale at the expense of sacrificing detailed temporal and spatial information. With MSI, by contrast, the amount of analyte per analysis is extremely small: with ~120 µm laser spot diameter, and assuming ~1 µm penetration depth and 1.3 g per cm^3 sediment density, and a verified concentration of 2.9 µg crenarchaeol per g in our test sample, each spot would yield an amount of only ~43 fg crenarchaeol. Therefore, we aimed to identify how many measurement spots need to be combined from coeval horizons in order to obtain satisfactory precision (cf. Wörmer et al., 2014).

To define a threshold for the number of required measurement spots, we quantified isoprenoidal GDGTs and calculated the crenarchaeol caldarchaeol tetraether index (CCaT; Wörmer et al., 2014) for the sapropel lipid extract sprayed on an aluminum sample holder. The standard deviation in CCaT determination as a function of the number of mass spectra (equivalent to coeval measurement spots) and analyte concentration served as an indicator of precision (Fig. 6). The higher the concentration, the sooner high reproducibility was achieved. In the concentration range >~1 µg crenarchaeol per g sediment, 10 spots resulted in a standard deviation of 0.01 CCaT units or less, and thus in an analytical precision for SST determination of ~0.6 °C or better; at this concentration range, more than 20 spots resulted in an analytical precision of ~0.3 °C. We have encountered concentration levels of >1 µg major GDGT per g sediment in the Mediterranean sapropels investigated, but also in some of the sedimentary systems that we view as most suitable for MSI-based molecular stratigraphy, i.e. laminated sediments from the SBB and the Cariaco Basin. For the sake of analytical quality in molecular stratigraphic studies, we therefore recommend to exclude data points generated from fewer measurement spots.

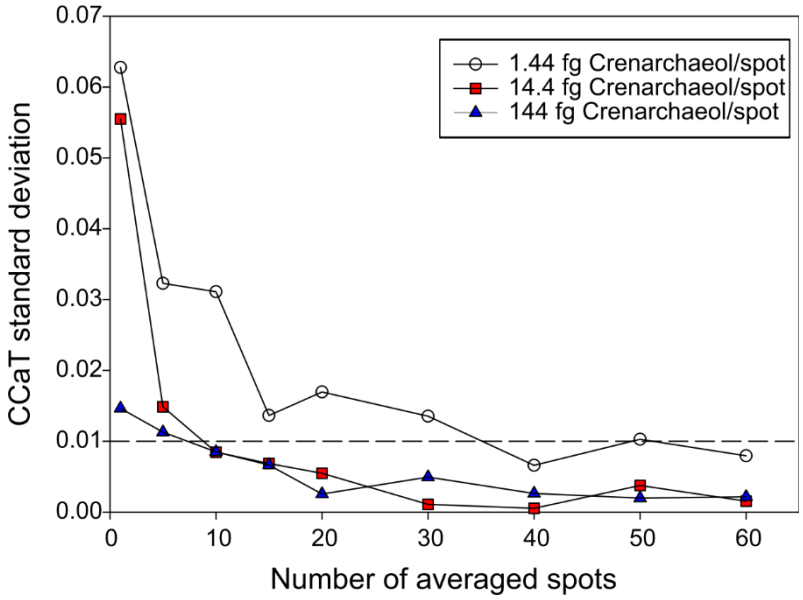

Fig. 6: *Assessment of the number of mass spectra (equivalent to number of measurement spots) required for statistically robust CCaT determination. Increasing amounts of a lipid extract from the sapropel test sample containing isoprenoidal GDGTs were sprayed on aluminum plates and ~200 spectra recorded by MSI. Standard deviation of the CCaT value for three replicates is plotted against the number of randomly chosen measurement spots for each replicate.*

As in conventional molecular stratigraphy, a multiproxy approach is most promising for a proper evaluation of paleoenvironmental variability. With the tools now at hand, ultra-high resolution records for an SST proxy ($U^{K'}_{37}$, Brassell et al., 1986, Prahl and Wakeham, 1987) and the C_{29} stanol/stenol ratio as indicator for redox conditions (Wakeham, 1989) were obtained for the uppermost ~5 cm section from the SBB sediment slab (Fig. 7), and can be compared to the CCaT record from the same sample (Alfken et al., 2019). As described in Alfken et al. (2019), layers are not horizontal, but slightly tilted, potentially because of original coring and core subsampling. By applying a shifting vector derived from the tilting observed by visual inspection, X-ray images and element distribution, these inclined layers are transformed into horizons ideally perpendicular to the depth axis (cf. Alfken et al., 2019). After this horizontal transformation, data from individual layers for which at least 10 individual data points were available were averaged to a single value (Fig. 7C).

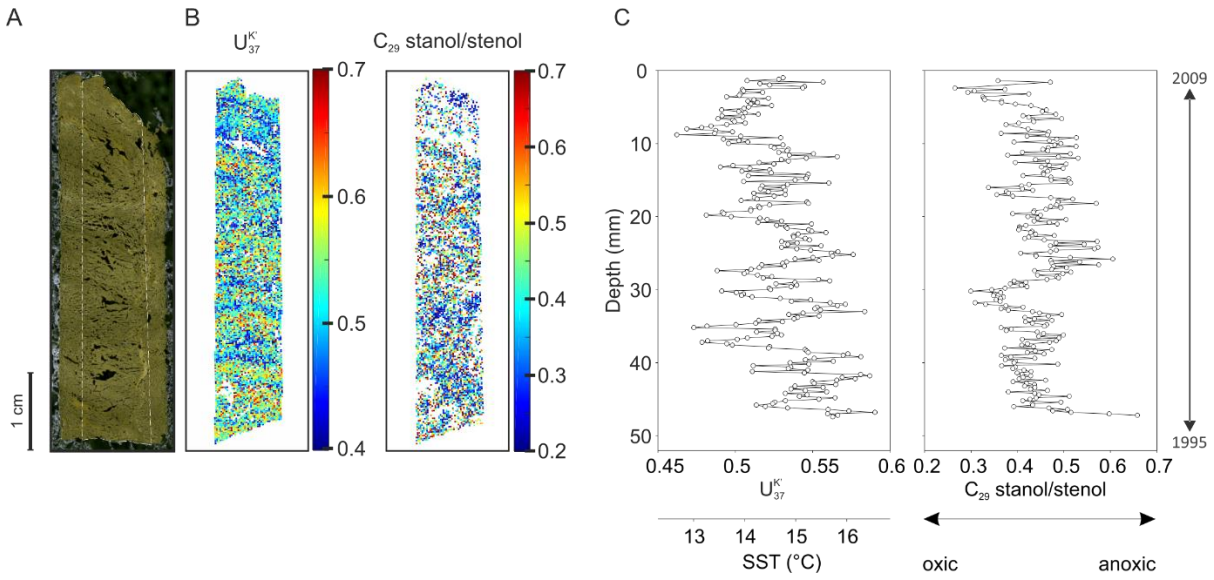

Fig. 7: *Ultra-high resolution multiproxy record for the uppermost ~5 cm sediment in the Santa Barbara Basin (core SPR0901-05BC). (A) Image of analyzed sample slice; (B) horizontally corrected distribution of $U^{K'}_{37}$ values and the C_{29} stanol/stenol ratio; (C) downcore profile for the two proxies obtained by averaging single horizontal layers. The analyzed section accounts for ~14 years of sedimentation (Alfken et al., 2019).*

$U^{K'}_{37}$ estimates fall in the range of SSTs recorded in the SBB. Additionally, the downcore profile of these SST estimates is consistent with yearly SST cycles regarding both its frequency and amplitude. Especially below the somewhat disturbed upper 10 mm, the record strongly suggests that with the 200 µm resolution we were able to resolve yearly SST cycles. The corresponding CCaT profile (Alfken et al., 2019) on the other hand does not reflect these yearly cycles, but lower frequency variations. These broader and more pronounced minima and maxima are potentially linked to El Niño-Southern Oscillation (ENSO) variability, and demonstrate that both proxies provide complementary information.

Interestingly, the stanol/stenol ratio of C_{29} sterols shows a profile more related to the one for CCaT (Alfken et al., 2019) and thereby suggests a coupling between these proxies at this location. CCaT maxima are accompanied by minima in the stanol/stenol ratio, suggestive of higher oxygen concentrations. Wang et al. (2017) analyzed instrumental data from the SBB and identified a tight linkage between ENSO variability and water oxygen replenishment. Our multiproxy approach confirms that this potential interdependence is recorded in, and can be retrieved from, the sedimentary archive at an interannual scale. Possible reasons for this coupling may, for example, be found in flushing with cold oxygenated water as suggested by Wang et al. (2017), or

in the upwelling-induced high primary productivity and associated increased organic matter remineralization and oxygen consumption during La Niña events.

A detailed discussion of ultra-high resolution climate and environmental observations is beyond the scope of this study. However, our preliminary data confirm the potential to reconstruct SST variations on a sub-annual scale and to characterize concurrent physical and ecological changes in the water column. Validating observed trends with instrumental data and extending the record throughout the laminated interval will nicely complement the high-resolution inorganic data previously obtained from this location by Hendy et al. (2015).

III.4. Conclusions

MSI is firmly established in the life sciences but has only recently been introduced in the geosciences. The main challenges regarding its application to sediments include significantly lower analyte concentration than in tissue samples, potential inhibitory effects of the mineral matrix and the generally lower polarity range of biomarkers, which may reduce ionization efficiency. Based on successful ionization of GDGTs (Wörmer et al., 2014, Alfken et al., 2019), we have sought to extend the range of sedimentary biomarkers amenable to MSI. We assembled an initial inventory of informative biomarkers that are readily detected in tested sediments; these include pigments, long-chain diols and alkenones, sterols and BHPs, in approximate order of signal quality. Unlike studies of biological tissue, the ionization of the majority of these compounds does not benefit from the use of conventional matrices; instead atypical matrices based on carbon or silver aid their ionization. We also observed that sediments serve as a natural matrix, directly allowing detection of many of these compounds. However, the sediment matrix also inhibits some reactions that otherwise promote detection, such as in situ derivatization of alkenones or silver-mediated ionization of *n*-alkanes. We further demonstrate that: (a) narrow m/z measurement ranges are required for the proper detection of analytes in relatively low concentration, and (b) summation of information from several coeval measurement spots yields precise proxy values.

With the method development described in the present study, including the selection of suitable matrices, the definition of optimal MS methods and the identification of potential target compounds, we have enabled ultra-high resolution, multi-proxy molecular stratigraphy via MSI. Such multi-proxy records, obtained from suitable marine or lacustrine sediment archives, will provide relevant and previously inaccessible information of climate and ecological change.

Acknowledgments

This study was funded by the ERC under the European Union's Horizon 2020 research and innovation programme (grant agreement No. 670115 ZOOMECULAR; PI K.-U.H.). We thank Arndt Schimmelmann (Indiana University) for providing the Santa Barbara Basin sample. We are grateful to the University of Bremen for setting up the infrastructure required for housing the Geobiomolecular Imaging Lab. Finally, our thanks to the editors and reviewers for their helpful comments.

III.5. Supporting information

Table S1: *Overview of pure standards tested for MALDI-FT-ICR-MS*

Compound	Obtained from:
***n*-Alkanes**	
$C_{36, 38, 39, 40}$	Sigma Aldrich, Dr. Ehrenstorfer GmbH
Polycyclic aromatic hydrocarbons (PAHs)	
Acenaphtylene, fluorene, phenanthrene, anthracene, pyrene, benzo(a)anthracene, chrysene, benzo(b)fluranthene, benzo(k)fluorantene, benz(a)pyrene, dibenz (a,h) anthracene, benzo(g,h,i)perylene, indeno (1.2.3, cd)pyrene	Sigma-Aldrich
Ketones	
2-Nonadecanone, 4-cholesten-3-one, epiandrosterone	Sigma-Aldrich, Fluka
Esters	
Nonadecanoic acid methyl ester, behenic acid methyl ester	Sigma-Aldrich, Fluka
Sterols	
Cholesterol, dihydrocholesterol, ergosterol, stigmasterol	Sigma-Aldrich
Bacteriohopanepolyols (BHPs) and hopanols	
Bacteriohopanetetrol (BHT), 2-methyl bacteriohopanetetrol, 2-methyl diplopterol	Dr. Roger Summons (MIT)
Long-chain alkenones	
$C_{37:2, 37:3}$	Dr. Ian Bull (University of Bristol)
***n*-Alcohols**	
Nonadecanol	Sigma-Aldrich
Isoprenoidal tetraether lipids	
Caldarchaeol (GDGT-0)	Dr. Julius Lipp (MARUM, University of Bremen)
Fatty acids	
Myristic acid, palmitoleic acid, palmitic acid, petroselenic acid, stearic acid, 2- methyloctadecanoic acid, nonadecanoic acid, arachidic acid, behenic acid	Sigma-Aldrich, Fluka
Pheopigments	
Pheophorbide *a*	Sigma-Aldrich
Carotenoids	
β Carotene, astaxanthin	Cayman Chemical

Table S2: *Selection of molecular formula and potential corresponding compounds identified by MSI in pellets made of pooled eastern Mediterranean sapropel layers (GeoB15103). The selection of compounds aims at providing an overview of prominent detectable compound classes rather than a detailed inventory.*

Compound	**Molecular formula**	***m/z* (adduct)**	**Observation**
Alkenone $C_{37:2}$	$C_{37}H_{70}O_1$	553.5319 (Na)	
Alkenone $C_{37:3}$	$C_{37}H_{68}O_1$	551.5162 (Na)	
Alkenone $C_{38:2}$	$C_{38}H_{72}O_1$	567.5475 (Na)	
Carotene	$C_{40}H_{56}$	559.4274 (Na)	
Echinenone	$C_{40}H_{54}O_1$	573.4067 (Na)	
Canthaxanthin	$C_{40}H_{52}O_2$	587.3860 (Na)	
Diatoxanthin	$C_{40}H_{54}O_2$	589.4016 (Na)	
Lutein, zeaxanthin	$C_{40}H_{56}O_2$	591.4173 (Na)	
Diploptene, squalene …	$C_{30}H_{50}$	433.3805 (Na)	Unspecific, use as calibrant
Bacteriohopanetetrol (BHT)	$C_{35}H_{62}O_4$	569.4540 (Na)	
AnhydroBHT	$C_{35}H_{60}O_3$	551.4435 (Na)	
Bishomohopanoic acid	$C_{32}H_{54}O_2$	493.4016 (Na)	
Cholesterol	$C_{27}H_{46}O_1$	409.3441 (Na)	
Cholestanol	$C_{27}H_{48}O_1$	411.3597 (Na)	
Brassicasterol	$C_{28}H_{46}O_1$	421.3441 (Na)	
Stigmasterol	$C_{29}H_{48}O_1$	435.3597 (Na)	
Sitosterol	$C_{29}H_{50}O_1$	437.3754 (Na)	
Stigmastanol	$C_{29}H_{52}O_1$	439.3910 (Na)	
Dinosterol	$C_{30}H_{52}O_1$	451.3910 (Na)	
GDGT-0, Caldarchaeol (0 dbe)	$C_{86}H_{172}O_6$	1324.3046 (Na)	
GDGT-5, Crenarchaeol (5dbe)	$C_{86}H_{162}O_6$	1314.2264 (Na)	Use as calibrant
Long chain keto-ol C_{30}	$C_{30}H_{60}O_2$	475.4486 (Na)	
Long chain diol C_{30}	$C_{30}H_{62}O_2$	477.4642 (Na)	Use as calibrant

Table S2 continued: *Selection of molecular formula and potential corresponding compounds identified by MSI in pellets made of pooled eastern Mediterranean sapropel layers (GeoB15103). The selection of compounds aims at providing an overview of prominent detectable compound classes rather than a detailed inventory.*

Compound	**Molecular formula**	***m/z* (adduct)**	**Observation**
Long chain keto-ol C_{32}	$C_{32}H_{64}O_2$	503.4799 (Na)	
Long chain diol C_{32}	$C_{32}H_{66}O_2$	505.4955 (Na)	
n-Alcohol C_{28}	$C_{28}H_{58}O_1$	433.4380 (Na)	
Tocopherol	$C_{29}H_{50}O_2$	453.3703 (Na)	
Pyropheophorbide *a*	$C_{33}H_{34}N_4O_3$	557.2523 (Na)	Use as calibrant
Chlorophyllone *a*	$C_{33}H_{32}N_4O_3$	555.2367 (Na)	
Diisonyl phtalate	$C_{26}H_{42}O_4$	441.2975 (Na)	Possible contamination, use as calibrant

CHAPTER IV

NEW INSIGHTS INTO THE FACTORS SHAPING MOLECULAR PROXIES VIA SEASONALLY RESOLVED SEDIMENTARY RECORDS

Susanne Alfken[a], Lars Wörmer[a], Julius S. Lipp[a], Jenny Wendt, Arndt Schimmelmann[b], Kai-Uwe Hinrichs[a*]

submitted to a
peer-reviewed international journal

[a] Organic Geochemistry Group, MARUM – Center for Marine Environmental Sciences and Faculty of Geosciences, University of Bremen, Leobener Str. 8, 28359 Bremen, Germany

[b] Department of Earth and Atmospheric Sciences, Indiana University, 1001 E 10th Street, Bloomington, IN 47405-1405, USA

* Corresponding author: E-mail address: khinrichs@uni-bremen.de

Abstract

Lipid biomarkers archived in marine sediments include widely applied proxies to reconstruct sea surface temperature (SST). Two prominent groups of SST sensitive biomarkers are long-chain alkenones from haptophyte algae and glycerol dibiphytanyl glycerol tetraethers (GDGTs) from planktonic Thaumarchaeota. The corresponding proxies, $U^{K'}_{37}$ and TEX_{86}, respectively, are strongly correlated with mean annual SST. However, studies of cultures suggest that other factors such as nutrients could also influence the proxy signals. We created monthly-resolved records of molecular SST proxies *via* mass spectrometry imaging at 200-µm resolution in varved sediments from Santa Barbara Basin to gain new mechanistic insights into proxy signal formation. Direct comparison of biomarker data in sediments deposited between 1984 and 2009 to water column data determined at seasonal resolution during the same period shows that $U^{K'}_{37}$ responds sensitively to SST variations, while also being influenced by seasonal variations in nutrient concentrations. Surface water nitrate concentrations above or below ~2 µmol/L are associated with $U^{K'}_{37}$ values that over- or underestimate the actual SST, respectively. Distributions of GDGTs, expressed as CCaT and TEX^{L}_{86} ratios, are correlated with chemical properties in the subsurface water column, which are controlled by interannual variations in upwelling intensity linked to dynamics of the California Current system. This relationship is attributed to the impact of nutrients on thaumarchaeal growth rates and GDGT cyclization. The coupling of CCaT to SST was weak but enhanced for temperatures averaged across the upper 100 m of the water column.

Significance Statement:

Lipid biomarkers from marine haptophytes and planktonic archaea deposited in sediments are widely used for reconstructing past sea surface temperatures. Conventional analyses of such biomarkers use samples that average signals of several years to decades. In varved sediments from Santa Barbara Basin off California deposited between 1984 and 2009, we measured these biomarkers at monthly to quarterly resolution by mass spectrometry imaging. Relating the data to coeval water column measurements of temperature and dissolved chemical species shows that nutrient availability influences the ability of both sets of biomarkers to record temperature. Interestingly, biomarkers of shallow-dwelling haptophytes respond to annual cyclicity of both temperature and nutrients while biomarkers from deep-dwelling planktonic archaea especially respond to longer-term variations in upwelling intensity.

IV.1. Introduction

Lipid biomarkers are valuable tools for extracting paleoenvironmental information from sedimentary archives. Originating from lipid membranes of microorganisms that once inhabited the water column, they provide information on environmental properties such as temperature within their biological producers' habitats. A prominent example are long-chain alkenones from marine haptophytes (Brassell et al., 1986); the degree of unsaturation of these compounds is dependent on the ambient temperature encountered in the algal habitat (Prahl et al., 1988) and the signal is faithfully recorded in marine sediments (Müller et al., 1998). Long-chain alkenones are consequently used to reconstruct sea surface temperatures (SST) using the $U^{K'}_{37}$ proxy (e.g., Kennedy and Brassell, 1992; Castañeda et al., 2010; Naafs et al., 2010). Another group of SST proxies is based on the relative distribution of the isoprenoidal glycerol dibiphytanyl glycerol tetraethers (GDGTs) from marine Thaumarchaeota (Schouten et al., 2002). This group of SST proxies includes the widely applied TEX_{86} (Schouten et al., 2002) and its derivative TEX^{L}_{86} (Kim et al., 2010), and the CCaT, a proxy based on the ratio of the two major GDGTs (Wörmer et al., 2014). GDGTs are ubiquitous in marine sediments and can be found in ancient sediments back to the mid-Cretaceous (Kuypers et al., 2001). Marine Thaumarchaeota increase cyclization in their GDGT membrane lipids to adapt to higher growth temperature (Wuchter et al., 2004).

Evidence exists that factors other than temperature may additionally influence the signals recorded by the aforementioned SST proxies. For example, ecological factors (Conte et al., 1998) and physiological responses to nutrient (Conte et al., 1998; Epstein et al., 1998; Prahl et al., 2003) and light stress (Conte et al., 1998; Prahl et al., 2003) have been suggested to also influence alkenone content and composition. Likewise, the sole dependency of GDGT cyclization on temperature has been challenged by culture experiments, which showed that the degree of cyclization is influenced by growth stage (Elling et al., 2014), oxygen concentration (Qin et al., 2015), taxonomic affiliation of the GDGT-producing Thaumarchaeon (Elling et al., 2015), and nutrient availability (Hurley et al., 2016; Evans et al., 2018). These findings can partly explain mismatches of reconstructed TEX_{86} SSTs with *in situ* temperatures in suspended particulate matter (e.g., Basse et al., 2014; Mollenhauer et al., 2015; Zhu et al., 2016; Hurley et al., 2018).

Proxy-based reconstructions of climatic and oceanographic properties at high temporal resolution are limited by the minimum sample amount required to produce high-quality data. In the late Quaternary, depending on sedimentation rate, this typically results in signal averaging to an annual-to-decadal mean. Even in high sedimentation rate settings, this averaging leads, for example, to an underrepresentation of strong El Niño events (Kennedy and Brassell, 1992; Herbert et al., 1998). Additionally, it cannot be determined whether a proxy signal in the sediment is seasonally biased or mirrors the yearly cycle.

Varved sediments of the Santa Barbara Basin (SBB), located offshore of Southern California, provide a unique record for high-resolution climate reconstruction (reviewed in refs. Schimmelmann and Lange, 1996; Schimmelmann et al., 2016). The suboxic conditions in the bottom waters, in combination with a seasonally alternating, high sedimentation rate favor the preservation of laminated sediments (Emery and Hülsemann, 1961; Soutar and Crill, 1977; Thunell et al., 1995). The seasonal upwelling intensity along the California Margin is influenced by interannual and decadal-scale variability related to El Niño-Southern Oscillation (ENSO), Pacific Decadal Oscillation (PDO, Mantua and Hare, 2002) and North Pacific Gyre Oscillation (NPGO, Di Lorenzo et al., 2008). Upwelling intensity decreases during the positive (warm) PDO phases and El Niño events, whereas an increase in upwelling intensity and primary productivity between 38°N and 30°N is associated with the NPGO (Di Lorenzo et al., 2008).

Kennedy and Brassell (1992) showed that long-chain alkenones from haptophyte algae extracted from SBB sediment could be used to reveal annual oscillations in sea surface temperature (SST) and warming associated with 20th century El Niño events. This study has remained one of the most highly-resolved biomarker records. With respect to the utility of archaeal GDGTs, Huguet et al. (2007) found that TEX_{86} based temperatures reconstructed in sediments and particulate organic matter from the SBB were substantially lower than actual SST in surface waters. They attributed this observation to the subsurface habitat of the proxy-signal producing Thaumarchaeota. Indeed, highest abundances of archaeal rRNA in the SBB have been detected in subsurface depth intervals (Massana et al., 1997) coinciding with the nitrite maximum (Murray et al., 1999).

Recently, we introduced an extraction-free, mass spectrometry imaging (MSI)-based approach that increases the resolution of molecular proxy records to the µm-scale (Wörmer et al., 2014; Alfken et al., 2019; Wörmer et al., 2019). We applied this approach to varved sediment sections from SBB box core SPR0901-05BC (N34° 16' 56.496", W120° 2' 20.436", 588 m water depth). We created $U^{K'}_{37}$- and GDGT-based proxy records (CCaT, TEX^{L}_{86}) with approximately monthly resolution. These records were directly compared to a 25-year record from 1984-2009 of seasonally-measured instrumental water column data from the California Cooperative Oceanic Fisheries Investigation (CalCOFI) station 81.8 46.9 (CalCOFI). The comparison of these high-resolution proxy and instrumental datasets allow us to: i) investigate small-scale differences between these two molecular proxy types; ii) identify alternative oceanographic factors that shape the sedimentary proxy records; and iii) evaluate the sensitivity of these molecular proxies to large-scale oceanic and atmospheric oscillations such as ENSO, PDO or NPGO.

IV.2. Results and discussion

Three molecular proxy systems sensitive to marine SST are amenable to MSI: the alkenone-based $U^{K'}_{37}$ and the GDGT-based CCaT and TEX^{L}_{86}. The conventionally used TEX_{86} cannot be determined because the crenarchaeol isomer used in its calculation has the same exact mass as crenarchaeol and is therefore not separable (cf. Wörmer et al., 2014). Of the two GDGT-based proxies, CCaT provides better data quality and enables a higher temporal resolution as it is based on the two major compounds, GDGT-0 and GDGT-5, while TEX^{L}_{86} incorporates the signals from the minor compounds GDGT-1, GDGT-2, and GDGT-3 and is thus more susceptible to analytical noise.

The age model of the subsampled SBB box core SPR0901-05BC was established by identification of specific marker layers on the X-radiographed contact print and additional varve counting, allowing for a precision of ± 1 year for the data presented in this study (Schimmelmann and Lange, 1996).

To enable robust comparison between the two GDGT-based proxy ratios, we reduced the TEX^{L}_{86} to a quarterly resolution (i.e. 0.25 year) to collect a sufficient number of successful spectra (cf. methods). Despite common concerns that the inclusion of GDGT-0 in SST proxies may result in weaker relationships with SST due to its diverse archaeal sources (Schouten et al., 2002), the strong correlation of the TEX^{L}_{86} and CCaT records (Fig. 1A, Spearman´s rank correlation coefficient $r_s = 0.705$, $p < 0.05$) suggests that for SBB sediment in the studied interval, both compound groups are largely derived from the same biological source, that is, planktonic Thaumarchaeota.

IV.2.1. Different responses of alkenone- versus tetraether-based proxies to seasonal SST variation

The approximately monthly-resolved CCaT and $U^{K'}_{37}$ records exhibit distinct patterns (Fig. 1A, B), suggesting that these two proxies respond to different processes. Only the $U^{K'}_{37}$ (Fig. 1B) resembles the seasonal temperature profile derived from instrumental measurements and integrated for 0 to 30 m water depth (Fig. 1C; cf. methods and SI Appendix for calculation of spatial averages), thus showing an annual cyclicity for most parts of the record. As haptophyte production in SBB is mainly limited to the upper 30 m (Herbert et al., 1998), we used the measurements from this depth interval as reference. Transferred into SST (Prahl et al., 1988), the reconstructed $U^{K'}_{37}$ temperatures vary between 12.5 and 16.3 °C - a slightly narrower range compared to the instrumental data (10.4 – 20.0 °C). The lower amplitude of our $U^{K'}_{37}$ record could indicate a varying depth of haptophyte production. The chlorophyll *a* maximum can be found at an average water depth of 14.4 m but varies between 0 and 49 m. Assuming the alkenone export depth oscillates similarly, the corresponding temperature range at the chlorophyll *a* maximum would be 11.0 to

18.4 °C, closer to the proxy record. The difference in instrumental water temperature and calculated SST may also reflect a physiological response to nutrient availability in the surface water, as has been previously noted in culture studies (Conte et al., 1998; Epstein et al., 1998; Prahl et al., 2003), but to our knowledge not yet in the sedimentary record. Since nutrient concentrations in the haptophyte depth habitat vary with the seasonal upwelling, i.e. higher nutrient concentrations during periods of upwelling and thus colder SST, we systematically investigated this effect in the following.

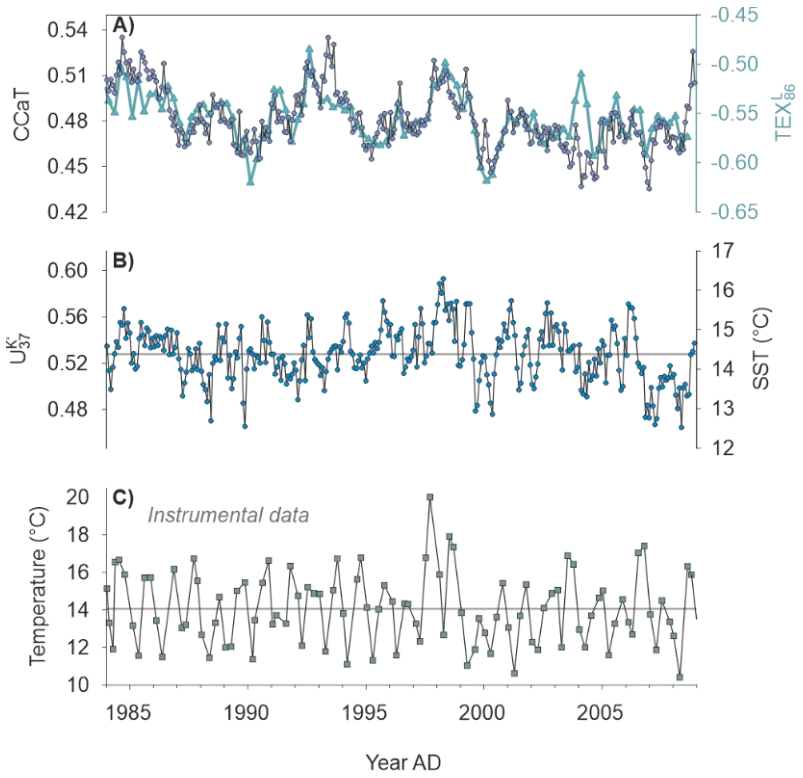

Fig. 1: *Records of molecular SST proxies in comparison to instrumental measurements. Monthly-resolved CCaT and quarterly-resolved TEX^L_{86} records (A) and $U^{K'}_{37}$ record (B) compared to seasonally measured water temperature integrated for 0 to 30 m water depth from the California Cooperative Oceanic Fisheries Investigation (CalCOFI) station 81.8 46.9 (C) from AD 1984 to 2009. Spearman´s rank correlation coefficient r_s = 0.705 ($p < 0.05$) between CCaT and TEX^L_{86} at quarterly resolution. Horizontal grey lines in B) and C) shows the 25-year means of the temperature for the $U^{K'}_{37}$ SST and the instrumental temperature, i.e. 14.38 °C and 14.06 °C, respectively.*

The comparison of the $U^{K'}_{37}$ with the CCaT and the TEX^L_{86} (Fig. 1) indicates that the $U^{K'}_{37}$ records the yearly cycle and broadly captures the SST range of the top 30 m of the water column, while the archaeal lipid-based proxies show patterns that mostly lack annual cyclicity and instead exhibit dominant multi-annual cycles (Fig. 1A, B).

IV.2.2. Thaumarchaeal proxies integrate characteristics of the entire water column

The main habitat of marine Thaumarchaeota and corresponding export depth of isoprenoidal GDGTs are indicated by the concentration maximum of nitrite, i.e. the initial product of thaumarchaeal ammonium oxidation (Massana et al., 1997; Murray et al., 1999; Hurley et al., 2018). The poor relationship between variations of GDGT-based SST estimates and surface water temperature is thus not unexpected and has been described previously for the SBB (Huguet et al., 2007). Assuming that a vertically alternating thaumarchaeal habitat depth contributes to the signal recorded in the sediment, as suggested by Huguet et al. (2007), we examined relationships with the temperature of the depth interval extending from the nitrite maximum 50 m downward. Between 1984 and 2009, the nitrite maximum in the SBB varied between the surface and 73 m water depth. Even though CCaT-based SST estimates of 9.8 to 16.9 °C are more similar to the water temperature at this depth range (9.4 to 16.1 °C) than to surface waters, the CCaT profile and the water temperature at the depth range of the nitrite maximum are not correlated (r_s = 0.088, p > 0.05.; SI Appendix Fig. S1).

In order to identify drivers of the molecular proxy signal exported to the sediment, we examined CCaT, TEX_{86}^{L}, and $U_{37}^{K'}$ profiles for the time period 1984-2009 in relation to coeval seasonally measured temperature, salinity, oxygen, and nutrients in the water column at CalCOFI station 81.8 46.9. This period was chosen because it features the most complete dataset with respect to temporal coverage and number of variables determined within the time span covered by our sediment core. To facilitate correlation analysis, various water column characteristics were integrated for different depth intervals and the age model was further refined by fixing the minima in the $U_{37}^{K'}$ profile to the corresponding minima in the temperature profile averaged from 0 to 30 m water depth. Tie points were set within the range of the precision of the age model (± 1 year) and are presented in SI Appendix, Table S1. The retuned CCaT and $U_{37}^{K'}$ records, as well as the instrumental data, were linearly interpolated with a quarterly (0.25 year) spacing. As the sampling depth of the bottom water is variable in the CalCOFI data set (Fig. 2B), the lower boundary of the water parcels including the deepest sampling points is referred to as BW (bottom water).

The combination of seasonal upwelling and its low-frequency interannual variability due to large-scale fluctuations in the California Current System (CCS) is visualized with the salinity and oxygen profiles of SBB waters integrated from 50 m – BW from AD 1984 – 2009 (Fig. 2A). During years of intense upwelling, relatively saline, oxygen-depleted water reaches the surface. Years with reduced upwelling, such as the 1997/1998 El Niño have the opposite pattern (Fig. 2A). Notably, the CCaT (as well as TEX_{86}^{L}) mirrors this pattern, with low values during periods of

intense upwelling and *vice versa* (Fig. 2). Since CCaT has a poorer correlation with temperature relative to the chemical parameters influenced by upwelling intensity, the CCaT pattern is not simply driven by the lower temperature of upwelled waters (Fig. 3).

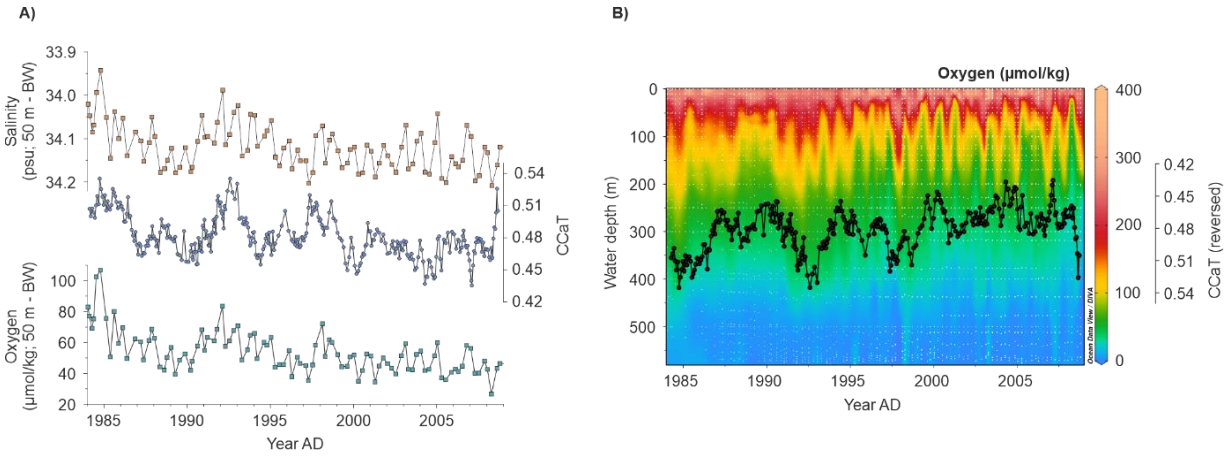

Fig. 2: *Response of thaumarchaeal proxies to subsurface water column properties. (A) Comparison of salinity and oxygen profiles integrating the water parcel from 50 m depth to bottom water (BW) from CalCOFI station 81.8 46.9 with age-refined CCaT. (B) Contour plot of oxygen concentrations in the entire water column from AD 1984 – 2009 at CalCOFI station 81.8 46.9 overlaid with age-refined CCaT on a reversed scale. Small white dots in B) show CalCOFI measurements. Map has been generated using Ocean Data View (Schlitzer; ODV5, http://odv.awi.de).*

Systematic examination of the molecular proxies in relation to the upwelling-related properties salinity, oxygen, temperature, and nutrient concentrations across 14 distinct depth intervals of the water column (further details SI Appendix) revealed that correlations of the CCaT profile with salinity and oxygen concentrations were strongest when integrated for the depth interval from 50 m - BW (Figs. 2, 3, SI Appendix Table S2). The CalCOFI data profiles (SI Appendix, Fig. S2) show that this depth interval reflects the water column below the photic zone. For the same depth interval moderate negative correlations exist with phosphate and silicate, the two nutrients accumulating in the BW (Fig. 3, SI Appendix Table S2). Even though thaumarchaeal biomarkers are used as SST proxies, only a weak correlation between surface water temperature (0 - 50 m) and CCaT was found ($r_s = 0.260$, $p < 0.05$ for CCaT; no significant correlation for TEX_{86}^{L}, $r_s = 0.165$, $p > 0.05$; Fig. 3). By including a larger water parcel, i.e. upper 100 m for CCaT and 50 – 200 m for TEX_{86}^{L}, the Spearman´s rank correlation coefficients slightly increase ($r_s = 0.265$, $p < 0.05$ for CCaT; $r_s = 0.236$, $p < 0.05$ for TEX_{86}^{L}). Interestingly, in surface waters, the CCaT is most strongly correlated with nitrate and nitrite (Fig. 3). This is consistent with the key role of Thaumarchaeota in nitrification and the previously demonstrated link between GDGT cyclization and nitrifying activity (Hurley et al., 2016).

The results of our correlation analysis for various depth intervals (Fig. 3) demonstrate the weaker connection of the CCaT to water column properties in the surface ocean and increasing correlative relationships with increasing extent of the averaged depth interval. The stronger correlations with increasing thickness of the water parcel are suggestive of two conceivable scenarios, whose relative importance cannot be determined on the basis of the available data: (i) Thaumarchaeota are known to inhabit the entire water column (Karner et al., 2001). However, subsurface depths beneath the photic zone are commonly viewed as hotspots for the export of thaumarchaeal lipids (Massana et al., 1997; Murray et al., 1999; Hurley et al., 2018) although there is evidence of export from deeper layers as well (Taylor et al., 2013). The basin topography of the SBB, with low-oxygen conditions below sill depth, may enhance upward export of thaumarchaeal lipids from deeper waters. (ii) Seasonal monitoring of the whole water column may more efficiently capture the changes driving proxy variability than data from a vertically constrained water mass, thus resulting in more significant correlations with the continuously exported signal.

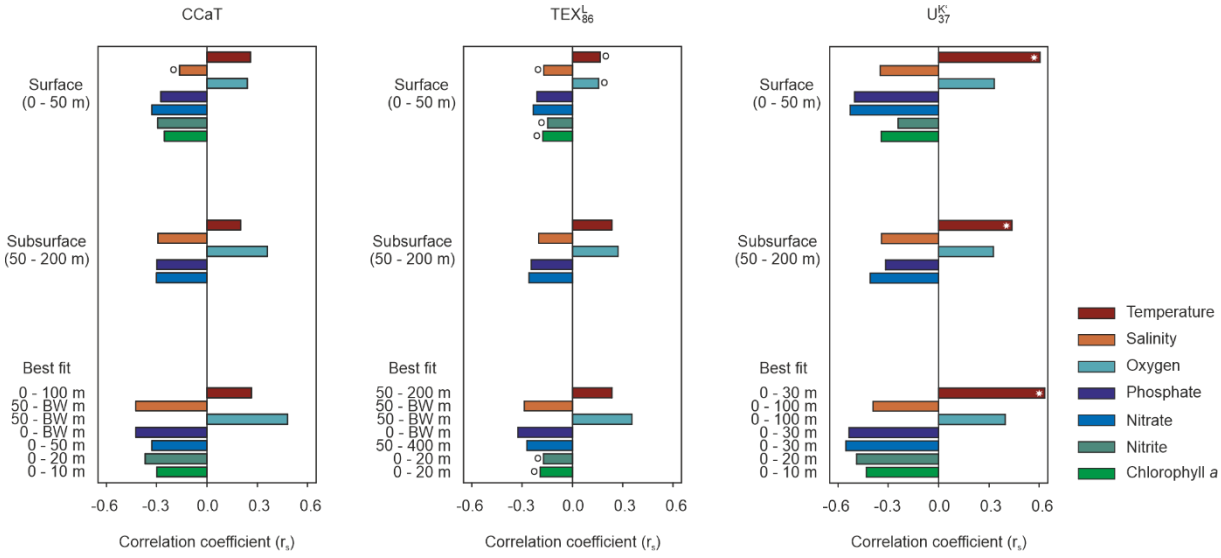

Fig. 3: *Correlation analysis between high-resolution proxy records and water column characteristics. Spearman´s rank order coefficients (r_s) between CCaT, TEX^{L}_{86}, and $U^{K'}_{37}$ and water column properties integrated for surface (0 – 50 m) and subsurface (50 – 200 m) waters and for the depth intervals with the strongest correlations for the time AD 1984 – 2009. For correlation, proxy and CalCOFI data from station 81.8 46.9 were linearly interpolated with 0.25 (quarterly) spacing; p<0.05; ○ no significant correlation; * note that the correlation of $U^{K'}_{37}$ with temperature was enhanced by the refinement of the age model based on defining tie points between these two variables.*

IV.2.3. Nutrients influence thaumarchaeal and haptophyte-derived SST proxies

Culture experiments reveal no systematic change in GDGT cyclization with salinity (Wuchter et al., 2004; Elling et al., 2015), and if oxygen concentrations had a direct impact, we would expect the opposite effect of what is observed, i.e. higher cyclization with decreasing

oxygen concentration (Qin et al., 2015). We therefore suggest that the inverse correlation of CCaT with salinity and the positive correlation with oxygen (Figs. 2, 3) are based on indirect relationships, and that the GDGT signal exported to and preserved in the sediments is instead influenced by the supply of nutrients associated with the upwelled oxygen-depleted waters of elevated salinity.

The negative correlations of GDGT-based proxies with nutrients (Fig. 3) are consistent with observations by Hurley et al. (2016) and Evans et al. (2018) who showed a dependency of GDGT cyclization on ammonia oxidation rate and ammonia supply, respectively. Ammonium concentrations are only available in the CalCOFI dataset from 2008 onwards, precluding an evaluation of its relationship with the thaumarchaeal proxies. While ammonium delivery from deeper to shallower waters to the surface *via* upwelling is not the major supply route, we expect strong coupling of the ammonium supply with upwelling intensity due to the stimulation of primary production and remineralization of organic matter, which results in ammonium release. The positive correlation with the temperature of the upper 100-m water depth shows that an unambiguous attribution to one driving factor is impossible as both temperature and nutrients are directly influenced by upwelling. Consequently, in the SBB CCaT, and by analogy TEX_{86}^{L} (Figs. 1, 3), primarily record water column properties associated with varying upwelling intensity.

In contrast to the thaumarchaeal proxies, the $U_{37}^{K'}$ is strongly correlated with SST (Fig. 3, SI Appendix Table S2). Besides temperature, strong to moderate negative correlations also exist with nutrient concentrations in surface water (Fig. 3). The correlations with nutrients could either indicate an indirect effect, since the upwelling-induced supply of nutrients tracks the seasonal temperature signal, or a direct effect of nutrients on the $U_{37}^{K'}$ signal. A potential direct effect would be consistent with observations from batch cultures of *Emiliania huxleyi,* which revealed a systematic decline in $U_{37}^{K'}$ values of up to 0.11 units (~3 °C) with a decrease in nitrate (Prahl et al., 2003).

In order to clarify the potential impact of nutrients, we investigated the influence of nitrate concentrations on the residuals of $U_{37}^{K'}$ SST and measured SST in the haptophyte habitat depth (0 – 30 m; Fig. 4). Indeed, we observed a clear relationship between nitrate concentrations and SST residuals. The majority (27 out of 33 values) of $U_{37}^{K'}$-derived SST estimates with nitrate concentrations <2.1 µmol/L are lower than actual SST, while the majority of $U_{37}^{K'}$ SST values (54 out of 65) with nitrate ≥2.1 µmol/L exceed actual SST (Fig. 4). This impact of seasonally variable nutrient concentrations on sedimentary $U_{37}^{K'}$ is consistent with observations in cultures and sediment traps by Prahl et al. (2003). This nitrate effect can additionally account for (i) the lower amplitude of our $U_{37}^{K'}$ SST record compared to actual SST, especially during years of strongly

reduced upwelling such as the 1997/1998 El Niño, and (ii) the lower slope of the $U_{37}^{K'}$ *vs.* SST relationship observed in our study (Fig. 4A) relative to that observed in global datasets (Müller et al., 1998). These results, enabled through unprecedented temporal resolution in sedimentary biomarker measurements, provide mechanistic insights into $U_{37}^{K'}$ signal formation. Presumably, such effects of nutrient availability have not been observed in previous studies using conventional protocols for biomarker analysis because typical sample volumes integrate periods of decades to centuries and thus provide information on long-term average conditions. In this context, we note that the 25-year average SST record reconstructed *via* the $U_{37}^{K'}$ is essentially equal to the corresponding instrumentally-determined SST (14.4 °C *vs.* 14.1 °C, respectively; Fig. 1). Nevertheless, our results imply that the influence of nutrients on the sedimentary $U_{37}^{K'}$ signal should be carefully considered in paleoenvironmental applications, especially when there is evidence that the studied systems oscillated between oligotrophic and eutrophic conditions.

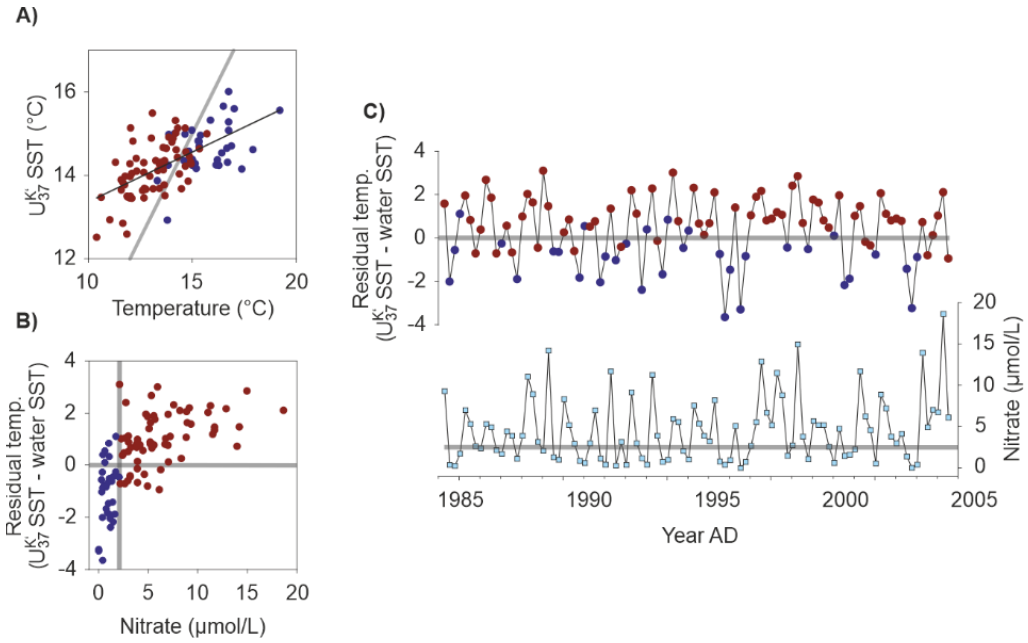

Fig. 4: *Relationship of surface water nitrate concentrations with $U_{37}^{K'}$ reconstructed SST. (A) $U_{37}^{K'}$ SST versus instrumental water temperature from 0 – 30 m water depth at CalCOFI station 81.8 46.9 with the 1:1 line shown in grey. (B) Temperature residuals (calculated $U_{37}^{K'}$ temperatures minus water temperature at 0 – 30 m water depth) against nitrate concentrations for 0 – 30 m water depth. The zero residual and nitrate threshold of 2.1 µmol/L are designated by gray lines. (C) Time series of temperature residuals (top panel) and nitrate concentration for 0 – 30 m water depth from AD 1984 – 2009. $U_{37}^{K'}$ values corresponding to nitrate concentrations below (above) 2.1 µmol/L are colored in blue (red) in all figure panels. Temperature residuals were calculated with age-refined $U_{37}^{K'}$ data and linearly interpolated with 0.25-year (quarterly) resolution of $U_{37}^{K'}$ and CalCOFI data.*

IV.2.4. Thaumarchaeal lipids respond to major oceanographic variations in the North Pacific

The SBB is influenced by the large-scale fluctuations of the CCS (Field et al., 2006b). Coastal upwelling intensities in the CCS are weaker (stronger) during the positive (negative) PDO phase (Mantua et al., 1997; Chavez et al., 2003; Chhak and Di Lorenzo, 2007) and during El Niño (La Niña) events (Lynn et al., 1995; Bograd and Lynn, 2001; Chavez et al., 2002; Jacox et al., 2015). Whereas the PDO and ENSO characterize changes of the SST field in the Pacific at timescales of 20 – 30 years and 6 to 18 months, respectively (Mantua and Hare, 2002), the NPGO correlates with fluctuations in nutrients, salinity, and chlorophyll *a* as a result of interannual and decadal variations in wind-driven upwelling (Di Lorenzo et al., 2008).

Examination of the relationship between the CCaT record and the three indices that capture the variation of PDO, ENSO, and NPGO reveals the similarity of the proxy record to these oscillations (Fig. 5). The inverse relationship between CCaT and NPGO (Fig. 5C) is supported by significant correlation between NPGO and salinity in the Southern California Current between 30°N and 38°N (Di Lorenzo et al., 2008). Additionally, the apparent resemblance of CCaT to both ENSO and PDO variability (Fig. 5 A, B) supports our suggestion of the CCaT, and by analogy the TEX_{86}^{L}, being sensitive to low-frequency variations in the upwelling intensity. The correlations between CCaT and local water column characteristics together with the ability of CCaT to capture the main features of NE Pacific Ocean-climate indices demonstrate the potential of the CCaT proxy to reconstruct past upwelling variability associated to large-scale climatic oscillation in the CCS and the Pacific climate.

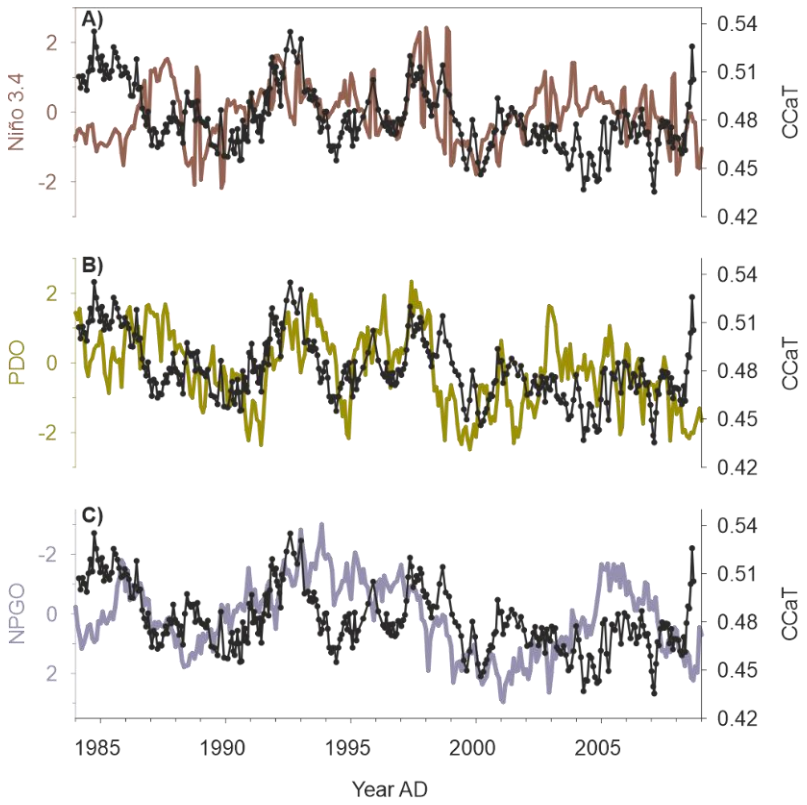

Fig. 5: *Imprint of (sub)decadal oceanographic variability in the North Pacific on the CCaT record. ENSO presented as Niño 3.4 (A), PDO (B) and reversed NPGO (C) compared to age-refined monthly-resolved CCaT from AD 1984 – 2009.*

Our study shows that the high spatial resolution obtained by MSI enables investigation of the sub-annual differences of archaeal *vs.* haptophyte lipids, both thought to be sensitive to SST variations. The monthly-resolved $U^{K'}_{37}$ records the annual cycle of SST variation, but its amplitude is dampened by a nutrient-effect, which so far has been only shown in culture experiments and was indicated in suspended particulate matter (Prahl et al., 2003). Thaumarchaeal-based proxies lack a strong correlation with SST. However, in varved sediments from the SBB, the high-resolution CCaT records variations in water column characteristics associated with low-frequency upwelling variability linked to Pacific climate variability on interannual to decadal timescales.

IV.3. Methods

IV.3.1. Sediment samples and instrumental data

Santa Barbara box core SPR0901-05BC (N34° 16' 56.496", W120° 2' 20.436", 588 m water depth) was collected from the center of SBB. At the time of its subsampling, the 30-cm slab from the box core was about 40 cm in length and spanned AD 1900 – 2009. An X-ray photograph of the slab was taken to visualize the varves by their density differences. The age model of 05BC was implemented by identification of specific marker layers and additional varve counting.

The sediment slab was subsampled into ~5-cm sections, frozen at -80 °C, freeze-dried and prepared for µm-scale molecular imaging according to (Alfken et al., 2019). This study focuses on the upper ~ 7.0 cm of the sediment slab corresponding to AD 1984 – 2009. This time period can be directly compared to seasonally measured instrumental water column characteristics such as temperature, nutrients, oxygen and salinity from California Cooperative Oceanic Fisheries Investigation station 81.8 46.9 at the center of SBB (N34°16' 29.64'', W120° 1' 30") (CalCOFI). Instrumental data cover the entire water column (Fig. 2B) with dominant spacing of 10 m for the upper 50 m of the water column, followed by a 25-m spacing until 150 m water depth, 50-m spacing down to 300 m, and data at 400 m and 500 m water depth. Additional data exist for various depths irregularly distributed between the main intervals and down to 580 m. Only the years 1984 to 1985, and the first sampling in 1986 do not include data below 550 m water depth, and have the deepest data taken between 400 and 500 m water depth. To account for irregular data coverage and smaller sampling intervals in the surface water, values representative of a defined water parcel were calculated by the sum of all integrals between available measurement depths, divided by the size of the water parcel.

For comparison to molecular proxy records, ENSO is represented by the Niño 3.4 region (5°N – 5°S, 120° - 170°W), and the PDO dataset used in this study was obtained from the Joint Institute for the Study of Atmosphere and Oceans (JISAO). Both time series are available from the U.S. National Oceanic and Atmospheric Administration (NOAA; https://www.esrl.noaa.gov/psd/gcos_wgsp/Timeseries/). The index for the NPGO (Di Lorenzo et al., 2008) can be downloaded at http://www.o3d.org/npgo/.

IV.3.2. Mass spectrometry imaging of molecular proxies

Mass Spectrometry Imaging (MSI) was performed with a 7T solariX XR FT-ICR-MS coupled to a MALDI source equipped with a Smartbeam II laser (Bruker Daltonik, Bremen, Germany). Embedded and frozen ~5-cm-long sediment sections were sliced with a cryomicrotome (Microm HM 505 E Cryostat, GMI, Ramsey, Minnesota, USA) into 60-µm-thick, 5-cm-long slices and adhered onto indium tin oxide (ITO)-coated glass slides. Mass spectra for isoprenoidal GDGTs and alkenones were generated on individual slices with a 95% data reduction during acquisition in the ftmsControl software program (Bruker Daltonik). To improve sensitivity spectra were acquired in continuous accumulation of selected ions (CASI) mode with an isolation window of m/z = 1,320 ± 40 for GDGTs and 550 ± 30 for alkenones. External mass calibration was performed in electrospray ionization mode with sodium trifluoroacetate (NaTFA), followed by internal lock mass calibration of single MSI spectra on the Na^+ adduct of $GDGT5_{MS}$ (m/z 1314.22636) and the Na^+ adduct of pheophorbide (m/z 557.25231). The term $GDGT5_{MS}$ accounts for the m/z value of all GDGTs with five double bond equivalents detected by FT-ICR-MS. For the ~7.0 cm (25 years)

section analyzed in this work, about 14,000 single spectra were generated with a large laser focus at a raster width of 200 µm. Laser power, number of shots and frequency were optimized for best signal intensities with final settings of 40%, 500 shots and 1,000 Hz, respectively, for GDGTs and 35%, 700 shots and 1,000 Hz, respectively, for alkenones.

The CCaT calculation followed the equation by Wörmer et al. (2014) with the modified nomenclature of GDGT-5_{MS} for the reasons described above.

$$1. \quad CCaT = \frac{GDGT\text{-}5_{MS}}{GDGT\text{-}0 + GDGT\text{-}5_{MS}}$$

The TEX_{86}^{L} including the minor GDGTs with one, two, and three cyclopentane rings was calculated after Kim et al. (2010). As quantities of GDGT-3 were minor, successful spectra were defined as spectra which include GDGT-2 and GDGT-1.

$$2. \quad TEX_{86}^{L} = \log \frac{GDGT\text{-}2}{GDGT\text{-}1 + GDGT\text{-}2 + GDGT\text{-}3}$$

The alkenone-based $U_{37}^{K'}$ index is based on the equation by Prahl and Wakeham (1987) with the SST transformation according to Prahl et al. (1988).

$$3. \quad U_{37}^{K'} = \frac{C_{37:2}}{C_{37:2} + C_{37:3}}$$

$$4. \quad U_{37}^{K'} = 0.034T + 0.039$$

Before averaging spectra along each horizon to create a downcore profile at 200-µm resolution, the mapped areas were corrected for tilted laminae. The tilt correction was done by visual identification of single laminae in the X-ray photograph and selection of a minimum of four tie points per lamina. The inverse spatial 2D transformation to horizontal laminae was done using *tforminv* in MATLAB 2016a (The MathWorks, Natick, USA). Downcore profiles with the temporal resolution specified were generated by averaging values along individual layers of the transformed data if at least 10 data points were available to satisfy data quality criteria described recently (Wörmer et al., 2019). A detailed description can be found in the SI Appendix.

Acknowledgments

We thank Tiffany Napier, Heiko Pälike and Jürgen Pätzold for helpful discussion during the course of the project and Tiffany Napier also for constructive comments on an earlier version of this manuscript. This research was supported by the European Research Council under the European Union´s Horizon 2020 Research and Innovation Programme (grant agreement No.

670115 ZOOMECULAR; PI Kai-Uwe Hinrichs). Raw and processed data will be available on PANGAEA once the manuscript is accepted.

IV.4. Supporting information

IV.4.1. Processing of µm-scale MSI-based data maps

To create a quasi-continuous record of the µm-scale mapped biomarkers, all ~5-cm sections were assembled to the original size of the sediment slab using MATLAB 2016a (The MathWorks, Natick, USA). This was achieved by registering the images of the sediment sections produced by the M4 Tornado µ-XRF mapping system (version 1.3.0.3273, Bruker Nano GmbH, Berlin, Germany) to the negative of the X-ray photograph of the intact ~30-cm slab of SPR0901-05BC which was used as reference (coordinate system in pixel units). Three teach points were chosen on each ~5-cm section image and three corresponding teaching points on the X-ray photograph. The corresponding xy-spot coordinates of the teaching points on the measured ~5-cm slices were read off from Bruker Daltonics flexImaging Software (version 4.1, Bruker Daltonics GmbH, Bremen, Germany). Using the spot coordinates of the teaching points from the individual cryomicrotome slices as moving points and the pixel coordinates of the teaching points on the X-ray image as fixed reference points, the data maps of the molecular proxies (CCaT, TEX_{86}^{L} and $U_{37}^{K'}$) were loaded as xyz-coordinates and mapped onto the X-ray photograph using *fitgeotrans.*

The contrast enhanced X-ray photograph was loaded with *imread*. To correct the tilted laminae in the sediment slab, single, coeval layers in the X-ray photograph of the sediment slab were identified and at least four tie points along the laminae were chosen. Corresponding tie points for the corrected horizontal layers were determined by using the x-coordinates of the tie points selected in the previous step and setting the y-coordinates to the value of the leftmost tie point. The resulting list of tuple pairs, as pixel coordinates, was used to establish a transformation using a slightly modified *tforminv* function resulting in a new piecewise linearly transformed pixel grid of the X-ray photograph with horizontal laminations. This transformation was also applied to the xy spot-coordinates of the xyz-data of the previously registered individual slices. By knowing the exact number of pixels and spots making up the X-ray image and the original size of the sediment slab, respectively, the data were further transformed to depth and age using the tie points of the age model.

The combination of individual slices to one continuous record was done using *vertcat.* Single layers were then averaged at a defined layer thickness along the y-axis with a minimum number of spots set as a threshold to increase data quality. This quality threshold was set to 10 data values according to Wörmer et al. (2019) and the layer thickness for CCaT and $U_{37}^{K'}$ was set to

the spot distance of 200 µm, which corresponds to roughly monthly resolution and thus a spacing of 0.08 years for the time domain. As the success rate of spectra in which the minor GDGTs with one, two, and three cyclopentane rings were detected was ~50% lower than for spectra needed to generate CCaT and $U^{K'}_{37}$ (~90%), the TEX^{L}_{86} downcore profile was generated by averaging at a broader resolution of 500 µm and 0.25 years to assure that the quality threshold of 10 data points was met.

IV.4.2. Age model adjustment for correlation of MSI-based data with CalCOFI station 81.8 46.9

To allow a correlation analysis of proxy data and instrumental water column data at CalCOFI station 81.8 46.9 (CalCOFI), in total 26 tie points were set between the minima in the integrated profile of the water temperature from 0 - 30 m water depth and the minima in the $U^{K'}_{37}$ profile using the AnalySeries 1.1 Software (Paillard et al., 1996). Tie points are displayed in Table S1.

IV.4.3. Correlation of high-resolution CCaT data with CalCOFI station 81.8 46.9

For the comparison to the MSI-based CCaT, TEX^{L}_{86}, and $U^{K'}_{37}$ data, 14 depth intervals covering the photic zone, the entire water column, and excluding the photic zone were used. To account for unevenly spaced sampling depths in the CalCOFI data, values of measured water column properties were calculated by the sum of all integrals between available measurement depths, divided by the size of the depth interval.

For the photic zone, five depth intervals starting at 0 m and increasing in height by 10 m were used. The entire water column was divided in four intervals starting a 0 m and increasing in height by 100 m and one interval from 0 m to the deepest data point of the bottom water (BW). To exclude the photic zone, four intervals were chosen, i.e. 50 – 200 m, 50 – 300 m, 50 – 400 m, and 50 – BW m.

Correlation analysis was performed using SigmaPlot for Windows Version 11.0 (Systat Software, San Jose, CA).

Table S1: *Age tie points between $U_{37}^{K'}$ profile (age SPR0901-05BC) and profile of water temperature from 0 – 30 m water depth at CalCOFI station 81.8 46.9 for AD 1984 – 2009.*

Age 05BC	Age CalCOFI
1984.20	1984.29
1985.32	1985.37
1987.24	1987.21
1988.44	1988.37
1989.32	1989.29
1989.88	1990.21
1991.16	1991.04
1992.12	1991.62
1993.24	1992.29
1993.80	1993.29
1995.00	1994.21
1996.20	1995.29
1996.60	1996.29
1997.80	1997.29
1999.00	1998.29
1999.64	1999.29
2000.36	2000.29
2001.48	2001.29
2002.12	2002.29
2003.32	2003.29
2004.12	2004.29
2005.16	2005.29
2005.80	2006.29
2007.24	2007.29
2008.36	2008.29
2008.84	2008.62

Table S2: *Top three Spearman´s rank order correlation coefficient (r_s) between CCaT, TEX_{86}^{L}, and $U_{37}^{K'}$ with water column data at CalCOFI station 81.8 46.9. For correlation, proxy and CalCOFI data were linearly interpolated with a 0.25 (quarterly) spacing. Correlation coefficients are only shown for significant correlations ($p < 0.05$). BW stands for bottom water.*

	CCaT		TEX_{86}^{L}		$U_{37}^{K'}$	
		depth interval		depth interval		depth interval
Temperature	0.265	0 - 100 m	0.236	50 – BW m	0.633	0 – 30 m
	0.260	0 - 50 m			0.620	0 – 20 m
	0.254	0 - 40 m			0.605	0 – 50 m
Oxygen	0.482	50 – BW m	0.355	50 - BW m	0.397	0 - 100 m
	0.429	50 – 400 m	0.320	50 - 400 m	0.380	0 – 40 m
	0.421	0 – 400 m	0.316	0 - 400 m	0.351	0 - 200 m
Salinity	-0.424	50 – BW m	-0.287	50 – BW m	-0.392	0 – 100 m
	-0.393	0 - BW m	-0.279	0 – BW m	-0.380	0 – BW m
	-0.360	50 – 400 m	-0.247	50 - 400 m	-0.371	0 – 200 m
Phosphate	-0.425	0 – BW m	-0.326	0 – BW m	-0.535	0 – 30 m
	-0.420	50 – BW m	-0.324	50 – BW m	-0.526	0 – 20 m
	-0.308	0 – 400 m	-0.252	0 – 200 m	-0.501	0 – 50 m
Silicate	-0.361	0 – BW m	-0.287	0 – BW m	-0.474	0 – 50 m
	-0.345	50 – BW m	-0.275	0 – 40 m	-0.461	0 – 30 m
	-0.286	0 – 50 m	-0.272	50 – BW m	-0.452	0 – 100 m
Nitrate	-0.329	0 – 50 m	-0.272	50 – 400 m	-0.554	0 – 30 m
	-0.324	0 – 40 m	-0.272	50 – 300 m	-0.547	0 – 20 m
	-0.317	0 – 100 m	-0.268	0 – 400 m	-0.528	0 – 50 m
Nitrite	-0.369	0 - 20 m			-0.489	0 – 20 m
	-0.360	0 - 30 m			-0.487	0 – 10 m
	-0.293	0 - 50 m			-0.382	0 – 30 m
Chlorophyll *a*	-0.299	0 – 10m			-0.431	0 – 10 m
	-0.287	0 – 20 m			-0.380	0 – 20 m
	-0.280	0 – 30 m			-0.351	0 – 30 m

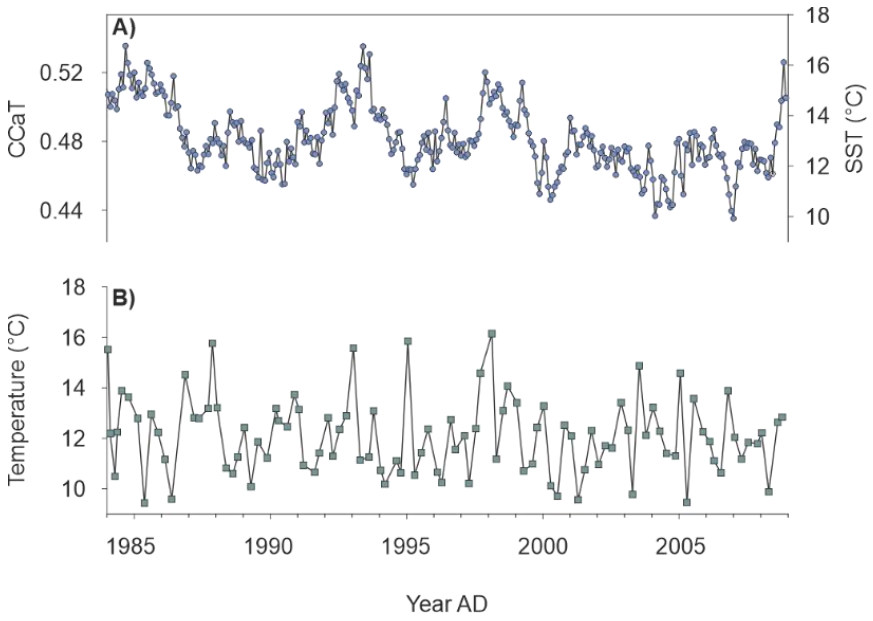

Figure S1: *Comparison of CCaT-based SST with water temperature at the presumed thaumarchaeal depth habitat in the range of the nitrite maximum. (A) Monthly-resolved transformed CCaT record compared to SST. (B) Seasonally measured water temperature from CalCOFI station 81.8 46.9 integrated for the water depth of the nitrite maximum plus 50 m (corresponding to a total depth range of 0 to 123 m) from AD 1984 to 2009. The CCaT-based SST was calculated according to (Wörmer et al., 2014).*

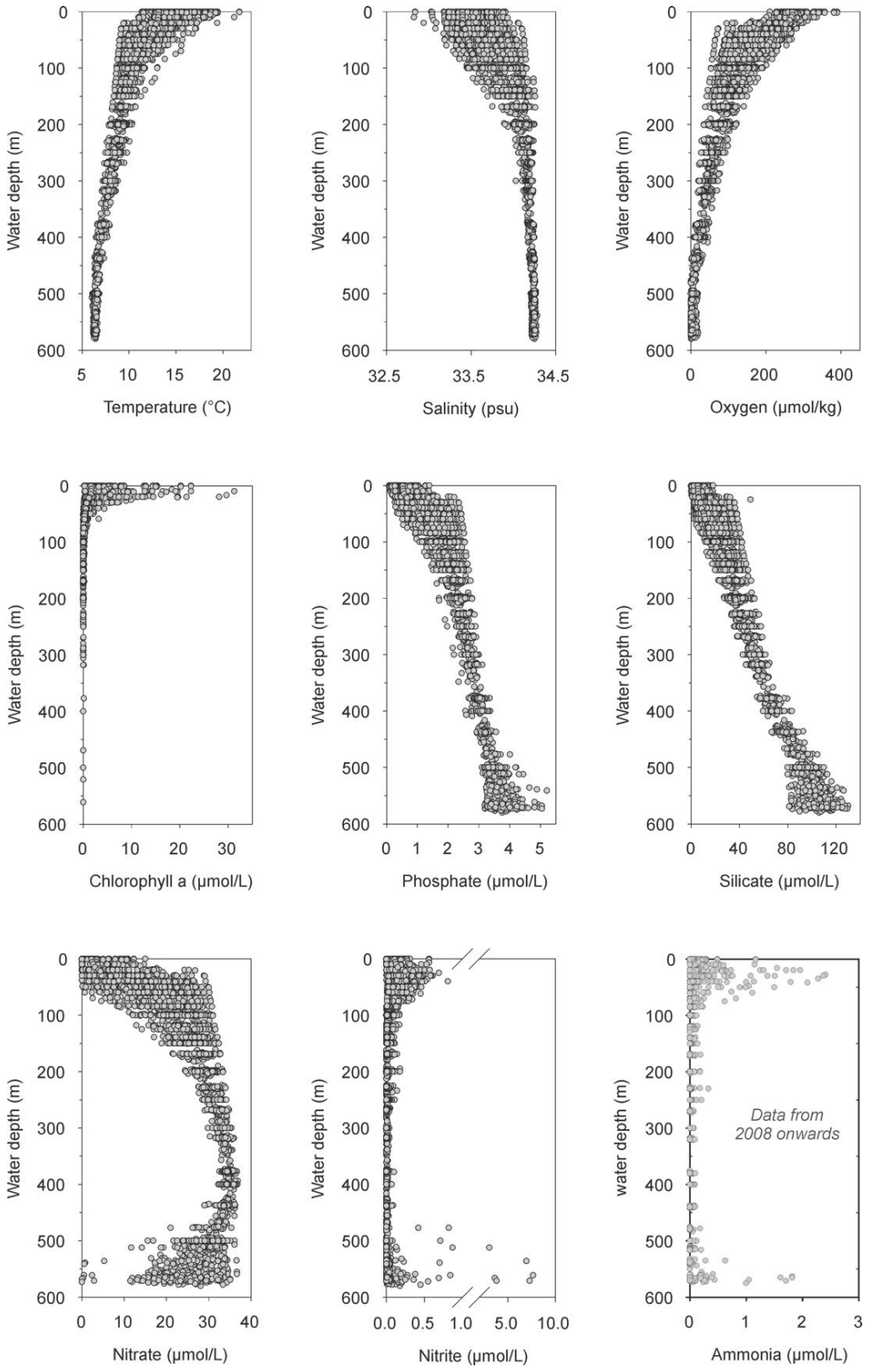

Figure S2: *Profiles of temperature, salinity, oxygen, chlorophyll a, phosphate, silicate, nitrate, nitrite, and ammonia from CalCOFI station 81.8 46.9 for AD 1984 to 2009. Ammonia concentrations are shown from 2008 onwards and are not available for the time period investigated in this study.*

CHAPTER V

A 110-YEAR MULTIPROXY RECORD OF OCEANOGRAPHIC VARIATION IN THE SANTA BARBARA BASIN, OFF SOUTHERN CALIFORNIA

Susanne Alfken[a*], Lars Wörmer[a], Julius S. Lipp[a], Marcus Elvert[a], Jenny Wendt[a], Arndt Schimmelmann[b], Kai-Uwe Hinrichs[a]

In preparation for *Earth and Planetary Science Letters*

[a] Organic Geochemistry Group, MARUM – Center for Marine Environmental Sciences and Faculty of Geosciences, University of Bremen, Leobener Str. 8, 28359 Bremen, Germany

[b] Department of Earth and Atmospheric Sciences, Indiana University, 1001 E 10th Street, Bloomington, IN 47405-1405, USA

* Corresponding author: E-mail address: salfken@marum.de

Abstract

Varved sediments from the center of the Santa Barbara Basin (SBB), off Southern California are a valuable archive for high-resolution reconstruction of past climate variability. Using mass spectrometry imaging of lipid biomarkers on a ~30 cm sediment box core, this study addresses variations of sea surface temperature (SST), low-frequency upwelling strength and bottom water redox conditions at a sub-annual resolution from AD 1900 – 2009. Overall the monthly-resolved SST variations based on the haptophyte-derived $U^{K'}_{37}$ proxy confidently record SST in the SBB and its interannual variability in response to El Niño Southern Oscillation (ENSO). The temperature increase of ~1 °C recorded for the California Current System during the 20th century is not captured by this proxy, potentially due to a concurrent decrease in upwelling efficiency leading to lower nutrient concentrations in the ocean surface. A mixed influence of ENSO, Pacific Decadal and North Pacific Gyre Oscillation on the low-frequency variations in the upwelling signal is expressed in the CCaT proxy based on glycerol dibiphytanyl glycerol tetraethers from planktonic Thaumarchaeota. Together with the redox-sensitive C_{29} stanol/stenol ratio this proxy also reveals the changing interdependency of upwelling strength and bottom water oxygen content. Until a ~mid 1970s regime shift, CCaT and the C_{29} stanol/stenol ratio are positively correlated. This suggests that periods of enhanced upwelling facilitated vertical mixing and ventilation, leading to an increase in bottom water oxygen content. In more recent sediments this relationship reverses due to an increase in stratification and thermocline deepening. Mixing and ventilation became less effective and the upwelling-induced increase in productivity and subsequent oxygen-consuming remineralization of organic matter became the driving factor of bottom water redox conditions.

V.1. Introduction

The Santa Barbara Basin (SBB) off Southern California is hydrographically situated in the California Current System (CCS), which has experienced strong changes during the past century, affecting both its physical and biological regime. Variability has been associated to large-scale climate phenomena in the North Pacific such as El Niño Southern Oscillation (ENSO; Bograd and Lynn, 2001, 2003; Venrick, 2012), Pacific Decadal Oscillation (PDO; Mantua et al., 1997; Chavez et al., 2003) or North Pacific Gyre Oscillation (NPGO; Di Lorenzo et al., 2008), as well as global warming (Roemmich and McGowan, 1995; Field et al., 2006b) and the consequent increased stratification (Palacios et al., 2004) and changes in upwelling strength (Bakun, 1990; Schwing and Mendelssohn, 1997). As a representative of the coastal region of the CCS (Field et al., 2006b), the SBB with its laminated sediments provide a natural archive of climate variability in Southern California (e.g., Soutar and Crill, 1977; Baumgartner et al., 1992; Biondi et al., 1997; Field et al., 2006a; Grelaud et al., 2009).

SBB sediments are formed by seasonally alternating input from biogenic-rich and clastic dominated material (Emery and Hülsemann, 1961; Soutar and Crill, 1977; Thunell et al., 1995; Thunell, 1998). This seasonality is largely driven by the atmospheric pressure pattern of the North Pacific High and Aleutian Low, and its forcing on the CCS. SBB waters are affected by the equatorward California Current, the poleward offshore California Undercurrent, extending north off Point Conception, and the inshore southern California Countercurrent (Fig. 1; Hickey, 1979; Hendershott and Winant, 1996). The strength of the southward flowing California Current intensifies during spring and summer in response to the equatorward winds, which are driven by the strong east-west pressure gradient between the strengthened North Pacific High and deepened continental low. The strong alongshore winds induce upwelling of cold and nutrient-rich water promoting productivity in the surface. In the fall-winter season the North Pacific High weakens, is displaced southward and the Aleutian Low strengthens, leading to a decrease in upwelling-favorable winds (Hickey, 1979; Hendershott and Winant, 1996; Thunell, 1998).

Modern SBB bottom waters in the deep center of the basin contain little dissolved oxygen due to the restricted ventilation of the basin and the inflow of waters over its deep western sill within the oxygen minimum zone (Emery and Hülsemann, 1961). Additionally, oxygen is consumed due to the enhanced productivity during upwelling and the subsequent remineralization of organic matter. Occasionally, suboxic bottom waters in the SBB can be flushed with dense and oxygenated water, which enters the basin over its western sill by strong seasonal upwelling during winter and spring north off Point Conception (Reimers et al., 1990; Bograd et al., 2002; Goericke et al., 2015). These flushing events usually lead to a mixing of the existing water and not to a complete oxygenation of the bottom water (Goericke et al., 2015).

Information on past environmental conditions are archived in the SBB sediments in the form of molecular biomarkers derived from membrane lipids of microorganisms that once inhabited the water column. These molecular fossils can be indicative of the habitat conditions the organisms needed to adapt to, but also of the prevailing redox conditions during sedimentation under which diagenetic processes took place. Retrieval of the archived signal from the sediment can be done using conventional solvent-based extraction methods, or with the recently introduced method of direct biomarker analysis *via* Mass Spectrometry Imaging (MSI; Wörmer et al., 2014; Alfken et al., 2019; Wörmer et al., 2019). Whereas the extraction-based approach is limited by the need of gram-sized sample amounts, the laser-based ionization of target molecules from the intact sample surface in MSI allows for sub-millimeter spatial resolution. Systems such as the SBB, where the biological signal from the ocean surface is deposited into the sediments within a few days (Schimmelmann and Lange, 1996), are ideal for MSI and allow for an up to monthly resolution. As shown in a recent MSI-based study of 25 years of modern SBB sediments (AD 1984 – 2009; Alfken et al., submitted), sea surface temperature (SST) reconstructions using the $U^{K'}_{37}$ proxy, indicative of the unsaturation of long-chain alkenones in haptophyte algae, (Brassell et al., 1986; Prahl et al., 1988) capture the annual SST cycle. However, the systematic comparison to various instrumental water column properties also revealed that a physiological response to nutrient availability in the haptophytes' habitat affects the absolute SST signal, leading to cold biased SSTs during reduced nutrient supply and *vice versa*. This study also showed that the CCaT proxy (Wörmer et al., 2014) based on the ratio of the two major isoprenoidal glycerol dibiphytanyl glycerol tetraethers (GDGTs) from planktonic Thaumarchaeota is correlated to subsurface oxygen, salinity and nutrient concentrations which vary according to the multi-year upwelling variability.

In the present study we applied MSI *via* matrix-assisted laser desorption/ionization coupled to Fourier transform-ion cyclotron resonance-mass spectrometry (MALDI-FT-ICR-MS) to a ~30 cm SBB box core to reconstruct variations of SST, upwelling strength and bottom water redox conditions from AD 1900 – 2009. The resulting high-resolution multiproxy record was employed to interrogate potential interdependencies between these water column properties, as well as their link to large-scale climate patterns affecting the southern CCS.

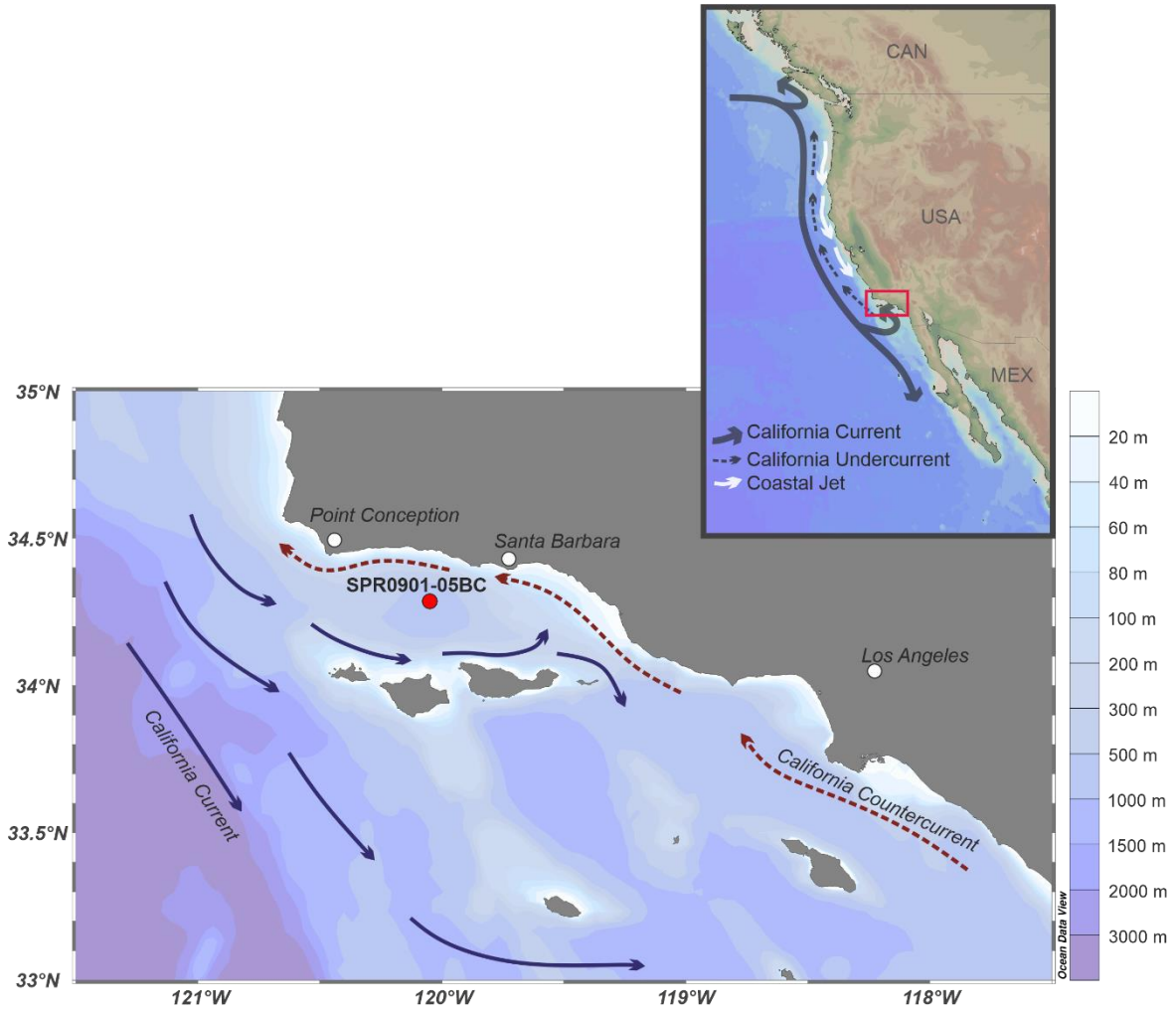

Fig.1*: Core location of SPR0901-05BC (red dot) in the center of the SBB. Arrows show the main circulation pattern within the basin. The small map at the top right shows a simplified overview of the California Current System. The area of the SBB is highlighted by the red rectangle.* Map has been generated using Ocean Data View (Schlitzer, ODV5, http://odv.awi.de).

V.2. Methods

V.2.1. Sediment sample

Box core SPR0901-05 BC (N34° 16' 56.496" W120° 2' 20.436", 588 m) was collected in central SBB (Fig. 1). The age model of the 30 cm sediment slab was established by visualization of varve couplets using X-ray photography allowing for identification of prominent markers layers and varve counting (Fig. 2). The precision of the age model based on varve counting until AD 1900 is estimated to be ± 1 year (Schimmelmann and Lange, 1996). The ~30 cm slab spanning AD 1900 – 2009 was subsampled twice using double L-channels (LL-channel) to create two overlying intact sediment sections from the same position. One LL-channel was used for the extraction-free, high resolution biomarker analysis with MALDI-FT-ICR-MS and one was further subsampled into 28 intervals for conventional extraction and lipid analysis.

V.2.2. Instrumental data

Climate indices of ENSO represented by the Niño 3.4 region (5°N – 5°S) and PDO were taken from the Joint Institute for the Study of Atmosphere and Oceans (JISAO) and are available from the U.S National Oceanographic and Atmosphere Administration (NOAA; https://www.esrl.noaa.gov/psd/gcos_wgsp/Timeseries). The NPGO index by Di Lorenzo et al. (2008) is available at http://www.o3d.org/npgo.

The monthly SST data used in this study were obtained from the NOAA Climate Data Center Extended Reconstructed Sea Surface Temperature (ERSST) V4 dataset at N°34 W°120 (http://www.esrl.noaa.gov/psd/data/gridded/data.noaa.ersst.v4.html, accessed 3 September 2019, Huang et al., 2015).

V.2.3. Extraction-free biomarker analysis with MALDI FT-ICR-MS

For MSI, the sediment from the LL-channel was split into six ~5 cm intact sections and subsequently prepared for analysis according to Alfken et al. (2019). Sample preparation included stabilization of the freeze-dried sections by embedding in a gelatin-based mixture (5% gelatin, 2% sodium carboxymethyl cellulose; Sigma Aldrich Chemie GmbH, Munich, Germany) and sectioning into sequential thin (60 µm) slices for multiple biomarker analyses using a cryomicrotome (Microm HM 505 E Cryostat, GMI, Ramsey, Minnesota, USA).

A 7T solariX XR FT-ICR-MS coupled to a MALDI source equipped with a Smartbeam II laser (Bruker Daltonik, Bremen, Germany) was used for MSI. Analysis for isoprenoidal GDGTs, alkenones and sterols were performed on individual 60 µm slices, placed on indium tin oxide coated glass slides (Bruker Daltonik, Bremen, Germany). For each compound class an individual isolation window for the continuous accumulation of selective ions (CASI) was chosen. CASI with isolation windows were set as follows: mass to charge ratio (m/z) = 1,320 ± 40 for GDGTs, m/z = 550 ± 30 for alkenones and m/z = 450 ± 150 for sterols and stanols. To assure high data quality, spectra were acquired with a 95% data reduction. External mass calibration was performed in electrospray ionization mode with sodium trifluoroacetate (Sigma Aldrich). Single MSI spectra were additionally calibrated by an internal lock mass calibration using the Na^+ adducts of $GDGT5_{MS}$ (m/z 1314.22636), pheophorbide a (m/z 557.25231) and the unspecific, but highly abundant m/z of 433.38047 corresponding to the Na^+ adduct of any $C_{30}H_{50}$ compound (e.g., squalene, diploptene). High-resolution data was produced by rastering with the laser across the sample in a defined rectangular area at a 200 µm resolution spot distance. Settings for laser power, frequency and number of shots were adjusted for optimal signal intensities. GDGTs were measured with 40% laser power, 500 shots and a frequency of 1,000 Hz, whereas alkenones and sterols were acquired with 35% laser power, 700 shots and a frequency of 1,000 Hz.

Proxy values were calculated for each individual spot based on the intensities of the corresponding compounds. To create high-resolution downcore profiles, values were averaged along single horizons with a minimum number of ten values set as a quality threshold (Wörmer et al., 2019). As laminae in the SBB subsample are slightly tilted due to subsampling from the box core, a tilt correction must be performed before averaging proxy value. This correction was achieved with an inverse spatial 2D transformation using *tforminv* in MATLAB 2016a (The MathWorks, Natick, USA) based on a minimum of four tie points per lamina set by visual identification of single laminae in the X-ray photograph (supplementary Fig. S1). A detailed description of the tilt correction and data processing can be found in Alfken et al., (submitted).

In consideration of the quality threshold (Wörmer et al., 2019), the high success rate of ~ 90% successful spectra for the $U_{37}^{K'}$ and CCaT allowed for a layer thickness of 200 µm, which correspond to 0.08 years (~monthly-resolution) in the time domain. The stanol to stenol ratio based on the saturated and monounsaturated C_{29} steroid alcohols was successful for ~ 60% of the spectra, allowing for broader resolution of 500 µm and 0.25 years.

The alkenone unsaturation index $U_{37}^{K'}$ is defined as described by Prahl et al. (1987) with the transformation into SST according to Prahl et al. (1988).

$$1. \quad U_{37}^{K'} = \frac{C_{37:2}}{C_{37:2} + C_{37:3}}$$

$$2. \quad U_{37}^{K'} = 0.034T + 0.039$$

The GDGT-based CCaT proxy was calculated according to Wörmer et al. (2014).

$$3. \quad CCaT = \frac{GDGT\text{-}5_{MS}}{GDGT\text{-}0 + GDGT\text{-}5_{MS}}$$

V.2.4. Lipid extraction and conventional biomarker analysis

In addition to MSI, 28 sediment samples were extracted according to a modified Bligh & Dyer protocol (Sturt et al., 2004b; Wörmer et al., 2015) for conventional biomarker analysis by liquid and gas chromatography coupled to mass spectrometry (LC-MS, GC-MS). Samples were extracted by ultrasonication using a solvent mixture of methanol (MeOH), dichloromethane (DCM) and aqueous buffer (2:1:0.8). The first two steps were performed using a phosphate buffer (8.7 g L^{-1} KH_2PO_4, pH 7,4), followed by two extraction steps with a trichloroacetic buffer (50 g L^{-1}, pH 2). After each step, supernatants were transferred to a separation funnel and subsequently separated into the organic and aqueous phase by addition of DCM and deionized MilliQ water. The organic phase was collected, and the water phase washed three more times with DCM, transferring the organic phase after each step. The pooled organic phase was washed three times

with deionized MilliQ water. The total lipid extract (TLE) was evaporated under a stream of nitrogen and stored at -20 °C.

Isoprenoidal GDGTs and alkenones were analyzed according to Becker et al (2015) using a Dionex Ultimate 3000RS UHPLC system coupled to a maXis Ultra-High Resolution quadrupole time-of-flight tandem mass spectrometer (qToF-MS; Bruker Daltonik, Bremen, Germany) equipped with an APCI-II ion source operating in positive mode. Chromatographic separation was achieved with two coupled Acquity BEH Amide columns (2.1 x 150 mm; 1.7 µm; Waters, Eschborn, Germany). Target compounds were identified based on exact m/z and characteristic retention times.

For the detection and identification of steroid alcohols via gas chromatography coupled to mass spectrometry (GC-MS), 50% of the TLE was treated with bis-(trimethylsilyl)trifluoroacetamide (BSTFA, Merck) in pyridine at 70 °C for 1.5 hours to form trimethylsilyl(TMS)-derivatives. Solvent and reagent were removed under a stream of nitrogen and the derivatized TLE was dissolved in 20 µL *n*-hexane. 2 µL were injected with an Agilent G4513A autosampler to an Agilent 7890A GC System equipped with a 30-m Restek Rxi-5MS fused silica capillary column (0.25 mm ID, 0.25 µm film thickness) coupled to a 5975C VL MSD with Triple-Axis detector (Agilent). The injection temperature of 60 °C was increased by 10 °C min^{-1} until 150 °C followed by a temperature ramp of 4 °C min^{-1} up to 320 °C. Steroid alcohols were identified according to their diagnostic mass spectrometric fragmentation pattern.

V.2.5. Frequency analysis

Spectral analysis was performed on the three climate indices (ENSO, PDO, NPGO) and three proxy record ($U^{K'}_{37}$, CCaT, stanol to stenol ratio) using the software PAST (version 3.22, Øyvind Hammer, Natural History Museum, University of Oslo). Wavelet transform was used for visualization of signals on different time scales throughout the time series and additional harmonic analysis was done with the REDFIT module. Power spectra were generated using a Hanning window with seven overlapping segments.

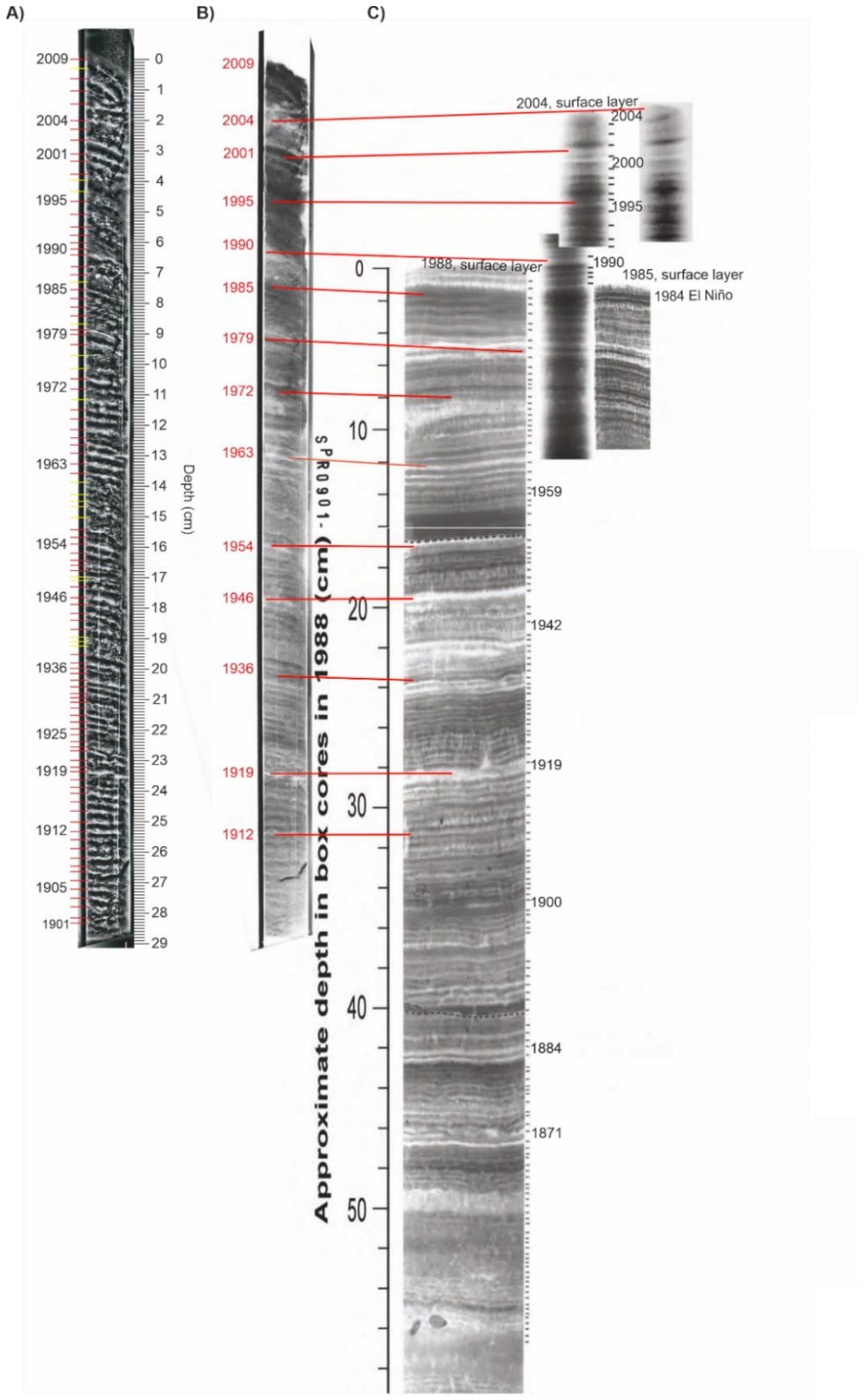

Fig.2: *Age model of SPR0901-05 BC. A) Contrast enhanced X-ray image of SPR0901-05BC with red lines showing varve counts and yellow lines showing indistinct varves, which were not counted but inferred based on linear interpolation B) original X-ray image, red lines identify prominent layers correlated to distinct marker layers in dated SBB cores (C) (Schimmelmann et al., 1990; Schimmelmann et al., 2013).*

V.3. Results and Discussion

V.3.1. Sea surface temperature reconstruction

The monthly-resolved $U^{K'}_{37}$ record reveals a total temperature range from 11.6 °C (1946) to 16.3 °C (1998). Compared to the ERSST, which has lowest values of 11.8 °C (1913) and highest of 20.0 °C (1998), the proxy-based temperatures exhibit a smaller range with cooler maxima. This smaller temperature range of the alkenone-based SST in the SBB can be attributed to a nutrient effect, as recently been shown by the first 25 years of this record (Alfken et al., submitted). This study showed an overall strong correlation of the $U^{K'}_{37}$ to the water temperature from the upper 30 m of the water column, i.e. the main habitat of the alkenone-producing haptophytes in SBB waters (Herbert et al., 1998), whereas the absolute amplitude of the proxy-based temperature was influenced by the nutrient concentrations in the haptophytes' habitat. Low nutrient supply as a result of reduced upwelling caused cooler than actual temperatures, whereas high nutrient concentrations led to warmer alkenone-based SSTs.

Whereas the lowest temperatures in these two records do not occur at the same time, the highest temperatures coincide with the strongest El Niño event of the past century in 1997/1998. Overall the $U^{K'}_{37}$ record mirrors the SST variations in the SBB expressed by the ERSST with corresponding minima and maxima throughout most of the record. Deviations between these two records can be attributed to the precision of the age model of ± 1 year, as well as the ERSST resolution of 2° in latitude and longitude leading to a representation of averaged SST around the broader SBB area.

The overall 20th century warming of ~1 °C until the 1997/1998 El Niño event and the subsequent cooling which has been observed along the southern Californian coast (Roemmich, 1992; Bograd and Lynn, 2003; Di Lorenzo et al., 2005) is also present in the ERSST record. For SST trend estimates we use the same approach as Di Lorenzo et al. (2005) and linearly fit a line to the time series and take the end values of the data for the period before and after the 1997/1998 El Niño (supplementary Fig. S4). The resulting warming trend of 1 °C in the ERSST is followed by a subtle cooling of 0.1 °C for the period after 1998. In the alkenone-based SST record this warming trend is almost imperceptible with an increase of only 0.2 °C, whereas the subsequent cooling of 1 °C is stronger The comparison of the MSI-based record with the $U^{K'}_{37}$ values obtained from extraction and HPLC/APCI-MS analysis shows a strong correspondence and no divergent trends (supplementary Fig. S2). The imprecise recording of the warming by the $U^{K'}_{37}$ can be attributed to the standard error of the $U^{K'}_{37}$ temperature calibration (± 1 °C; Prahl et al., 1988; Müller et al., 1998), which includes the range of the observed and reconstructed SST trends in the CCS. Another

cause of the indistinct warming in the $U_{37}^{K'}$ temperatures could be linked to the reported increase in stratification and deepening of the thermocline and nutricline in the CCS since the mid 1970´s (Roemmich and McGowan, 1995; Bograd and Lynn, 2003; McGowan et al., 2003; Palacios et al., 2004; Di Lorenzo et al., 2005), which led to a reduction in upwelling efficiency and reduced nutrient supply in surface waters (Di Lorenzo et al., 2005). Since the $U_{37}^{K'}$ temperature signal is dampened by the nutrient supply in the haptophytes' habitat (Prahl et al., 2003; Alfken et al., submitted), with the effect that lower nutrients result in colder reconstructed temperatures and *vice versa*, the absent overall warming trend, as well as the stronger subsequent cooling in the sedimentary $U_{37}^{K'}$ signal could be attributed to this nutrient effect.

V.3.2. Sea surface temperature and ENSO

SST variations in the CCS are influenced by the large-scale interannual climate phenomena ENSO. ENSO is most prominent in the tropical Pacific, with recurring fluctuation between warm (El Niño) and cold (La Niña) conditions every 2 to 7 years (McPhaden et al., 2006). During an El Niño event the thermocline in the CCS deepens, temperatures of the mixed layer become warmer and the southward transport of the California Current decreases leading to a reduction in upwelling. During a La Niña event, these effects are reversed, with colder SSTs, stronger upwelling and a strengthening of the California Current (e.g., Emery and Hamilton, 1985; Simpson, 1992; Lynn et al., 1995). ENSO events in the CCS usually lag behind the tropical Pacific by several months (Bograd and Lynn, 2001; Venrick et al., 2006) and not every equatorial El Niño is affecting the CCS (summarized by Venrick, 2012). Indeed, a recent study by Fiedler et al., (2017) showed that since 1950 only half of the warm events in the CCS coincide with an El Niño and that several El Niños had no warming effect on the CCS. The correspondence between cold events and tropical La Niñas on the other hand was more robust and displayed that all La Niñas resulted in cold temperatures in the CCS, whereas only three out of ten cold events were not related to La Niña.

Figure 3A shows the Niño 3.4 index for the time covered in this study (AD 1900 – 2009) with 13 moderate to strong La Niña events highlighted for negative temperature anomalies of ≥ 0.5 °C for at least five consecutive months in the annual running average. Events that were separated by up to two months are marked as one event (e.g. 1974 – 1976).

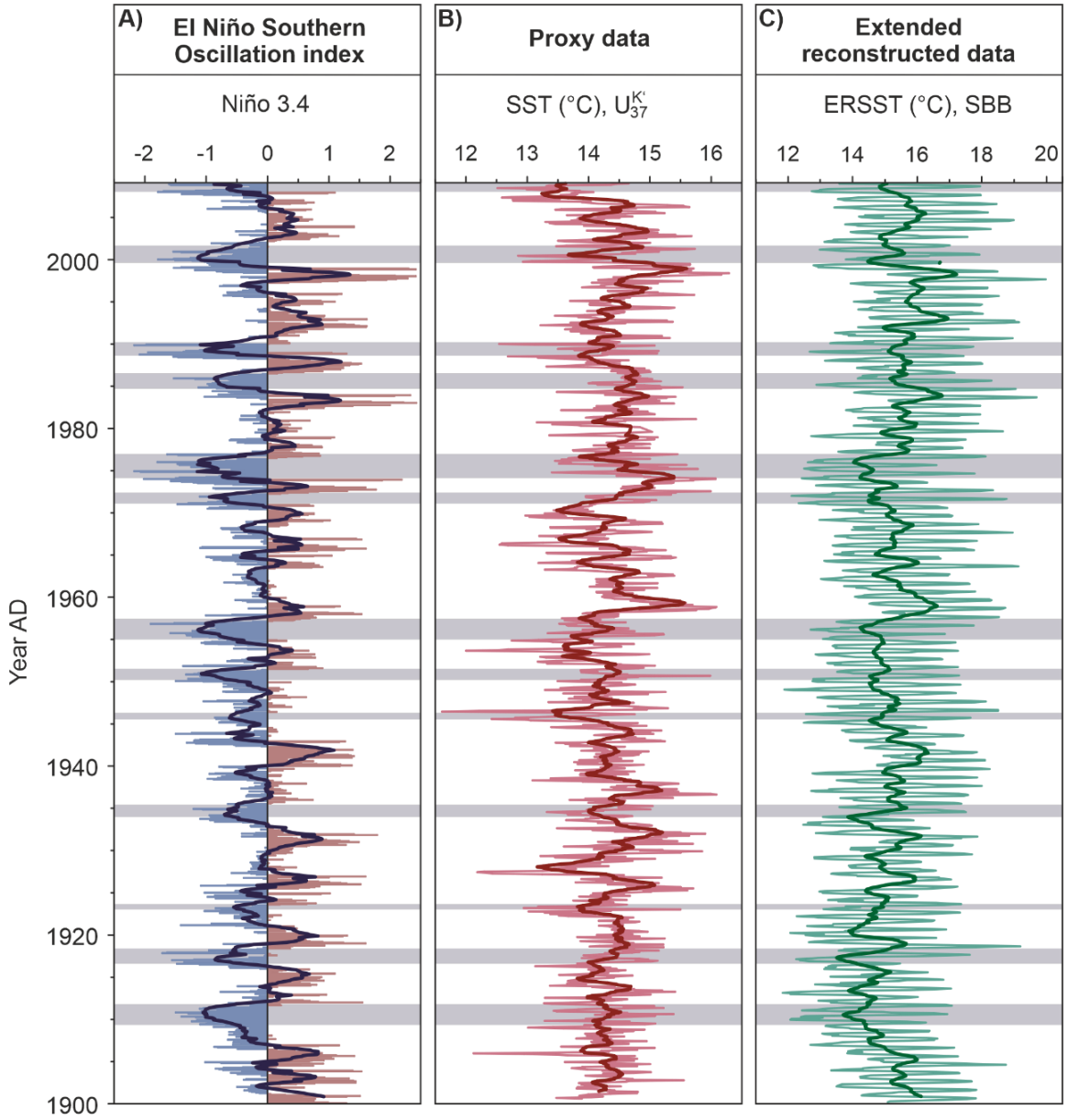

Fig.3: *SST variation in the SBB. MSI-based $U_{37}^{K'}$ SST (B) in comparison to ERSST (C) and Niño 3.4 index (A). All datasets are shown at monthly resolution with annual (12 point) running averages (thick lines). Horizontal grey bars highlight La Niña events with a temperature anomaly of 0.5 °C or more for five consecutive months in the annual running average of the Niño 3.4 record.*

The comparison of the monthly-resolved $U_{37}^{K'}$ temperatures and the ERSST to the Niño 3.4 index generally agrees with the above-mentioned findings of cold temperatures co-occurring with strong La Niña events (Fig. 3). The ERSST exhibits cold phases during most of these events, except from the La Niña in 1923 and the very weakly expressed event in 1952. The $U_{37}^{K'}$ records 9 out of the 13 La Niña events with a cooling. The two oldest events around 1910 and 1918, as well as the 1952 and 1986 La Niñas are not clearly recorded by the proxy record. The latter two also only show a minor cooling in the ERSST compared to the strength in the Niño 3.4 index. One prominent cooling around 1927 is only visible in the alkenone-based record.

The results of the frequency analyses of the $U^{K'}_{37}$ record confirm the correspondence of the alkenone-based SST reconstruction with ENSO variability (Fig. 4). In addition to the annual SST cycle, the $U^{K'}_{37}$ reveals significant frequencies resembling the ENSO frequencies. Whether the few mismatches between the ERSST and $U^{K'}_{37}$, as well as with the Niño 3.4 index are induced by the proxy itself or can be attributed to local oceanographic conditions in the SBB cannot be deciphered in this study. Overall the $U^{K'}_{37}$ can be seen as a confident proxy to record major ENSO, especially La Niña events in the SBB.

V.3.3. Low-frequency upwelling variability

Whereas SST and its variations on interannual time-scales in the SBB are recorded by the $U^{K'}_{37}$, the CCaT proxy, representative of the cyclization degree in isoprenoidal GDGTs, has shown to be a sensitive recorder of multi-year fluctuation in subsurface oxygen, salinity and nutrient concentrations in the SBB (Alfken et al., submitted). The ~110-year MSI-derived CCaT record (Fig. 5) shows a very different pattern compared to the SST variations in the SBB, with pronounced minima and maxima lasting for several years. This supports the previous findings from the direct comparison of the most recent 25 years of this record with seasonal instrumental data of the overlying water column in the SBB, which showed that this pattern most certainly derives from the nutrient availability in the subsurface water column (Alfken et al., submitted). Even though the cyclization in thaumarchaeal GDGTs is sensitive to temperature variations (Wuchter et al., 2004; Elling et al., 2015) and used for reconstruction of SST (Schouten et al., 2002; Kim et al., 2010; Wörmer et al., 2014), recent results from culture experiments showed that the ammonia oxidation rate in response to nutrient availability strongly affects the degree of cyclization (Hurley et al., 2016; Evans et al., 2018). Hence, in the upwelling area of the SBB we use the CCaT ratio as an indicator for upwelling strength.

These interannual to decadal variations in upwelling strength and the resulting ecosystem changes in the CCS have been linked to the large-scale climate modes of ENSO (Lynn et al., 1997; Bograd and Lynn, 2001), PDO (Mantua et al., 1997; Chavez et al., 2003; Chhak and Di Lorenzo, 2007) and NPGO (Di Lorenzo et al., 2008; García-Reyes and Largier, 2010) variability. The frequency analysis of the proxy record and the three climate indices confirms that the CCaT captures significant frequencies similar to these large-scale climate fluctuations (Fig. 4): frequencies close to ENSO and PDO of about 4 years are dominant until ~1985, followed by longer frequencies between 6 to 16 years similar to the PDO and NPGO. Before 1950, the CCaT seems to reflect a mixed signal of ENSO and PDO, whereas the influence of the NPGO cannot be addressed, since this index is only available until 1950.

A clear association of the CCaT and thus the long-term variability in the upwelling signal in the SBB to one climate index is not possible. This is not surprising, as all three indices dominate different regions of the CCS. As already presented in the SST analysis of the SBB, not every tropical ENSO event is affecting the SBB region. Indeed, for the CCS it has been shown that the overall ENSO influence is decreasing poleward, though it still has a dominant effect at 31°N (Lluch-Cota et al., 2001). The upwelling variability south of 38°N on the other hand is strongly correlated with the NPGO (Di Lorenzo et al., 2008), whereas the correlation with the PDO becomes stronger farther north (Chhak and Di Lorenzo, 2007; Di Lorenzo et al., 2008). Consequently, the SBB is located in a region where all three indices have an overlapping influence. The semi-closed structure of the SBB and the resulting local effects on the current structure can additionally modify the upwelling variability and thus be accounted for differences in the CCaT proxy and the climate indices.

The overall decreasing trend of the CCaT record is suggestive of an intensification in upwelling strength. This is consistent with observations and modelling results from the CCS showing an increase in upwelling-favorable winds within 50 – 100 km of the coast, as a result of intensified alongshore winds in response to warming ocean temperatures (Bakun, 1990; Schwing and Mendelssohn, 1997; Di Lorenzo et al., 2005; García-Reyes and Largier, 2010). The concurrent lower nutrient supply in the surface waters due to a deepening of the thermocline and intensification in stratification (Roemmich and McGowan, 1995; Bograd and Lynn, 2003; McGowan et al., 2003; Palacios et al., 2004; Di Lorenzo et al., 2005) is not captured by the CCaT signal, as this would generally result in higher CCaT values. This can be attributed to the main habitat depth of the GDGT-producing Thaumarchaea, which have been detected in subsurface depths below the mixed layer (Massana et al., 1997; Murray et al., 1999) and would thus not be affected by the lower nutrient supply in the surface water.

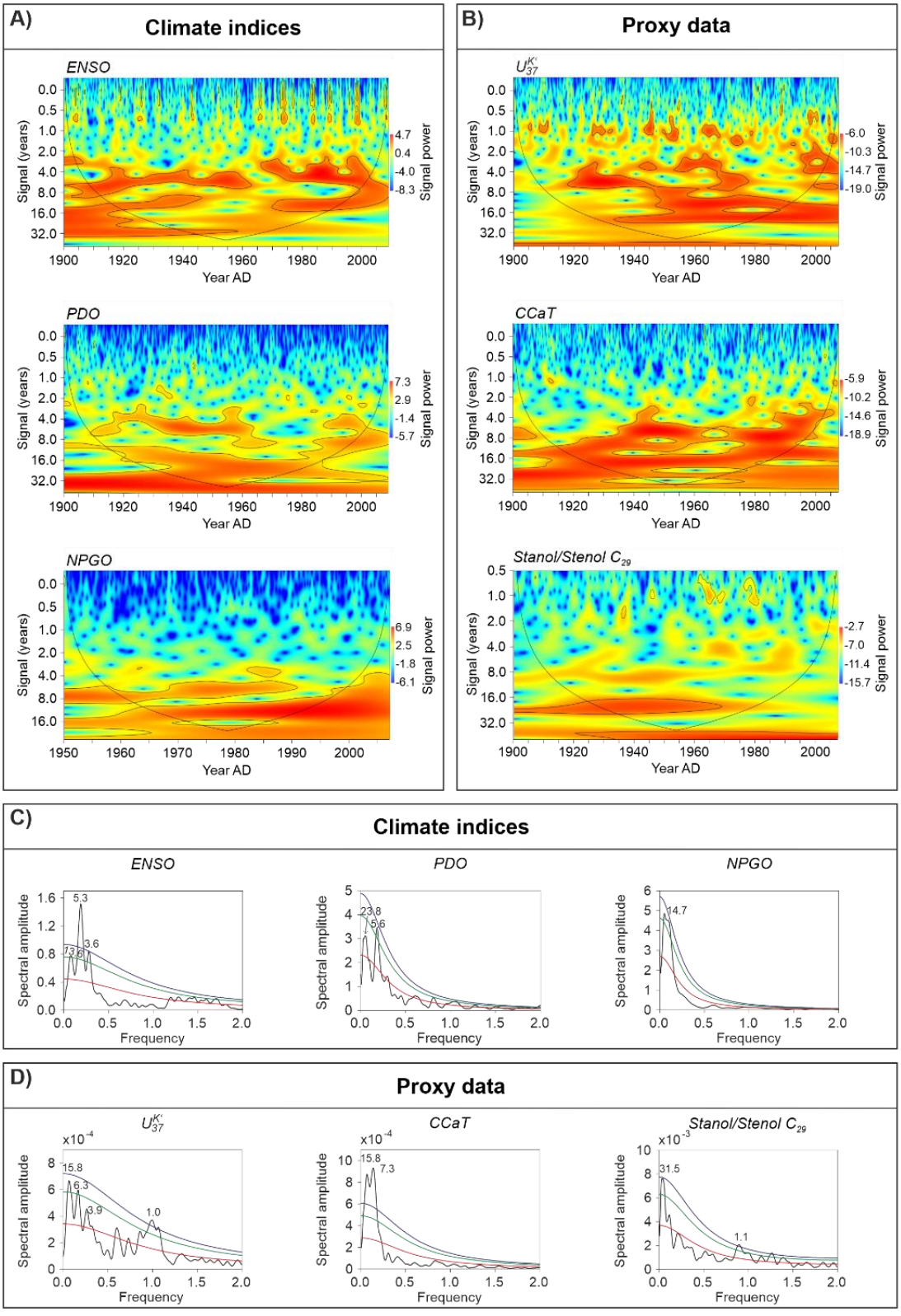

***Fig. 4**: Frequency analysis of climate indices and high-resolution proxy data. Wavelet transform are shown in panels A and B, and harmonic analysis using REDFIT in C and D. Thin black lines in the wavelet transforms show the cone of influence and dominant frequencies above the 95% significant level. Colored lines in C) and D) show red noise (red), 95% (green) and 99% (blue) significant levels Significant periodicities in years are labelled in the REDFIT analysis.*

V.3.4. Bottom water redox conditions

The 5α(H)-stanol/Δ5-stenol ratio is an organic geochemical proxy indicative of redox conditions. Increased 5α(H)-stanol/Δ5-stenol ratios at the oxic/anoxic boundary in the water column (Wakeham, 1989) and surface sediments (Nishimura and Koyama, 1977) occur through microbial conversion under anoxic conditions (Rosenfeld and Hellmann, 1971; Eyssen et al., 1973).

The stanol/stenol ratio based on the C_{29} saturated and mono-unsaturated steroid alcohols is accessible to MSI, even though a clear identification of the corresponding 5α(H)-stanol and Δ5-stenol pair is not possible by sole identification on exact *m*/*z* values. This is why a complementary analysis of lipid extracts via GC-MS is strongly recommended to assess possible influences on the MSI-derived stanol/stenol ratio by other isomers. The GC-MS results reveal that the 24-ethyl-5α(H)-cholestan-3β-ol to 24-ethylcholest-5-en-3β-ol is the most abundant C_{29} stanol-stenol pair, with only one additional stereoisomer of the monounsaturated C_{29} sterol, i.e. 4,24-Dimethylcholest-22-en-3β-ol, being present. The overall abundance of 4,24-Dimethylcholest-22-en-3β-ol is much lower compared to 24-ethylcholest-5-en-3β-ol. The comparison of the 24-ethyl-5α(H)-cholestan-3β-ol to 24-ethylcholest-5-en-3β-ol ratio with the C_{29} stanol/stenol ratio including 4,24-Dimethylcholest-22-en-3β-ol shows a strong correspondence (r^2 = 0.76; supplementary Fig. S3). Consequently, we assume that the C_{29} stanol/stenol ratio derived from MSI is primarily representing the 5α(H)-stanol/Δ5-stenol ratio. Additionally, the high-resolution MSI-based downcore profile of the C_{29} stanol/stenol ratio and the GC-MS derived values reveal a good alignment, which consolidates the use of this ratio as an indicator for redox conditions (supplementary Fig. S2).

The MSI-based C_{29} stanol/stenol ratio varies between values of 0.33 and 0.73 with a high-frequency pattern embedded into prolonged minima and maxima in its annual running average (Fig 5). Overall the C_{29} stanol/stenol ratio shows a decreasing trend after its maximum in 1966, which stabilizes into low values around 0.4 from ~1992 onwards. These decreasing values in the C_{29} stanol/stenol ratio are indicative of a higher redox potential associated to more oxygen availability in SBB bottom waters. Compared to other studies, the declining values from the mid-1960 until ~1990 are in agreement with sedimentary $\delta^{15}N$ from the Southern California Bight (Deutsch et al., 2014), whereas the low values after ~1992 are contrary to the increasing trends in $\delta^{15}N$ and the observation of an oxygen decline in the CCS (Bograd et al., 2008; Deutsch et al., 2014; Davis et al., 2019).

This discrepancy might be attributed to the suboxic bottom water conditions in the SBB. The initial study of 5α(H)-stanol/Δ5-stenol ratios in the water column of the Black Sea (Wakeham,

1989) showed an increase in 5α(H)-stanol/Δ^5-stenol ratios with decreasing dissolved oxygen and highest values at or just below the redox boundary when hydrogen sulfides (H_2S) strongly increased. In the SBB, this redox boundary does not occur in the bottom water as H_2S is not detectable within the upper ~5 cm of the sediment (Reimers et al., 1990). Assuming that the suboxic bottom water conditions generally result in a preferential degradation of Δ^5-stenols to 5α(H)-stanol, this ratio is capable of mirroring variations in the redox-potential of the SBB bottom waters. Nevertheless, with the O_2/H_2S interface occurring within the upper ~5 cm of the sediment, the absolute values of the C_{29} stanol/stenol ratio may further increase, potentially facilitated by the reducing power of inorganic sulfur species (Hebting et al., 2006). Whether this effect actually is responsible for the divergent low values since ~1992 needs to be assessed with a more recent sediment core, where the observed decrease in dissolved oxygen since ~1990 is archived below the upper 5 cm sedimentary record.

On shorter time-scales, changes in the oxygenation of SBB bottom water can occur due to the occasional flushing with dense and oxygenated water, which enters the basin over its western sill by strong seasonal upwelling during winter and spring north off Point Conception (Reimers et al., 1990; Bograd et al., 2002; Goericke et al., 2015). These flushing events usually lead to a mixing of the existing water and not to a complete oxygenation of the bottom water (Goericke et al., 2015). In the high-resolution C_{29} Stanol/Stenol record, this seasonal variability in bottom water oxygenation might be expressed in its high-frequency variability as well as the significant annual frequency of the time-series (Fig. 4D).

V.3.5. Varying effects of upwelling-induced changes in the redox conditions

Overall the C_{29} stanol/stenol ratio exhibits a pattern similar to the CCaT proxy with minima and maxima lasting for several years (Fig. 5). Indeed, for most of the record and until ~1970 it strongly resembles the CCaT. After this, the two proxies show a reversed pattern with CCaT minima coinciding with C_{29} stanol/stenol maxima. Displaying this relation in a correlation between the detrended annual running averages before and after 1970, reveals a positive correlation ($R = 0.32$; $p \leq 0.05$) for the time before 1970, whereas the more recent times are negatively correlated ($R = -0.46$; $p \leq 0.05$; Fig. 5).

As the CCaT is indicative of the low-frequency upwelling variability in the SBB, the observed relation to the C_{29} stanol/stenol ratio potentially shows a link between upwelling and redox potential associated to the oxygenation of the bottom water in the SBB. Until ~1970, years of upwelling (minima in CCaT) and intensified southward flow of the California Current led to mixing and ventilation of SBB waters and consequently to more oxygenated bottom water as expressed in low C_{29} stanol/stenol values. High CCaT values and thus reduced upwelling strength

would increase the stratification of the water column leading to persistent low oxygen concentrations in the bottom water due to the restricted ventilation and remineralization of organic matter.

After ~1970 this pattern reverses and times of strong upwelling coincide with lower bottom water oxygen content. Interestingly, the timing of this pattern shift is very close to the reported changes in the CCS in the mid-1970s, which have been linked to the PDO shift from its cold into its warm phase in 1976-1977. Changes included warming SSTs, an increase in stratification and deepening of the thermocline, as well as a decrease in the upwelling efficiency (Roemmich and McGowan, 1995; Bograd and Lynn, 2003; McGowan et al., 2003; Palacios et al., 2004; Di Lorenzo et al., 2005). In SBB sediments this change has been reported slightly earlier around 1972/1973, and thus closer to the one observed in this study (Lange et al., 1990). These authors observed a large decrease in the diatom flux, which they also associated to an overall reduction of mixing due to a weakening of the California Current.

Considering these observations, the inverse relationship between CCaT and C_{29} stanol/stenol ratio after ~1970 potentially reflects this general regime shift in the CCS. After this shift the oxygen content in SBB bottom water might be more affected by the upwelling-induced increase in primary productivity and the subsequent remineralization of organic matter. Times of strong upwelling no longer result in a mixing and ventilation of the water column. Even though the upwelling efficiency is lower, it is still accompanied by a higher nutrient supply compared to years of low upwelling strength. Thus, higher amounts of organic matter are produced, enhancing the remineralization of organic matter and consequently increasing the oxygen consumption in the bottom water, leading to an overall reduction in the redox potential.

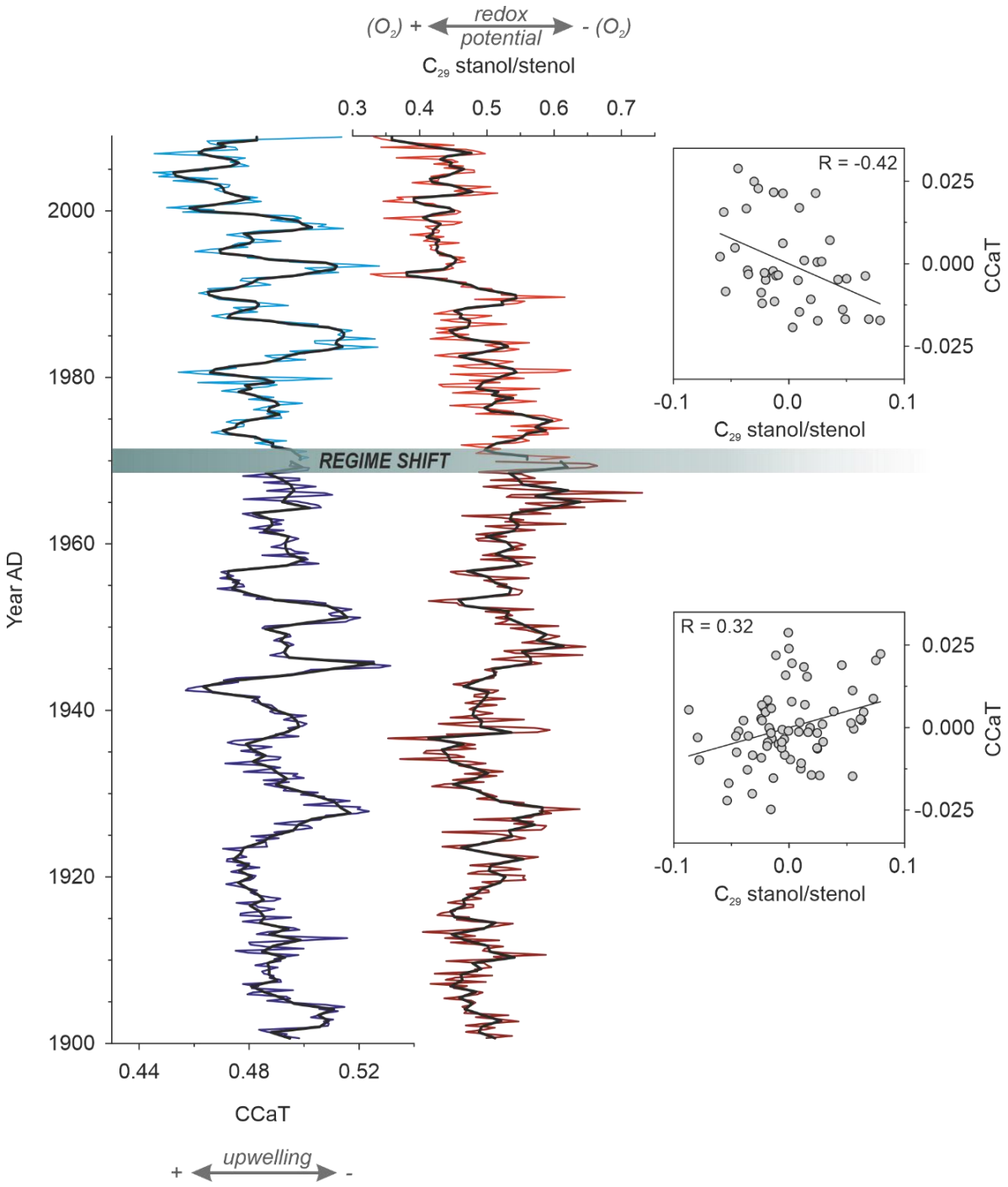

Fig. 5: *Interdependency between upwelling strength and bottom water redox conditions.MSI-derived records of CCaT (blue) and C_{29} stanol/stenol ratio (red) with annual running averages in black. Correlations between linearly detrended annual running averages before and after 1970 are shown by the crossplots ($p<0.05$).*

V.4. Summary and conclusion

This high-resolution, multiproxy analysis of the ~30 cm SBB box core *via* MSI revealed detailed insights into the dynamics and interactions of SST, upwelling, and redox conditions in the SBB from AD 1900 – 2009.

The monthly-resolved $U^{K'}_{37}$ reliably reflects SST variation and its modulation by ENSO events which affect the southern CCS region. However, the previously reported 20th century temperature increase of ~1 °C is not captured by the proxy. Even though this discrepancy could be attributed to the limitations of the temperature calibration, it can also be an effect of the long-term decrease in upwelling efficiency in the CCS. The related reduction of vertical transport of nutrient-rich waters to the ocean surface can affect the $U^{K'}_{37}$-based SST reconstruction, which has shown to be biased towards colder SST in respect to lower nutrient concentrations.

The upwelling-sensitive CCaT records multi-year upwelling variability in subsurface waters and an intensification of the upwelling strength in agreement with stronger upwelling-favorable winds in response to warming temperatures in the CCS. The low-frequency upwelling signal in the SBB region can described by a composite signal of ENSO, PDO and NPGO.

Changes in bottom water redox conditions were reconstructed using the C_{29} stanol/stenol ratio. The existing oxygen decline since the end of the past century cannot be reconstructed with this proxy. As the oxic/anoxic boundary occurs within the upper few centimeter of the sediment, corresponding to the timing of the oxygen decline, this discrepancy can be potentially associated to secondary processes of proxy alteration. A more recent sediment core would be needed to elucidate this effect.

The C_{29} stanol/stenol revealed that long-term changes in the bottom water oxygen content are linked to variations of the low-frequency upwelling. Until ~1970 upwelling, expressed by the CCaT proxy, and the C_{29} stanol/stenol are positively correlated, leading to the conclusion that bottom water oxygen concentrations are affected by upwelling-induced mixing and ventilation. After ~1970 this pattern is reversed leading to the assumption that the mid-1970s regime shift in the CCS and its related increase in stratification and deepening of the thermocline affects this relationship. Thus, after this regime shift the redox potential in SBB bottom waters is primarily controlled by changes in oxygen consumption in response to remineralization of organic matter.

Article info

Raw and processed data will be available on PANGAEA once the manuscript is accepted.

V.5. Supplementary information

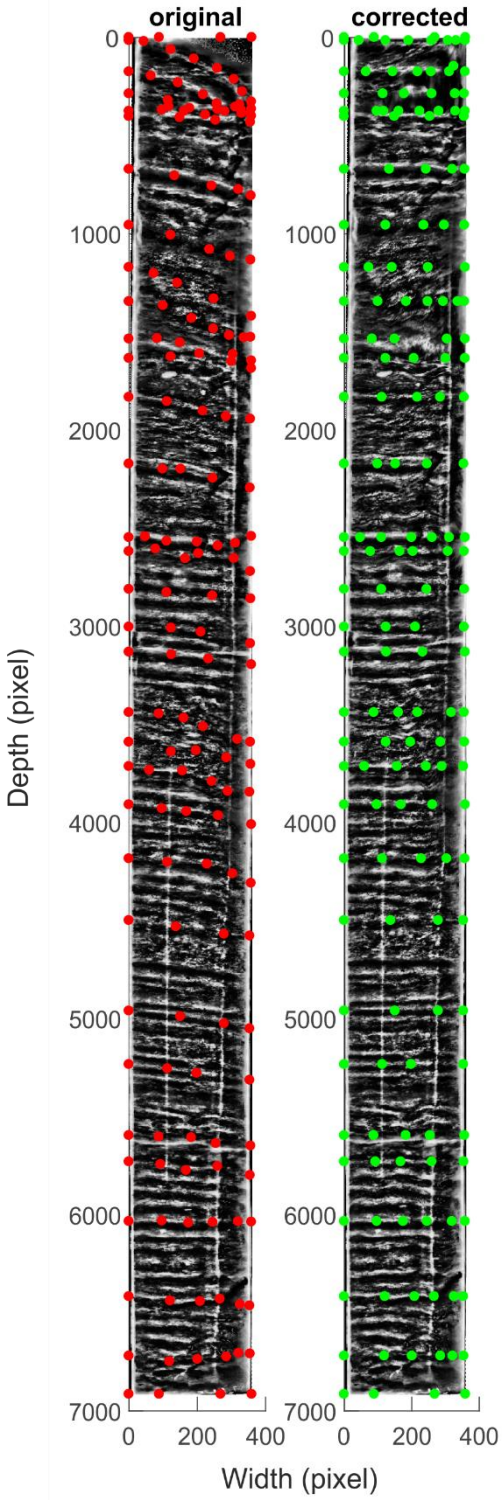

Fig. S1. *Correction of tilted laminae in SBB box core SPR0901-05BC. Left panel shows the contrast-enhanced original X-ray image with coeval layers labelled with at least 4 tie points (red). The corrected X-ray image with transformed horizontal laminae (green) is shown on the right. Piecewise linear transformation was performed using a slightly modified tforminv function in MATLAB 2016a (The MathWorks, Natick, USA). See Alfken et al., (submitted) for a more detailed description.*

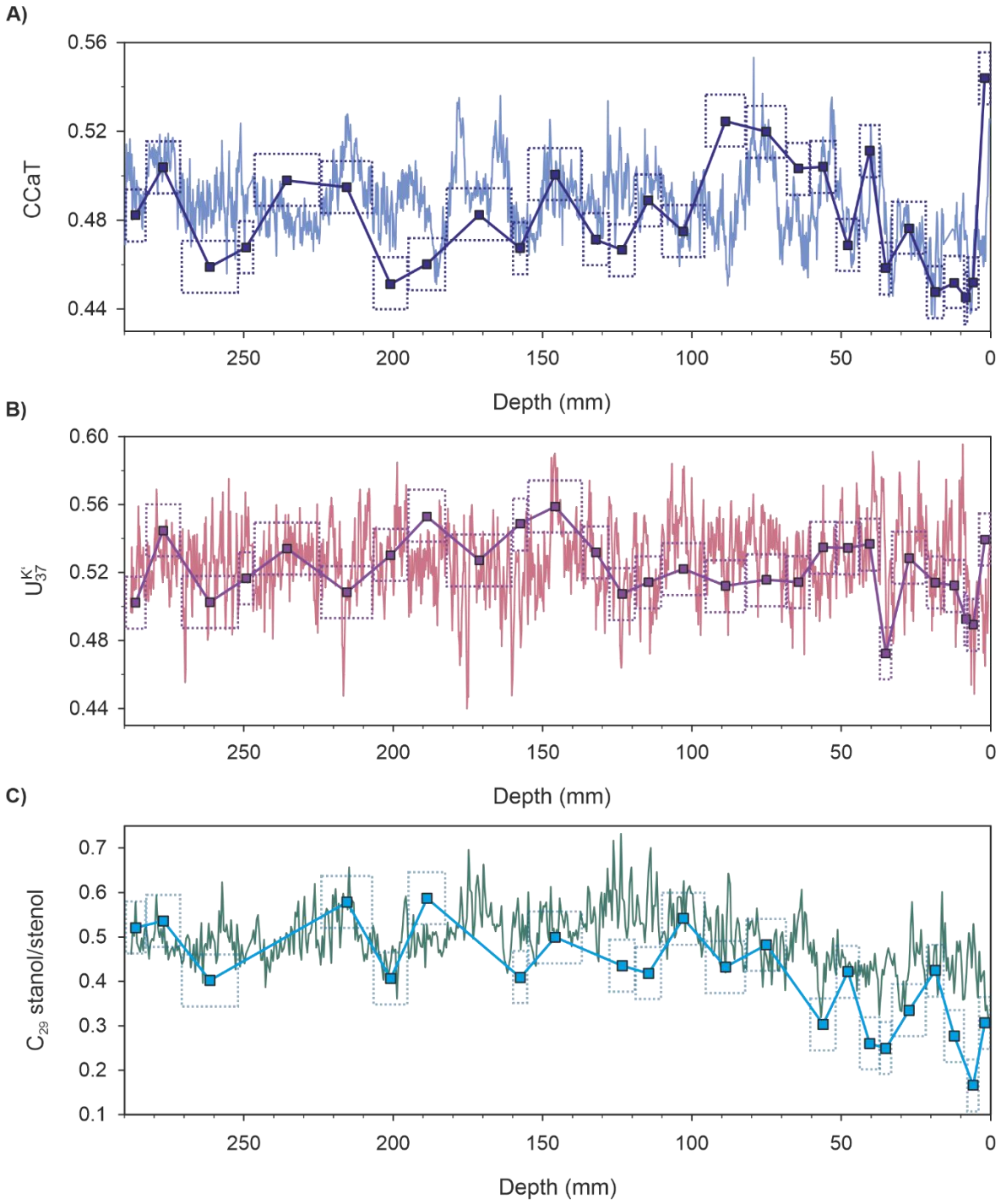

Fig. S2: *Comparison MSI-based and conventional, extraction-based data of CCaT (A), $U^{K'}_{37}$ (B) and the C_{29} stanol/stenol ratio (C). CCaT and $U^{K'}_{37}$ are shown at a 200 µm resolution and extraction-based results were obtained by HPLC/APCI-MS. The C_{29} stanol/stenol ratio is shown at 500 µm resolution due to a lower success rate in spectra generated by MALDI-FT-ICR-MS. Its complementary analysis of extracts was performed via GC-MS. Dotted rectangles indicate the corresponding depth range averaged for one sample used for extraction. The C_{29} stanol/stenol ratio was only detectable in 22 out of 28 extracted samples.*

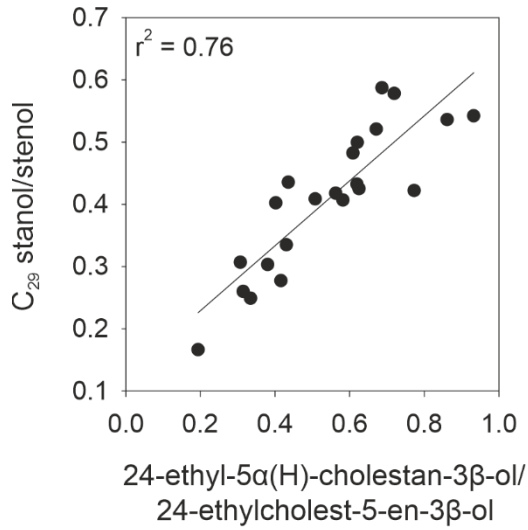

Fig. S3. *Comparison of the GC-MS-based C_{29} stanol/stenol ratios derived from 24-ethyl-5α(H)-cholestan-3β-ol and 24-ethylcholest-5-en-3β-ol (x-axis) with the C_{29} stanol/stenol ratio including 4,24-Dimethylcholest-22-en-3β-ol (y-axis).*

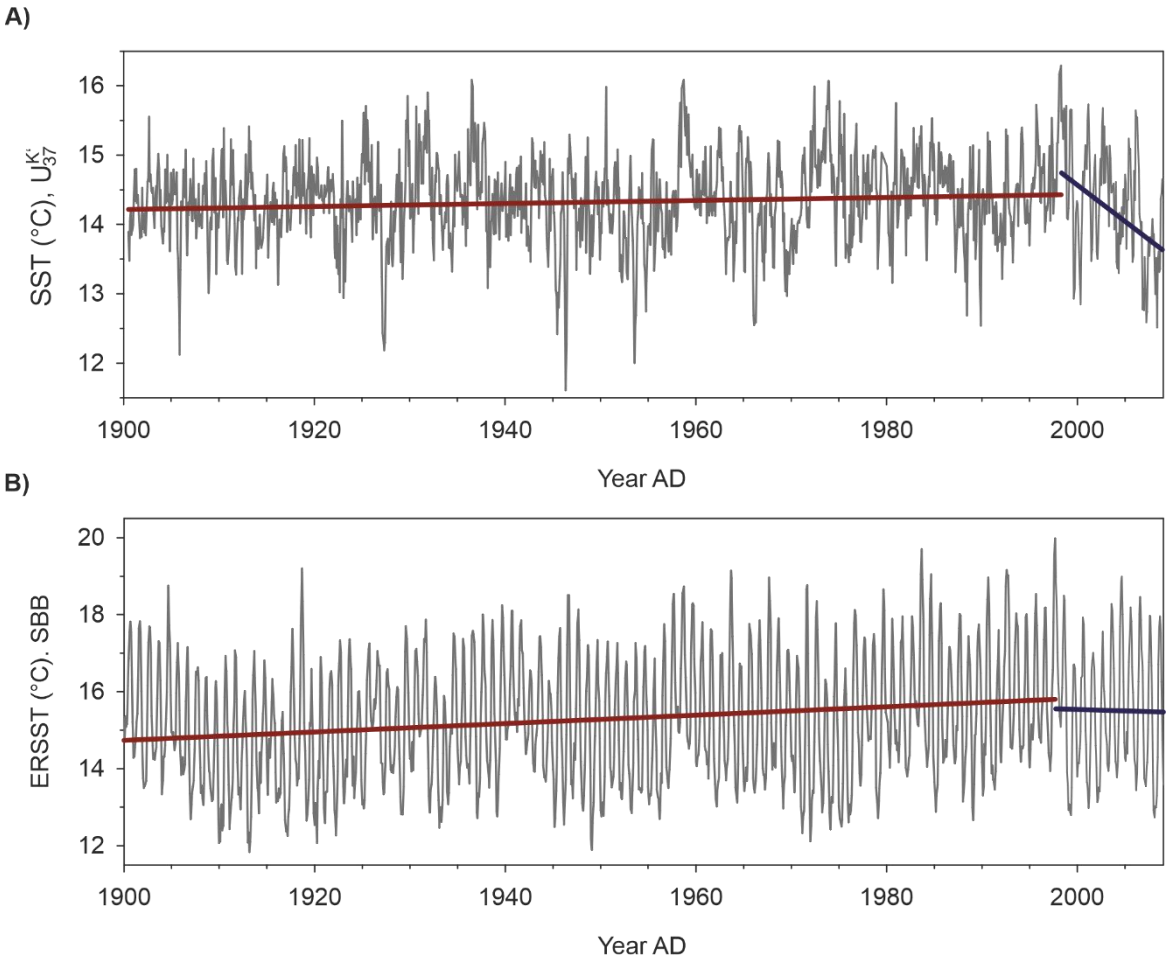

Fig. S4*: Temperature trends in $U^{K'}_{37}$-based SST (A) and ERSST record (B). Trends were defined by linearly fitting a line to the time series before (dark red) and after the temperature maximum 1997/1998 during El Niño (dark blue). This approach does not distinguish significant trends in SST and is only used to indicate the overall transition towards warmer temperatures throughout the 20th century (Di Lorenzo et al., 2005). The $U^{K'}_{37}$ shows warming of 0.2 °C and subsequent cooling of 1 °C. The ERSST has an increase of 1 °C and a cooling of 0.1 °C.*

CHAPTER VI

CONCLUDING REMARKS AND FUTURE PERSPECTIVES

Exploring past climate fluctuations *via* molecular stratigraphy provides insights into the temporal dynamics and response of ecosystems to climate change. However, the dependency of conventional extraction-based biomarker analysis on a relatively high sample amount limits the temporal resolution in paleo studies to decades or longer. Consequently, environmental transitions in response to abrupt events or natural interannual oscillations can hardly be addressed and fade into an averaged signal.

This dissertation focused on the implementation of a new, extraction-free approach to molecular stratigraphy by mass spectrometry imaging (MSI) that allows to increase the spatial and temporal resolution to the micrometer and subannual scale (CHAPTER II, CHAPTER III). With this novel technique detailed insights into the drivers of lipid biomarker-derived proxies were gained by addressing the small-scale differences of the signal archived in the sedimentary record (CHAPTER IV). Together with the improved understanding of the proxy signal, application of MSI to varved sediments from the Santa Barbara Basin, off Southern California revealed insights into the dynamics and interdependencies of ocean surface temperatures, upwelling strength and bottom water oxygen content during the 20th century (CHAPTER V).

Implementation of mass spectrometry imaging as a tool for molecular stratigraphy

MSI enables visualization of the micrometer-sized spatial distribution of target analytes on a sample surface. Applied to sediments, this technique holds enormous potential for high-resolution paleoclimatology and at the same time presents great challenges regarding its implementation.

In CHAPTER II I established a routine protocol for the ideal sample preparation of marine sediment samples for the sequential analysis of lipid biomarkers by MALDI-FT-ICR-MS, with a focus on archaeal tetraether lipids. Sample preparation involves freeze-drying of the intact sediment to avoid dimensional alteration, the subsequent stabilization in MSI-compatible embedding media and sectioning into micrometer-thin sequential slices ideally suited for MSI. Besides lipid biomarker analysis, this protocol includes the option of a complementary elemental mapping to provide information on depositional settings and the interdependence between lipid biomarkers and the sedimentary matrix. With the developed protocol signal intensities were improved, and multiproxy and replicate analyses were enabled.

To exploit the full potential of MSI for molecular stratigraphy, the set of sedimentary biomarkers amenable by this technique was extended and guidelines for laser-based multiproxy paleoclimatology were defined in CHAPTER III. This chapter shows that concentration of the target compounds is strongly determining its successful ionization and analytical quality. Whereas ionization of compounds in biological tissues usually relies on the addition of artificial matrices, no matrix or rather unconventional ones like silver nitrate or graphite were needed for sediment MSI. Together CHAPTER II and CHAPTER III set the stage for MSI-based high-resolution paleoclimate studies.

New insights into drivers of proxy information

The unprecedented high temporal resolution given by MSI allows for new mechanistic insights into the factors shaping the molecular proxy signal archived in the sedimentary record. In CHAPTER IV, monthly-resolved records of two SST proxies were obtained with MALDI-FT-ICR-MS from varved SBB sediments and were directly compared to 25 years of seasonally measured water column characteristics. Even though both proxies, i.e. $U^{K'}_{37}$ from the unsaturation of long-chain alkenones in haptophyte algae and CCaT representative of the cyclization in core GDGTs from planktonic Thaumarchaeota, exhibit strong correlations to mean annual SST, influences of the physiological response to other water properties have previously been observed in culture experiments. The results presented in CHAPTER IV of my thesis emphasize the strength of the $U^{K'}_{37}$ proxy to capture the annual SST cycle and simultaneously show, for the first time in a sedimentary

record, that the temperature amplitude is affected by a physiological response to nutrient availability in the haptophytes' habitat. This finding implies that the effect of nutrients on the archived $U_{37}^{K'}$ signal should be carefully considered in paleoenvironmental reconstructions, especially when there is evidence of dynamical nutrient supply.

The MSI-based signal of the CCaT record reveals a completely different signal compared to the $U_{37}^{K'}$. The CCaT exhibits correlation with subsurface nutrient, oxygen and salinity concentrations, which are controlled by interannual, basin-wide variations in upwelling intensity. As physiological responses to salinity and oxygen cannot explain the observed CCaT variations, we conclude that its signal is strongly dependent on upwelling-induced nutrient availability. Consequently, in an upwelling system such as the SBB, the sedimentary CCaT signal can be seen as a proxy for subsurface variations in upwelling strength.

Interdependency of ocean warming, upwelling strength and bottom water redox conditions in the southern California current system

Given the new insights on proxy interpretation obtained from CHAPTER IV and the widened set of lipid biomarkers amenable to MSI described in CHAPTER III, in CHAPTER V we investigated the temporal dynamics of SST, upwelling strength and bottom water redox conditions in the SBB region in a subannual resolved 110-year multiproxy record.

SST variations and its modulation by the large-scale climate phenomenon ENSO was confidently recorded by the $U_{37}^{K'}$ during the 20th century. However, the reported ~1 °C warming trend in the CCS could not be detected by this proxy, a fact that can be attributed to the nutrient effect observed in CHAPTER IV. Ocean warming in the CCS would increase stratification and result in a decrease in upwelling efficiency and lower nutrient availability in the ocean surface. As lower nutrient supply shifts alkenone-based temperatures towards a cold bias the general warming trend is potentially underestimated by this proxy. Again, CHAPTER V together with the results from CHAPTER IV emphasize the careful consideration of the reliability of $U_{37}^{K'}$ derived SST, especially in systems with variable nutrient supply.

Long-term change in upwelling strength in the CCS is represented by the CCaT proxy, which shows an increasing trend in upwelling strength as a result of intensified alongshore winds in response to warming SST. Modification of this multi-year upwelling variability is linked to a composite signal of large-scale climate phenomena affecting the CCS, i.e. ENSO, PDO and NPGO.

The connection between upwelling strength and bottom water oxygen content and its changing pattern is shown by the relation between the CCaT and C_{29} stanol/stenol ratio. Before a

major change in the CCS, intensification of upwelling strength increased the oxygen content in SBB bottom water due to ventilation and vertical mixing. The increasing stratification and deepening of the thermocline associated to the mid-1970s regime shift also changed the effect of upwelling on the bottom water redox conditions. Ventilation is no longer affecting the oxygen content in SBB bottom waters, and a reversed pattern emerges suggesting that the upwelling-induced increase in productivity and the subsequent remineralization of organic matter becomes the driving force in bottom water redox conditions.

OUTLOOK

While the analysis of the ~30 cm SBB sediment core has revealed detailed insights into the variable oceanographic conditions in the southern CCS during the past century, the record did not cover the transition from pre-industrial times. Consequently, the effects of anthropogenic forcing on the SBB region and on the large-scale climate oscillations affecting this region were not addressed. Extending this study to the past ~2000 years will provide unique perspectives on the evolution of past oceanic properties and on their natural variability which are an essential requirement to evaluate their response to global warming. Whereas the intensity of the large-scale climate phenomenon ENSO has been variable throughout the past millennium (Cobb et al., 2003), most of the extreme ENSO events seem to be associated to the 20th century (Gergis and Fowler, 2009) and the occurrence of central Pacific El Niño events is predicted to become more frequent with global warming (Yeh et al., 2009). A MSI-based analysis of a longer SBB sediment record will provide valuable insights into the frequencies and intensity of SST and upwelling variability and the potential changes of ENSO-related influence through time.

Besides oceanographic changes, the variability of southern California hydroclimate and associated severe droughts and flooding events were also shown to be related to ENSO (Hendy et al., 2015; Napier et al., 2018). Controlled by this precipitation pattern wildfires strongly affect the SBB region and their occurrence has been potentially modified by active fire suppression during the 20th century (Minnich, 1983; Mensing et al., 1999). MSI-based analyses of biomarkers indicative of biomass burning such as PAHs or Levoglucosan (Simoneit, 2002; Lima et al., 2005) present great potential to reconstruct the past fire regime and to evaluate its connection to large-scale climate oscillation as well as the effect of fire suppression.

Whereas this dissertation focused on modern varved SBB sediments, other high-resolution marine and lacustrine archives are ideally suited for MSI-based molecular stratigraphy. Promising archives that are currently analyzed by this technique are, for example, the North Atlantic Cariaco Basin and the central European Meerfelder Maar, which both allow for the reconstruction of the abrupt and drastic environmental changes associated to the Younger Dryas

cooling period. Apart from paleoenvironmental reconstructions with proxies based on membrane core lipids, the approach of MSI yields the potential to generate images of molecular biomarkers that inform on the spatial distribution of living microbial communities and their interaction with the sedimentary matrix. Similarly, micrometer-scale visualization of these biomarkers can provide detailed insights into the fine zonation of e.g. microbial mats in response to strong physical or chemical gradients.

So far, sedimentary MSI is based on a targeted approach, i.e. defining ratios from the intensity of specific biomarkers ionized and detected by MALDI-FT-ICR-MS. Given the extremely high mass resolving power of FT-ICR-MS, this technique potentially allows for the untargeted molecular characterization of the ionized organic matter, similar to the characterization of dissolved organic matter. The statistical analysis of the micrometer-scale distribution of organic compounds in combination with an elemental mapping of the sedimentary matrix has the potential to provide new insights of the distribution, composition and degradation of organic matter in sedimentary archives.

CONTRIBUTIONS TO PUBLICATIONS

CHAPTER II

MICROMETER SCALE IMAGING OF SEDIMENTARY CLIMATE ARCHIVES – SAMPLE PREPARATION FOR COMBINED ELEMENTAL AND LIPID BIOMARKER ANALYSIS

Susanne Alfken, Lars Wörmer, Julius S. Lipp, Jenny Wendt, Heidi Taubner, Arndt Schimmelmann, Kai-Uwe Hinrichs

Published in O*rganic Geochemistry*, Vol. 127, pages 81-91.

Detailed author contributions

I designed the study with L.W. and K.-U.H. I performed the lab work with support from J.W. I performed MALDI-FT-ICR-MS measurements. Elemental data based on μ-XRF scanning were acquired by me with the help from H.T. Santa Barbara Basin sediments samples were provided by A.S. I analyzed and interpreted MALDI-FT-ICR-MS data with support from L.W. and J.S.L. I visualized results in figures and wrote the manuscript with significant input from L.W and K.-U.H. All authors commented on the manuscript.

CHAPTER III

TOWARDS MULTIPROXY, ULTRA-HIGH RESOLUTION MOLECULAR STRATIGRAPHY: ENABLING LASER-INDUCED MASS SPECTROMETRY IMAGING OF DIVERSE MOLECULAR BIOMARKERS IN SEDIMENTS

Lars Wörmer, Jenny Wendt, Susanne Alfken, Jin-Xiang Wang, Marcus Elvert, Verena B. Heuer, Kai-Uwe Hinrichs

Published in O*rganic Geochemistry*, Vol. 127, pages 136-145.

Detailed author contributions

L.W. and K.-U.H. designed this study. L.W., J.W., and J.-X.W. performed lab work and MALDI-FT-ICR-MS measurements of pure compounds and lipid extracts. L.W. and J.W. measured Mediterranean sapropel sediments with MALDI-FT-ICR-MS. I performed MALDI-FT-ICR-MS measurements of Santa Barbara Basin samples. L.W. analyzed and interpreted data from pure compounds, lipid extracts and Mediterranean sapropel. Data analysis and interpretation from Santa Barbara Basin samples was done by L.W. and me. L.W. visualized results from pure compounds, lipid extracts and Mediterranean sapropel. L.W. and I visualized results from Santa Barbara Basin samples. L.W. and K.-U.H. wrote the manuscript with contributions from all co-authors.

CHAPTER IV

NEW INSIGHTS INTO THE FACTORS SHAPING MOLECULAR PROXIES VIA SEASONALLY RESOLVED SEDIMENTARY RECORDS

Susanne Alfken, Lars Wörmer, Julius S. Lipp, Jenny Wendt, Arndt Schimmelmann, Kai-Uwe Hinrichs

Submitted to a peer-reviewed international journal

Detailed author contributions

I, K.-U.H., L.W. and A.S. designed research. I performed the lab work and measured samples with MALDI-FT-ICR-MS with support from J.W. A.S. provided Santa Barbara Basin samples. Age model was established by A.S. and me. I analyzed data with help from L.W. and J.S.L. I interpreted data with L.W. and K.-U.H. I visualized results in figures and wrote the manuscript together with K.-U.H. and significant input from L.W.; all authors commented on the manuscript.

CHAPTER V

A 110-YEAR MULTIPROXY RECORD OF OCEANOGRAPHIC VARIATION IN THE SANTA BARBARA BASIN, OFF SOUTHERN CALIFORNIA

In preparation for *Earth and Planetary Science Letters*

Susanne Alfken, Lars Wörmer, Julius S. Lipp, Marcus Elvert, Jenny Wendt, Arndt Schimmelmann, Kai-Uwe Hinrichs

Detailed author contributions

I designed the study with K.-U.H. and L.W. I measured samples with MALDI-FT-ICR-MS with support from J.W. A.S. provided Santa Barbara Basin samples. Age model was established by A.S. and me. I performed sample extraction and measurements with GC-MS. I analyzed MALDI-FT-ICR-MS data with help from L.W. and J.S.L. GC-MS data was analyzed by me with support from M.E. I interpreted data with L.W. and K.-U.H. I visualized results in figures and wrote the manuscript with input from L.W. and K.-U.H.

CONTRIBUTION AS CO-AUTHOR

Forcing mechanisms behind the time-transgressive Younger Dryas cooling across the North Atlantic realm

Igor Obreht[a*], Lars Wörmer[a], Achim Brauer[b, c], Jenny Wendt[a], Susanne Alfken[a], David De Vleeschouwer[d], Marcus Elvert[a], Kai-Uwe Hinrichs[a]

In review for *Nature Communications*

[a] Organic Geochemistry Group, MARUM – Center for Marine Environmental Sciences and Faculty of Geosciences, University of Bremen, Leobener Str. 8, 28359 Bremen, Germany

[b] GFZ – German Research Centre for Geosciences, Section Climate Dynamics and Landscape Evolution, Telegrafenberg, 14473 Potsdam, Germany

[c] Potsdam University, Department of Earth Sciences, Karl-Liebknecht-Str. 24/25, 14476 Potsdam, Germany

[c] Palaeoceanography group, MARUM – Center for Marine Environmental Sciences and Department of Geosciences, University of Bremen, Leobener Str. 8, 28359 Bremen, Germany

[*] Corresponding author: E-mail address: iobreht@marum.de

Abstract

The regional patterns and timing of the Younger Dryas cooling in the North Atlantic realm were complex and are mechanistically incompletely understood. To enhance our understanding of the underlying forcing mechanisms, we generated biomarker records at subannual to annual resolution by mass spectrometry imaging of sediments from the Lake Meerfelder Maar covering the Allerød-Younger Dryas transition. The targeted fatty acid biomarkers serve as a sensitive gauge of the response of local aquatic and terrestrial vegetation to climate change. Despite the delay of Western Europe cooling relative to abrupt Greenland cooling by ~135 years, biomarker data correlate with deuterium excess in Greenland ice core during this time-transgressive cooling, indicating a coherent atmospheric forcing across the North Atlantic realm. We suggest that Western European cooling was postponed by the impact of amplified sea-ice formation over the western North Atlantic on the westerlies, forcing lower latitude warmer and wetter air masses to reach Western Europe and preventing abrupt cooling.

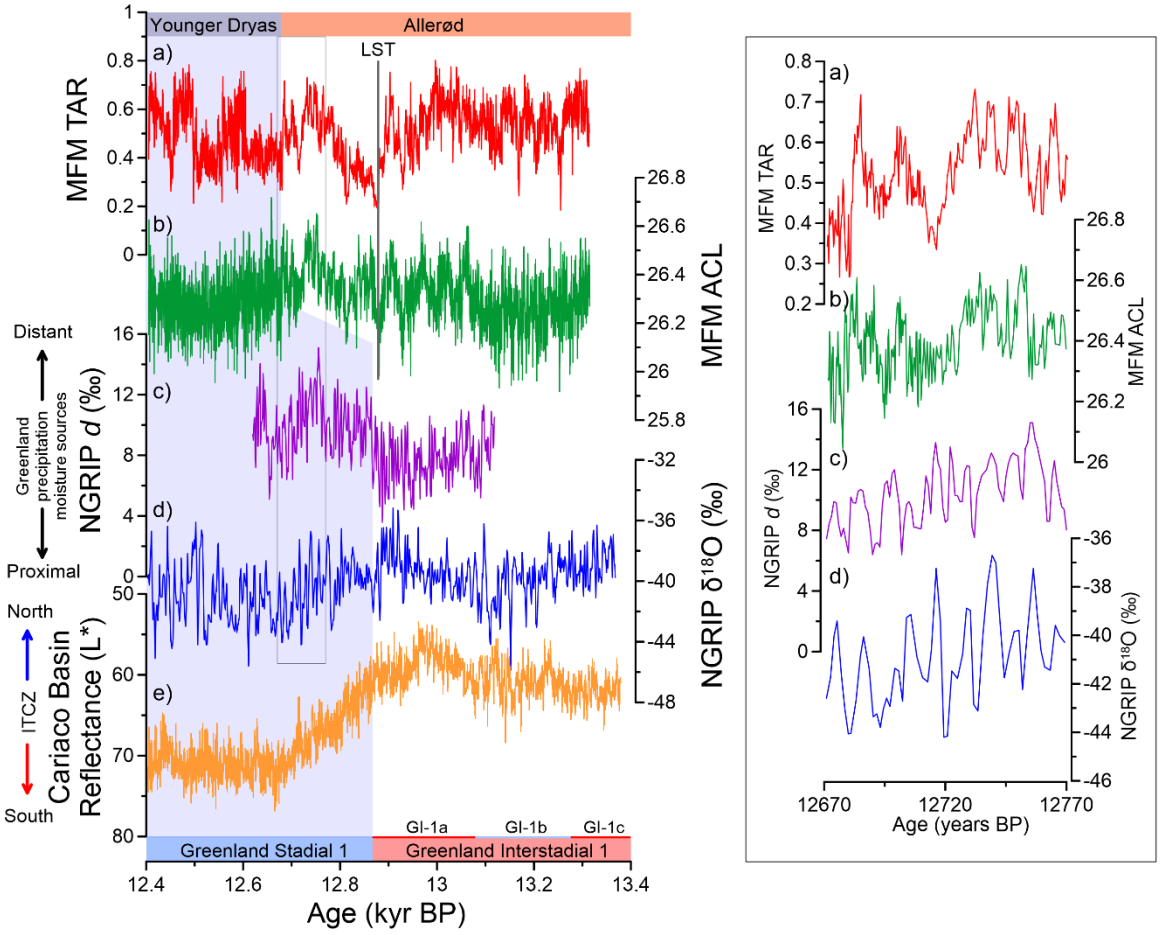

Comparison of Meerfelder Maar and North Greenland Ice Core Project (NGRIP). *a) From top: comparison of Meerfelder Maar Terrestrial to Aquatic Ratio (TAR; red line) and Average Chain Length (ACL; green line) from MSI-based fatty acid analysis with Na^+ d (purple line) and $\delta^{18}O$ (blue line) from NGRIP (Steffensen et al., 2008; Gkinis et al., 2014). Note that the NGRIP chronology is converted to the Meerfelder Maar chronology. Blue shaded areas indicate the onset of Greenland Stadial 1 in Greenland and the onset of the Younger Dryas in Western Europe. b) – zoom in the interval of time-transgressive onset of Greenland and Western Europe Younger Dryas cooling (indicated by a grey rectangle in the left panel).*

REFERENCES

ALFKEN, S., WÖRMER, L., LIPP, J.S., WENDT, J., TAUBNER, H., SCHIMMELMANN, A., HINRICHS, K.-U. (2019). Micrometer scale imaging of sedimentary climate archives–Sample preparation for combined elemental and lipid biomarker analysis. *Organic Geochemistry* **127**, 81–91. DOI: 10.1016/j.orggeochem.2018.11.002.

ALFKEN, S., WÖRMER, L., LIPP, J.S., WENDT, J., SCHIMMELMANN, A., HINRICHS, K.-U. (submitted). New insights into the factors shaping molecular proxies via seasonally resolved sedimentary records.

BAKUN, A. (1990). Global climate change and intensification of coastal ocean upwelling. *Science* **247** (4939), 198–201. DOI: 10.1126/science.247.4939.198.

BASSE, A., ZHU, C., VERSTEEGH, G.J.M., FISCHER, G., HINRICHS, K.-U., MOLLENHAUER, G. (2014). Distribution of intact and core tetraether lipids in water column profiles of suspended particulate matter off Cape Blanc, NW Africa. *Organic Geochemistry* **72**, 1–13. DOI: 10.1016/j.orggeochem.2014.04.007.

BAUMGARTNER, T.R., SOUTAR, A., FERREIRA-BARTRINA, V. (1992). Reconstruction of the history of the Pacific sardine and northern anchovy populations over the past two millenia from sediments of the Santa Barbara Basin, California. *California Cooperative Oceanic Fisheries Investigations Report* (33), 24–40.

BECKER, K.W., LIPP, J.S., VERSTEEGH, G.J.M., WÖRMER, L., HINRICHS, K.-U. (2015). Rapid and simultaneous analysis of three molecular sea surface temperature proxies and application to sediments from the Sea of Marmara. *Organic Geochemistry* **85**, 42–53. DOI: 10.1016/j.orggeochem.2015.04.008.

BIANCHI, T.S., ENGELHAUPT, E., WESTMAN, P., ANDRÉN, T., ROLFF, C., ELMGREN, R. (2000). Cyanobacterial blooms in the Baltic Sea: Natural or human-induced? *Limnology and Oceanography* **45** (3), 716–726. DOI: 10.4319/lo.2000.45.3.0716.

BIDDLE, J.F., LIPP, J.S., LEVER, M.A., LLOYD, K.G., SØRENSEN, K.B., ANDERSON, R., FREDRICKS, H.F., ELVERT, M., KELLY, T.J., SCHRAG, D.P. (2006). Heterotrophic Archaea dominate sedimentary subsurface ecosystems off Peru. *Proceedings of the National Academy of Sciences* **103** (10), 3846–3851. DOI: 10.1073/pnas.0600035103.

BIONDI, F., LANGE, C.B., HUGHES, M.K., BERGER, W.H. (1997). Inter-decadal signals during the last millennium (AD 1117–1992) in the varve record of Santa Barbara Basin, California. *Geophysical Research Letters* **24** (2), 193–196. DOI: 10.1029/96GL03813.

BOËS, X., FAGEL, N. (2005). Impregnation method for detecting annual laminations in sediment cores: An overview. *Sedimentary Geology* **179** (3–4), 185–194. DOI: 10.1016/j.sedgeo.2005.05.001.

BOETIUS, A., RAVENSCHLAG, K., SCHUBERT, C.J., RICKERT, D., WIDDEL, F., GIESEKE, A., AMANN, R., JØRGENSEN, B.B., WITTE, U., PFANNKUCHE, O. (2000). A marine microbial consortium apparently mediating anaerobic oxidation of methane. *Nature* **407** (6804), 623. DOI: 10.1038/35036572.

BOGRAD, S.J., CASTRO, C.G., DI LORENZO, E., PALACIOS, D.M., BAILEY, H., GILLY, W., CHAVEZ, F.P. (2008). Oxygen declines and the shoaling of the hypoxic boundary in the California Current. *Geophysical Research Letters* **35** (12), L12607. DOI: 10.1029/2008GL034185.

BOGRAD, S.J., LYNN, R.J. (2001). Physical-biological coupling in the California Current during the 1997–99 El Niño-La Niña Cycle. *Geophysical Research Letters* **28** (2), 275–278. DOI: 10.1029/2000GL012047.

BOGRAD, S.J., LYNN, R.J. (2003). Long-term variability in the Southern California Current System. *Deep Sea Research Part II: Topical Studies in Oceanography* **50** (14), 2355–2370. DOI: 10.1016/S0967-0645(03)00131-0.

BOGRAD, S.J., SCHWING, F.B., CASTRO, C.G., TIMOTHY, D.A. (2002). Bottom water renewal in the Santa Barbara Basin. *Journal of Geophysical Research: Oceans* **107** (C12), 9-1-9-9. DOI: 10.1029/2001JC001291.

BRASSELL, S.C., EGLINTON, G., MARLOWE, I.T., PFLAUMANN, U., SARNTHEIN, M. (1986). Molecular stratigraphy: a new tool for climatic assessment. *Nature* **320** (6058), 129–133. DOI: 10.1038/320129a0.

BRAUER, A., HAUG, G.H., DULSKI, P., SIGMAN, D.M., NEGENDANK, J.F.W. (2008). An abrupt wind shift in western Europe at the onset of the Younger Dryas cold period. *Nature Geoscience* **1** (8), 520–523. DOI: 10.1038/ngeo263.

BROCHIER-ARMANET, C., BOUSSAU, B., GRIBALDO, S., FORTERRE, P. (2008). Mesophilic Crenarchaeota: Proposal for a third archaeal phylum, the Thaumarchaeota. *Nature Reviews Microbiology* **6** (3), 245. DOI: 10.1038/nrmicro1852.

BULL, D., KEMP, A.E.S., WEEDON, G.P. (2000). A 160-k.y.-old record of El Niño–Southern Oscillation in marine production and coastal runoff from Santa Barbara Basin, California, USA. *Geology* **28** (11), 1007. DOI: 10.1130/0091-7613(2000)28<1007:AKROEN>2.0.CO;2.

CalCOFI. California Cooperative Oceanic Fisheries Investigation (CalCOFI), March 2018. http://www.calcofi.org.

CALVERT, S.E., FONTUGNE, M.R. (2011). On the late Pleistocene-Holocene sapropel record of climatic and oceanographic variability in the eastern Mediterranean. *Paleoceanography* **16**, 78–94. DOI: 10.1029/1999PA000488.

CAMUTI, K.S., MCGUIRE, P.T. (1999). Preparation of polished thin sections from poorly consolidated regolith and sediment materials. *Sedimentary Geology* **128** (1–2), 171–178. DOI: 10.1016/S0037-0738(99)00073-1.

CAPRIOLI, R.M., FARMER, T.B., GILE, J. (1997). Molecular imaging of biological samples: Localization of peptides and proteins using MALDI-TOF MS. *Analytical Chemistry* **69** (23), 4751–4760. DOI: 10.1021/ac970888i.

CASTAÑEDA, I.S., SCHEFUß, E., PÄTZOLD, J., SINNINGHE DAMSTÉ, J.S., WELDEAB, S., SCHOUTEN, S. (2010). Millennial-scale sea surface temperature changes in the eastern Mediterranean (Nile River Delta region) over the last 27,000 years. *Paleoceanography* **25** (1), PA1208. DOI: 10.1029/2009PA001740.

CHA, S., SONG, Z., NIKOLAU, B.J., YEUNG, E.S. (2009). Direct profiling and imaging of epicuticular waxes on Arabidopsis thaliana by laser desorption/ionization mass spectrometry using silver colloid as a matrix. *Analytical Chemistry* **81** (8), 2991–3000. DOI: 10.1021/ac802615r.

CHA, S., ZHANG, H., ILARSLAN, H.I., WURTELE, E.S., BRACHOVA, L., NIKOLAU, B.J., YEUNG, E.S. (2008). Direct profiling and imaging of plant metabolites in intact tissues by using colloidal graphite-assisted laser desorption ionization mass spectrometry. *The Plant Journal* **55** (2), 348–360. DOI: 10.1111/j.1365-313X.2008.03507.x.

CHAVEZ, F.P., PENNINGTON, J.T., CASTRO, C.G., RYAN, J.P., MICHISAKI, R.P., SCHLINING, B., WALZ, P., BUCK, K.R., MCFADYEN, A., COLLINS, C.A. (2002). Biological and chemical consequences of the 1997-1998 El Niño in central California waters. *Progress in Oceanography* **54** (1), 205–232. DOI: 10.1016/S0079-6611(02)00050-2.

CHAVEZ, F.P., RYAN, J.P., LLUCH-COTA, S.E., ÑIQUEN, M. (2003). From anchovies to sardines and back: multidecadal change in the Pacific Ocean. *Science* **299** (5604), 217–221. DOI: 10.1126/science.1075880.

CHECKLEY, D.M., BARTH, J.A. (2009). Patterns and processes in the California Current System. *Progress in Oceanography* **83** (1), 49–64. DOI: 10.1016/j.pocean.2009.07.028.

CHEN, W., MOHTADI, M., SCHEFUß, E., MOLLENHAUER, G. (2014). Organic-geochemical proxies of sea surface temperature in surface sediments of the tropical eastern Indian Ocean. *Deep Sea Research Part I: Oceanographic Research Papers* **88**, 17–29. DOI: 10.1016/j.dsr.2014.03.005.

CHHAK, K., DI LORENZO, E. (2007). Decadal variations in the California Current upwelling cells. *Geophysical Research Letters* **34** (14). DOI: 10.1029/2007GL030203.

COBB, K.M., CHARLES, C.D., CHENG, H., EDWARDS, R.L. (2003). El Niño/Southern Oscillation and tropical Pacific climate during the last millennium. *Nature* **424** (6946), 271–276. DOI: 10.1038/nature01779.

CONTE, M.H., SICRE, M.-A., RÜHLEMANN, C., WEBER, J.C., SCHULTE, S., SCHULZ-BULL, D., BLANZ, T. (2006). Global temperature calibration of the alkenone unsaturation index ($U^{K'}_{37}$) in surface waters and comparison with surface sediments. *Geochem. Geophys. Geosyst.* **7** (2), n/a-n/a. DOI: 10.1029/2005GC001054.

CONTE, M.H., THOMPSON, A., LESLEY, D., HARRIS, R.P. (1998). Genetic and physiological influences on the alkenone/alkenoate versus growth temperature relationship in *Emiliania huxleyi* and *Gephyrocapsa oceanica*. *Geochimica et Cosmochimica Acta* **62** (1), 51–68. DOI: 10.1016/S0016-7037(97)00327-X.

CONTE, M.H., WEBER, J.C., KING, L.L., WAKEHAM, S.G. (2001). The alkenone temperature signal in western North Atlantic surface waters. *Geochimica et Cosmochimica Acta* **65** (23), 4275–4287. DOI: 10.1016/S0016-7037(01)00718-9.

CRANWELL, P.A. (1973). Chain-length distribution of n-alkanes from lake sediments in relation to post-glacial environmental change. *Freshwater Biology* **3** (3), 259–265. DOI: 10.1111/j.1365-2427.1973.tb00921.x.

Croudace, I.W., Rothwell, R.G., 2015. Micro-XRF Studies of Sediment Cores: applications of a non-destructive tool for the environmental sciences. Springer, Dordrecht, 656 pp.

DAVIS, C.V., ONTIVEROS-CUADRAS, J.F., BENITEZ-NELSON, C., SCHMITTNER, A., TAPPA, E.J., OSBORNE, E., THUNELL, R.C. (2019). Ongoing increase in Eastern Tropical North Pacific denitrification as interpreted through the Santa Barbara Basin sedimentary $\delta^{15}N$ record. *Paleoceanography and Paleoclimatology* **35** (4), 535. DOI: 10.1029/2019PA003578.

DEUTSCH, C., BERELSON, W., THUNELL, R., WEBER, T., TEMS, C., MCMANUS, J., CRUSIUS, J., ITO, T., BAUMGARTNER, T., FERREIRA, V., MEY, J., VAN GEEN, A. (2014). Centennial changes in North Pacific anoxia linked to tropical trade winds. *Science* **345** (6197), 665–668. DOI: 10.1126/science.1252332.

DI LORENZO, E., MILLER, A.J., SCHNEIDER, N., MCWILLIAMS, J.C. (2005). The warming of the California Current System: Dynamics and ecosystem implications. *Journal of Physical Oceanography* **35** (3), 336–362. DOI: 10.1175/JPO-2690.1.

DI LORENZO, E., SCHNEIDER, N., COBB, K.M., FRANKS, P.J.S., CHHAK, K., MILLER, A.J., MCWILLIAMS, J.C., BOGRAD, S.J., ARANGO, H., CURCHITSER, E., POWELL, T.M., RIVIÈRE, P. (2008). North Pacific Gyre Oscillation links ocean climate and ecosystem change. *Geophysical Research Letters* **35** (8). DOI: 10.1029/2007GL032838.

DONG, Y., LI, B., MALITSKY, S., ROGACHEV, I., AHARONI, A., KAFTAN, F., SVATOŠ, A., FRANCESCHI, P. (2016). Sample preparation for mass spectrometry imaging of plant tissues: a review. *Frontiers in Plant Science* **7**(60.). DOI: 10.3389/fpls.2016.00060.

DREISEWERD, K. (2003). The desorption process in MALDI. *Chemical reviews* **103** (2), 395–426. DOI: 10.1021/cr010375i.

DUTTA, T.K., HARAYAMA, S. (2001). Time-of-flight mass spectrometric analysis of high-molecular-weight alkanes in crude oil by silver nitrate chemical ionization after laser desorption. *Analytical Chemistry* **73** (5), 864–869. DOI: 10.1021/ac0009797.

EGLINTON, G., BRADSHAW, S., RESELL, A., SARNTHEIN, M., PFLAUMANN, U., TIEDEMANN, R. (1992). Molecular record of secular sea surface temperature changes on 100-year timescales for glacial terminations I, II and IV. *Nature* **356** (6368), 423. DOI: 10.1038/356423a0.

EGLINTON, G., HAMILTON, R.J. (1967). Leaf epicuticular waxes. *Science* **156** (3780), 1322–1335. DOI: 10.1126/science.156.3780.1322.

ELLING, F.J., KÖNNEKE, M., LIPP, J.S., BECKER, K.W., GAGEN, E.J., HINRICHS, K.-U. (2014). Effects of growth phase on the membrane lipid composition of the thaumarchaeon *Nitrosopumilus maritimus* and their implications for archaeal lipid distributions in the marine environment. *Geochimica et Cosmochimica Acta* **141**, 579–597. DOI: 10.1016/j.gca.2014.07.005.

ELLING, F.J., KÖNNEKE, M., MUßMANN, M., GREVE, A., HINRICHS, K.-U. (2015). Influence of temperature, pH, and salinity on membrane lipid composition and TEX_{86} of marine planktonic thaumarchaeal isolates. *Geochimica et Cosmochimica Acta* **171**, 238–255. DOI: 10.1016/j.gca.2015.09.004.

ELVERT, M., POHLMAN, J.W., BECKER, K.W., GAGLIOTI, B., HINRICHS, K.-U., WOOLLER, M.J. (2016). Methane turnover and environmental change from Holocene lipid biomarker records in a thermokarst lake in Arctic Alaska. *The Holocene* **26** (11), 1766–1777. DOI: 10.1177/0959683616645942.

EMERY, K.O., HÜLSEMANN, J. (1961). The relationships of sediments, life and water in a marine basin. *Deep Sea Research* **8** (3-4), 165–180. DOI: 10.1016/0146-6313(61)90019-3.

EMERY, W.J., HAMILTON, K. (1985). Atmospheric forcing of interannual variability in the northeast Pacific Ocean: Connections with El Niño. *Journal of Geophysical Research* **90** (C1), 857. DOI: 10.1029/JC090iC01p00857.

EPSTEIN, B.L., D'HONDT, S., QUINN, J.G., ZHANG, J., HARGRAVES, P.E. (1998). An effect of dissolved nutrient concentrations on alkenone-based temperature estimates. *Paleoceanography* **13** (2), 122–126. DOI: 10.1029/97PA03358.

EVANS, T.W., KÖNNEKE, M., LIPP, J.S., ADHIKARI, R.R., TAUBNER, H., ELVERT, M., HINRICHS, K.-U. (2018). Lipid biosynthesis of *Nitrosopumilus maritimus* dissected by lipid specific radioisotope probing (lipid-RIP) under contrasting ammonium supply. *Geochimica et Cosmochimica Acta* **242**, 51–63. DOI: 10.1016/j.gca.2018.09.001.

EYSSEN, H.J., PARMENTIER, G.G., COMPERNOLLE, F.C., PAUW, G. de, PIESSENS-DENEF, M. (1973). Biohydrogenation of sterols by Eubacterium ATCC 21,408—nova species. *European journal of biochemistry* **36** (2), 411–421. DOI: 10.1111/j.1432-1033.1973.tb02926.x.

FIEDLER, P.C., MANTUA, N.J. (2017). How are warm and cool years in the California Current related to ENSO? *Journal of Geophysical Research: Oceans* **122** (7), 5936–5951. DOI: 10.1002/2017JC013094.

FIELD, D.B., BAUMGARTNER, T.R., CHARLES, C.D., FERREIRA-BARTRINA, V., OHMAN, M.D. (2006a). Planktonic foraminifera of the California Current reflect 20th-century warming. *Science* **311** (5757), 63–66. DOI: 10.1126/science.1116220.

FIELD, D.B., CAYAN, D., CHAVEZ, F.P. (2006b). Secular warming in the California current and North Pacific. *California Cooperative Oceanic Fisheries Investigations Report* **47**, 92.

FRANCIS, C.A., ROBERTS, K.J., BEMAN, J.M., SANTORO, A.E., OAKLEY, B.B. (2005). Ubiquity and diversity of ammonia-oxidizing archaea in water columns and sediments of the ocean. *Proceedings of the National Academy of Sciences of the United States of America* **102** (41), 14683–14688. DOI: 10.1073/pnas.0506625102.

GARCÍA-REYES, M., LARGIER, J. (2010). Observations of increased wind-driven coastal upwelling off central California. *Journal of Geophysical Research* **115** (C4), 849. DOI: 10.1029/2009JC005576.

GERGIS, J.L., FOWLER, A.M. (2009). A history of ENSO events since A.D. 1525: implications for future climate change. *Climatic Change* **92** (3-4), 343–387. DOI: 10.1007/s10584-008-9476-z.

GHOLIPOUR, Y., NONAMI, H., ERRA-BALSELLS, R. (2008). In situ analysis of plant tissue underivatized carbohydrates and on-probe enzymatic degraded starch by matrix-assisted laser desorption/ionization time-of-flight mass spectrometry by using carbon nanotubes as matrix. *Analytical biochemistry* **383** (2), 159–167. DOI: 10.1016/j.ab.2008.08.034.

GKINIS, V., SIMONSEN, S.B., BUCHARDT, S.L., WHITE, J.W.C., VINTHER, B.M. (2014). Water isotope diffusion rates from the NorthGRIP ice core for the last 16,000 years – Glaciological and paleoclimatic implications. *Earth and Planetary Science Letters* **405**, 132–141. DOI: 10.1016/j.epsl.2014.08.022.

GOERICKE, R., BOGRAD, S.J., GRUNDLE, D.S. (2015). Denitrification and flushing of the Santa Barbara Basin bottom waters. *Deep Sea Research Part II: Topical Studies in Oceanography* **112**, 53–60. DOI: 10.1016/j.dsr2.2014.07.012.

GOODWIN, R.J.A. (2012). Sample preparation for mass spectrometry imaging: small mistakes can lead to big consequences. *Journal of Proteomics* **75** (16), 4893–4911. DOI: 10.1016/j.jprot.2012.04.012.

GRELAUD, M., SCHIMMELMANN, A., BEAUFORT, L. (2009). Coccolithophore response to climate and surface hydrography in Santa Barbara Basin, California, AD 1917–2004. *Biogeosciences* **6** (10), 2025–2039. DOI: 10.5194/bg-6-2025-2009.

HANKIN, S.M., JOHN, P., SIMPSON, A.W., SMITH, G.P. (1996). Spatially resolved time-of-flight mass spectrometry of polycyclic aromatic hydrocarbons: Quantification studies. *Analytical Chemistry* **68** (18), 3238–3243. DOI: 10.1021/ac960356m.

HARVEY, H.R., FALLON, R.D., PATTON, J.S. (1986). The effect of organic matter and oxygen on the degradation of bacterial membrane lipids in marine sediments. *Geochimica et Cosmochimica Acta* **50** (5), 795–804. DOI: 10.1016/0016-7037(86)90355-8.

HAUG, G.H., GÜNTHER, D., PETERSON, L.C., SIGMAN, D.M., HUGHEN, K.A., AESCHLIMANN, B. (2003). Climate and the collapse of Maya civilization. *Science* **299** (5613), 1731–1735. DOI: 10.1126/science.1080444.

HAUG, G.H., HUGHEN, K.A., SIGMAN, D.M., PETERSON, L.C., RÖHL, U. (2001). Southward migration of the Intertropical Convergence Zone through the Holocene. *Science* **293** (5533), 1304–1308. DOI: 10.1126/science.1059725.

HEBTING, Y., SCHAEFFER, P., BEHRENS, A., ADAM, P., SCHMITT, G., SCHNECKENBURGER, P., BERNASCONI, S.M., ALBRECHT, P. (2006). Biomarker evidence for a major preservation pathway of sedimentary organic carbon. *Science* **312** (5780), 1627–1631. DOI: 10.1126/science.1126372.

HEEREN, R.M.A., KÜKRER-KALETAŞ, B., TABAN, I.M., MACALEESE, L., MCDONNELL, L.A. (2008). Quality of surface: the influence of sample preparation on MS-based biomolecular tissue imaging with MALDI-MS and (ME-) SIMS. *Applied Surface Science* **255** (4), 1289–1297. DOI: 10.1016/j.apsusc.2008.05.243.

HEEREN, R.M.A., SMITH, D.F., STAUBER, J., KÜKRER-KALETAŞ, B., MACALEESE, L. (2009). Imaging mass spectrometry: hype or hope? *Journal of the American Society for Mass Spectrometry* **20** (6), 1006–1014. DOI: 10.1016/j.jasms.2009.01.011.

HENDERSHOTT, M.C., WINANT, C.D. (1996). Surface circulation in the Santa Barbara channel. *Oceanography* **9** (2), 114–121.

HENDY, I.L., DUNN, L., SCHIMMELMANN, A., PAK, D.K. (2013). Resolving varve and radiocarbon chronology differences during the last 2000 years in the Santa Barbara Basin sedimentary record, California. *Quaternary International* **310**, 155–168. DOI: 10.1016/j.quaint.2012.09.006.

HENDY, I.L., NAPIER, T.J., SCHIMMELMANN, A. (2015). From extreme rainfall to drought: 250 years of annually resolved sediment deposition in Santa Barbara Basin, California. *Quaternary International* **387**, 3–12. DOI: 10.1016/j.quaint.2015.01.026.

HERBERT, T.D., SCHUFFERT, J.D., THOMAS, D., LANGE, C., WEINHEIMER, A.L., PELEO-ALAMPAY, A., HERGUERA, J.-C. (1998). Depth and seasonality of alkenone production along the California Margin inferred from a core top transect. *Paleoceanography* **13** (3), 263–271. DOI: 10.1029/98PA00069.

HICKEY, B.M. (1979). The California current system—hypotheses and facts. *Progress in Oceanography* **8** (4), 191–279.

HILLENKAMP, F., JASKOLLA, T.W., KARAS, M. (2014). The MALDI process and method. In. *Hillenkamp, F., Peter-Katalinic, J. (Eds.), MALDI MS: A Practical Guide to Instrumentation, Methods, and Applications, second ed. Wiley-VCH Verlag*, 1–40.

HINRICHS, K.-U., HAYES, J.M., SYLVA, S.P., BREWER, P.G., DELONG, E.F. (1999). Methane-consuming archaebacteria in marine sediments. *Nature* **398** (6730), 802. DOI: 10.1038/19751.

HINRICHS, K.-U., HMELO, L.R., SYLVA, S.P. (2003). Molecular fossil record of elevated methane levels in Late Pleistocene coastal waters. *Science* **299** (5610), 1214–1217. DOI: 10.1126/science.1079601.

HOPMANS, E.C., SCHOUTEN, S., PANCOST, R.D., VAN DER MEER, M.T.J., SINNINGHE DAMSTÉ, J.S. (2000). Analysis of intact tetraether lipids in archaeal cell material and sediments by high performance liquid chromatography/atmospheric pressure chemical ionization mass spectrometry. *Rapid Communications in Mass Spectrometry* **14** (7), 585–589. DOI: 10.1002/(SICI)1097-0231(20000415)14:7<585:AID-RCM913>3.0.CO;2-N.

HOPMANS, E.C., WEIJERS, J.W.H., SCHEFUß, E., HERFORT, L., SINNINGHE DAMSTÉ, J.S., SCHOUTEN, S. (2004). A novel proxy for terrestrial organic matter in sediments based on branched and isoprenoid tetraether lipids. *Earth and Planetary Science Letters* **224** (1–2), 107–116. DOI: 10.1016/j.epsl.2004.05.012.

HUANG, B., BANZON, V.F., FREEMAN, E., LAWRIMORE, J., LIU, W., PETERSON, T.C., SMITH, T.M., THORNE, P.W., WOODRUFF, S.D., ZHANG, H.-M. (2015). Extended Reconstructed Sea Surface Temperature Version 4 (ERSST.v4). Part I: Upgrades and intercomparisons. *Journal of Climate* **28** (3), 911–930. DOI: 10.1175/JCLI-D-14-00006.1.

HUANG, W.-Y., MEINSCHEIN, W.G. (1976). Sterols as source indicators of organic materials in sediments. *Geochimica et Cosmochimica Acta* **40**, 323–330. DOI: 10.1016/0016-7037(76)90210-6.

HUANG, W.-Y., MEINSCHEIN, W.G. (1979). Sterols as ecological indicators. *Geochimica et Cosmochimica Acta* **43** (5), 739–745. DOI: 10.1016/0016-7037(79)90257-6.

HUGUET, C., SCHIMMELMANN, A., THUNELL, R.C., LOURENS, L.J., SINNINGHE DAMSTÉ, J.S., SCHOUTEN, S. (2007). A study of the TEX_{86} paleothermometer in the water column and sediments of the Santa Barbara Basin, California. *Paleoceanography* **22** (3). DOI: 10.1029/2006PA001310.

HURLEY, S.J., ELLING, F.J., KÖNNEKE, M., BUCHWALD, C., WANKEL, S.D., SANTORO, A.E., LIPP, J.S., HINRICHS, K.-U., PEARSON, A. (2016). Influence of ammonia oxidation rate on thaumarchaeal lipid composition and the TEX_{86} temperature proxy. *Proceedings of the National Academy of Sciences of the United States of America* **113** (28), 7762–7767. DOI: 10.1073/pnas.1518534113.

HURLEY, S.J., LIPP, J.S., CLOSE, H.G., HINRICHS, K.-U., PEARSON, A. (2018). Distribution and export of isoprenoid tetraether lipids in suspended particulate matter from the water column of the Western Atlantic Ocean. *Organic Geochemistry* **116**, 90–102. DOI: 10.1016/j.orggeochem.2017.11.010.

HURRELL, J.W. (1995). Decadal trends in the North Atlantic oscillation: regional temperatures and precipitation. *Science* **269** (5224), 676–679. DOI: 10.1126/science.269.5224.676.

HUYER, A. (1983). Coastal upwelling in the California Current system. *Progress in Oceanography* **12** (3), 259–284. DOI: 10.1016/0079-6611(83)90010-1.

JACOX, M.G., FIECHTER, J., MOORE, A.M., EDWARDS, C.A. (2015). ENSO and the California Current coastal upwelling response. *Journal of Geophysical Research: Oceans* **120** (3), 1691–1702. DOI: 10.1002/2014JC010650.

JUN, J.H., SONG, Z., LIU, Z., NIKOLAU, B.J., YEUNG, E.S., LEE, Y.J. (2010). High-spatial and high-mass resolution imaging of surface metabolites of Arabidopsis thaliana by laser desorption-ionization mass spectrometry using colloidal silver. *Analytical Chemistry* **82** (8), 3255–3265. DOI: 10.1021/ac902990p.

KAHR, M.S., WILKINS, C.L. (1993). Silver nitrate chemical ionization for analysis of hydrocarbon polymers by laser desorption Fourier transform mass spectrometry. *Journal of the American Society for Mass Spectrometry* **4** (6), 453–460. DOI: 10.1016/1044-0305(93)80002-G.

KANEDA, T. (1991). Iso-and anteiso-fatty acids in bacteria: Biosynthesis, function, and taxonomic significance. *Microbiology and Molecular Biology Reviews* **55** (2), 288–302.

KARNER, M.B., DELONG, E.F., KARL, D.M. (2001). Archaeal dominance in the mesopelagic zone of the Pacific Ocean. *Nature* **409** (6819), 507–510. DOI: 10.1038/35054051.

KENNEDY, J.A., BRASSELL, S.C. (1992). Molecular records of twentieth-century El Niño events in laminated sediments from the Santa Barbara Basin. *Nature* **357** (6373), 62–64. DOI: 10.1038/357062a0.

KERWIN, J.L., WIENS, A.M., ERICSSON, L.H. (1996). Identification of fatty acids by electrospray mass spectrometry and tandem mass spectrometry. *Journal of Mass Spectrometry* **31** (2), 184–192. DOI: 10.1002/(SICI)1096-9888(199602)31:2<184:AID-JMS283>3.0.CO;2-2.

KIM, J.-H., VAN DER MEER, J., SCHOUTEN, S., HELMKE, P., WILLMOTT, V., SANGIORGI, F., KOÇ, N., HOPMANS, E.C., SINNINGHE DAMSTÉ, J.S. (2010). New indices and calibrations derived from the distribution of crenarchaeal isoprenoid tetraether lipids: Implications for past sea surface temperature reconstructions. *Geochimica et Cosmochimica Acta* **74** (16), 4639–4654. DOI: 10.1016/j.gca.2010.05.027.

KIM, Y.-W., SUNG, C., LEE, S., KIM, K.-J., YANG, Y.-H., KIM, B.-G., LEE, Y.K., RYU, H.W., KIM, Y.-G. (2015). MALDI-MS-based quantitative analysis for ketone containing homoserine lactones in Pseudomonas aeruginosa. *Analytical Chemistry* **87** (2), 858–863. DOI: 10.1021/ac5039362.

KNOCHENMUSS, R., ZENOBI, R. (2003). MALDI ionization: The role of in-plume processes. *Chemical reviews* **103** (2), 441–452. DOI: 10.1021/cr0103773.

KÖNNEKE, M., BERNHARD, A.E., LA TORRE, J.R. de, WALKER, C.B., WATERBURY, J.B., STAHL, D.A. (2005). Isolation of an autotrophic ammonia-oxidizing marine archaeon. *Nature* **437** (7058), 543–546. DOI: 10.1038/nature03911.

KUYPERS, M.M.M., BLOKKER, P., ERBACHER, J., KINKEL, H., PANCOST, R.D., SCHOUTEN, S., SINNINGHE DAMSTÉ, J.S. (2001). Massive expansion of marine Archaea during a Mid-Cretaceous oceanic anoxic event. *Science* **293** (5527), 92–95. DOI: 10.1126/science.1058424.

KUYPERS, M.M.M., PANCOST, R.D., SINNINGHE DAMSTÉ, J.S. (1999). A large and abrupt fall in atmospheric CO 2 concentration during Cretaceous times. *Nature* **399** (6734), 342. DOI: 10.1038/20659.

KUYPERS, M.M.M., SLIEKERS, A.O., LAVIK, G., SCHMID, M., JØRGENSEN, B.B., KUENEN, J.G., SINNINGHE DAMSTÉ, J.S., STROUS, M., JETTEN, M.S.M. (2003). Anaerobic ammonium oxidation by anammox bacteria in the Black Sea. *Nature* **422** (6932), 608–611. DOI: 10.1038/nature01472.

LAMB, P.J., PEPPLER, R.A. (1987). North Atlantic oscillation: concept and an application. *Bulletin of the American Meteorological Society* **68** (10), 1218–1225. DOI: 10.1175/1520-0477(1987)068<1218:NAOCAA>2.0.CO;2.

LANGE, C.B., BERGER, W.H., BURKE, S.K., CASEY, R.E., SCHIMMELMANN, A., SOUTAR, A., WEINHEIMER, A.L. (1987). El Niño in Santa Barbara Basin: Diatom, radiolarian and foraminiferan responses to the "1983 El Niño" event. *Marine Geology* **78** (1), 153–160. DOI: 10.1016/0025-3227(87)90074-0.

LANGE, C.B., BURKE, S.K., BERGER, W.H. (1990). Biological production off Southern California is linked to climatic change. *Climatic Change* **16** (3), 319–329. DOI: 10.1007/BF00144507.

LANGE, C.B., WEINHEIMER, A.L., REID, F.M.H., THUNELL, R.C. (1997). Sedimentation patterns of diatoms, radiolarians, and silicoflagellates in Santa Barbara Basin, California. *California Cooperative Oceanic Fisheries Investigations Report* **38**, 161–170.

LATTAUD, J., KIM, J.-H., JONGE, C. de, ZELL, C., SINNINGHE DAMSTÉ, J.S., SCHOUTEN, S. (2017). The C32 alkane-1, 15-diol as a tracer for riverine input in coastal seas. *Geochimica et Cosmochimica Acta* **202**, 146–158. DOI: 10.1016/j.gca.2016.12.030.

LEE, K.E., KIM, J.-H., WILKE, I., HELMKE, P., SCHOUTEN, S. (2008). A study of the alkenone, TEX_{86}, and planktonic foraminifera in the Benguela Upwelling System: Implications for past sea surface temperature estimates. *Geochemistry, Geophysics, Geosystems* **9** (10). DOI: 10.1029/2008GC002056.

LEIDER, A., HINRICHS, K.-U., MOLLENHAUER, G., VERSTEEGH, G.J.M. (2010). Core-top calibration of the lipid-based $U^{K'}_{37}$ and TEX_{86} temperature proxies on the southern Italian shelf (SW Adriatic Sea, Gulf of Taranto). *Earth and Planetary Science Letters* **300** (1), 112–124. DOI: 10.1016/j.epsl.2010.09.042.

LIMA, A.L.C., FARRINGTON, J.W., REDDY, C.M. (2005). Combustion-derived polycyclic aromatic hydrocarbons in the environment—a review. *Environmental Forensics* **6** (2), 109–131. DOI: 10.1080/15275920590952739.

LIPP, J.S., MORONO, Y., INAGAKI, F., HINRICHS, K.-U. (2008). Significant contribution of Archaea to extant biomass in marine subsurface sediments. *Nature* **454** (7207), 991. DOI: 10.1038/nature07174.

LIU, X.-L., LIPP, J.S., BIRGEL, D., SUMMONS, R.E., HINRICHS, K.-U. (2018). Predominance of parallel glycerol arrangement in archaeal tetraethers from marine sediments: structural features revealed from degradation products. *Organic Geochemistry* **115**, 12–23. DOI: 10.1016/j.orggeochem.2017.09.009.

LLUCH-COTA, D.B., WOOSTER, W.S., HARE, S.R. (2001). Sea surface temperature variability in coastal areas of the northeastern Pacific related to the El Niño-Southern Oscillation and the Pacific Decadal Oscillation. *Geophysical Research Letters* **28** (10), 2029–2032. DOI: 10.1029/2000GL012429.

LOPES DOS SANTOS, R.A., PRANGE, M., CASTAÑEDA, I.S., SCHEFUß, E., MULITZA, S., SCHULZ, M., NIEDERMEYER, E.M., SINNINGHE DAMSTÉ, J.S., SCHOUTEN, S. (2010). Glacial–interglacial variability in Atlantic meridional overturning circulation and thermocline adjustments in the tropical North Atlantic. *Earth and Planetary Science Letters* **300** (3-4), 407–414. DOI: 10.1016/j.epsl.2010.10.030.

LÜCKGE, A., DOOSE-ROLINSKI, H., KHAN, A.A., SCHULZ, H., RAD, U.v. (2001). Monsoonal variability in the northeastern Arabian Sea during the past 5000years: Geochemical evidence from laminated sediments. *Palaeogeography, Palaeoclimatology, Palaeoecology* **167** (3), 273–286. DOI: 10.1016/S0031-0182(00)00241-8.

LYNN, R.J., COLLINS, C.A., MANTYLA, A.W., SCHWING, F.B., BAUMGARTNER, T., HAYWARD, T.L., MURPHREE, T., SAKUMA, K.M., GARCIA, J., HYRENBACH, K.D. (1997). The state of the California Current, 1997-1998: transition to El Niño conditions. *California Cooperative Oceanic Fisheries Investigations Report, 25-49*

LYNN, R.J., SCHWING, F.B., HAYWARD, T.L. (1995). The effect of the 1991-1993 ENSO on the California Current System. *California Cooperative Oceanic Fisheries Investigations Report*, 57–71.

MANTUA, N.J., HARE, S.R. (2002). The Pacific decadal oscillation. *Journal of Oceanography* **58** (1), 35–44. DOI: 10.1023/A:1015820616384.

MANTUA, N.J., HARE, S.R., ZHANG, Y., WALLACE, J.M., FRANCIS, R.C. (1997). A Pacific interdecadal climate oscillation with impacts on salmon production. *Bulletin of the American Meteorological Society* **78** (6), 1069–1080. DOI: 10.1175/1520-0477(1997)078<1069:APICOW>2.0.CO;2.

MARLOWE, I.T., BRASSELL, S.C., EGLINTON, G., GREEN, J.C. (1990). Long-chain alkenones and alkyl alkenoates and the fossil coccolith record of marine sediments. *Chemical Geology* **88**, 349–375. DOI: 10.1016/0009-2541(90)90098-R.

MARSHALL, A.G., HENDRICKSON, C.L. (2008). High-resolution mass spectrometers. *Annual Review of Analytical Chemistry* **1**, 579–599. DOI: 10.1146/annurev.anchem.1.031207.112945.

MASSANA, R., MURRAY, A.E., PRESTON, C.M., DELONG, E.F. (1997). Vertical distribution and phylogenetic characterization of marine planktonic Archaea in the Santa Barbara Channel. *Applied and Environmental Microbiology* **63** (1), 50–56.

MCGOWAN, J.A., BOGRAD, S.J., LYNN, R.J., MILLER, A.J. (2003). The biological response to the 1977 regime shift in the California Current. *Deep Sea Research Part II: Topical Studies in Oceanography* **50** (14), 2567–2582. DOI: 10.1016/S0967-0645(03)00135-8.

MCPHADEN, M.J. (2002). El Niño and La Niña: causes and global consequences. *Encyclopedia of Global Environmental Change* **1**, 1–17.

MCPHADEN, M.J., ZEBIAK, S.E., GLANTZ, M.H. (2006). ENSO as an integrating concept in earth science. *Science* **314** (5806), 1740–1745. DOI: 10.1126/science.1132588.

MENSING, S.A., MICHAELSEN, J., BYRNE, R. (1999). A 560-year record of Santa Ana fires reconstructed from charcoal deposited in the Santa Barbara Basin, California. *Quaternary Research* **51** (3), 295–305. DOI: 10.1006/qres.1999.2035.

MINNICH, R.A. (1983). Fire mosaics in southern California and northern Baja California. *Science (New York, N.Y.)* **219** (4590), 1287–1294. DOI: 10.1126/science.219.4590.1287.

MOINI, M., JONES, B.L., ROGERS, R.M., JIANG, L. (1998). Sodium trifluoroacetate as a tune/calibration compound for positive- and negative-ion electrospray ionization mass spectrometry in the mass range of 100–4000 Da. *Journal of the American Society for Mass Spectrometry* **9** (9), 977–980. DOI: 10.1016/S1044-0305(98)00079-8.

MOLLENHAUER, G., BASSE, A., KIM, J.-H., SINNINGHE DAMSTÉ, J.S., FISCHER, G. (2015). A four-year record of $U^{K'}_{37}$ - and TEX_{86}-derived sea surface temperature estimates from sinking particles in the filamentous upwelling region off Cape Blanc, Mauritania. *Deep Sea Research Part I: Oceanographic Research Papers* **97**, 67–79. DOI: 10.1016/j.dsr.2014.11.015.

MONTSKO, G., VACZY, A., MAASZ, G., MERNYAK, E., FRANK, E., BAY, C., KADAR, Z., OHMACHT, R., WOLFLING, J., MARK, L. (2009). Analysis of nonderivatized steroids by matrix-assisted laser desorption/ionization time-of-flight mass spectrometry using C70 fullerene as matrix. *Analytical and Bioanalytical Chemistry* **395** (3), 869–874. DOI: 10.1007/s00216-009-3018-z.

MÜLLER, P.J., KIRST, G., RUHLAND, G., STORCH, I. von, ROSELL-MELÉ, A. (1998). Calibration of the alkenone paleotemperature index $U^{K'}_{37}$ based on core-tops from the eastern South Atlantic and the global ocean (60° N-60° S). *Geochimica et Cosmochimica Acta* **62** (10), 1757–1772. DOI: 10.1016/S0016-7037(98)00097-0.

MURRAY, A.E., BLAKIS, A., MASSANA, R., STRAWZEWSKI, S., PASSOW, U., ALLDREDGE, A., DELONG, E.F. (1999). A time series assessment of planktonic archaeal variability in the Santa Barbara Channel. *Aquatic Microbial Ecology* **20** (2), 129–145. DOI: 10.3354/ame020129.

NAAFS, B.D.A., STEIN, R., HEFTER, J., KHÉLIFI, N., SCHEPPER, S. de, HAUG, G.H. (2010). Late Pliocene changes in the North Atlantic Current. *Earth and Planetary Science Letters* **298** (3-4), 434–442. DOI: 10.1016/j.epsl.2010.08.023.

NAKAGAWA, T., SUIGETSU 2006 PROJECT MEMBERS (2014). High-precision sampling of laminated sediments: strategies from Lake Suigetsu. *PAGES News* **22** (1), 12–13.

NAPIER, T.J., HENDY, I.L., HINNOV, L.A., BROWN, E.T., SHEVENELL, A. (2018). Subtropical hydroclimate during Termination V (~430-422 ka): Annual records of extreme precipitation, drought, and interannual variability from Santa Barbara Basin. *Quaternary Science Reviews* **191**, 73–88. DOI: 10.1016/j.quascirev.2018.05.003.

NEDERBRAGT, A.J., THUROW, J. (2005). Amplitude of ENSO cycles in the Santa Barbara Basin, off California, during the past 15 000 years. *Journal of Quaternary Science* **20** (5), 447–456. DOI: 10.1002/jqs.946.

NELSON, K.A., DANIELS, G.J., FOURNIE, J.W., HEMMER, M.J. (2013). Optimization of whole-body zebrafish sectioning methods for mass spectrometry imaging. *Journal of Biomolecular Techniques* **24** (3), 119–127. DOI: 10.7171/jbt.13-2403-002.

NISHIMURA, M., KOYAMA, T. (1977). The occurrence of stanols in various living organisms and the behavior of sterols in contemporary sediments. *Geochimica et Cosmochimica Acta* **41** (3), 379–385. DOI: 10.1016/0016-7037(77)90265-4.

PAILLARD, D., LABEYRIE, L., YIOU, P. (1996). Macintosh program performs time-series analysis. *Eos, Transactions American Geophysical Union - AGU Publications* **77** (39), 379. DOI: 10.1029/96EO00259.

PALACIOS, D.M., BOGRAD, S.J., MENDELSSOHN, R., SCHWING, F.B. (2004). Long-term and seasonal trends in stratification in the California Current, 1950–1993. *Journal of Geophysical Research: Oceans* **109** (C10), 307. DOI: 10.1029/2004JC002380.

PANCOST, R.D., BOOT, C.S. (2004). The palaeoclimatic utility of terrestrial biomarkers in marine sediments. *Marine Chemistry* **92** (1-4), 239–261. DOI: 10.1016/j.marchem.2004.06.029.

PEARSON, A., INGALLS, A.E. (2013). Assessing the use of archaeal lipids as marine environmental proxies. *Annual Review of Earth and Planetary Sciences* **41** (1), 359–384. DOI: 10.1146/annurev-earth-050212-123947.

PERDIAN, D.C., CHA, S., OH, J., SAKAGUCHI, D.S., YEUNG, E.S., LEE, Y.J. (2010). In situ probing of cholesterol in astrocytes at the single-cell level using laser desorption ionization mass spectrometric imaging with colloidal silver. *Rapid Communications in Mass Spectrometry* **24** (8), 1147–1154. DOI: 10.1002/rcm.4491.

PERRY, G.J., VOLKMAN, J.K., JOHNS, R.B., BAVOR JR, H.J. (1979). Fatty acids of bacterial origin in contemporary marine sediments. *Geochimica et Cosmochimica Acta* **43** (11), 1715–1725. DOI: 10.1016/0016-7037(79)90020-6.

PIKE, J., KEMP, A.E.S. (1996). Preparation and analysis techniques for studies of laminated sediments. *Geological Society, London, Special Publications* **116** (1), 37–48. DOI: 10.1144/GSL.SP.1996.116.01.05.

PRAHL, F.G., MUEHLHAUSEN, L.A., ZAHNLE, D.L. (1988). Further evaluation of long-chain alkenones as indicators of paleoceanographic conditions. *Geochimica et Cosmochimica Acta* **52** (9), 2303–2310. DOI: 10.1016/0016-7037(88)90132-9.

PRAHL, F.G., SPARROW, M.A., WOLFE, G.V. (2003). Physiological impacts on alkenone paleothermometry. *Paleoceanography* **18** (2). DOI: 10.1029/2002PA000803.

PRAHL, F.G., WAKEHAM, S.G. (1987). Calibration of unsaturation patterns in long-chain ketone compositions for palaeotemperature assessment. *Nature* **330** (6146), 367–369. DOI: 10.1038/330367a0.

QIN, W., CARLSON, L.T., ARMBRUST, E.V., DEVOL, A.H., MOFFETT, J.W., STAHL, D.A., INGALLS, A.E. (2015). Confounding effects of oxygen and temperature on the TEX_{86} signature of marine Thaumarchaeota. *Proceedings of the National Academy of Sciences of the United States of America* **112** (35), 10979–10984. DOI: 10.1073/pnas.1501568112.

RAMPEN, S.W., WILLMOTT, V., KIM, J.-H., ULIANA, E., MOLLENHAUER, G., SCHEFUß, E., SINNINGHE DAMSTÉ, J.S., SCHOUTEN, S. (2012). Long chain 1, 13-and 1, 15-diols as a potential proxy for palaeotemperature reconstruction. *Geochimica et Cosmochimica Acta* **84**, 204–216. DOI: 10.1016/j.gca.2012.01.024.

REED, W.E., MANKIEWICZ, P. (1975). Molecular stratigraphy. *Nature* **254** (5496), 127–129. DOI: 10.1038/254127a0.

REIMERS, C.E., LANGE, C.B., TABAK, M., BERNHARD, J.M. (1990). Seasonal spillover and varve formation in the Santa Barbara Basin, California. *Limnology and Oceanography* **35** (7), 1577–1585. DOI: 10.4319/lo.1990.35.7.1577.

REPETA, D.J., SIMPSON, D.J., JØRGENSEN, B.B., JANNASCH, H.W. (1989). Evidence for anoxygenic photosynthesis from the distribution of bacterio-chlorophylls in the Black Sea. *Nature* **342** (6245), 69. DOI: 10.1038/342069a0.

ROEMMICH, D. (1992). Ocean warming and sea level rise along the southwest u.s. Coast. *Science* **257** (5068), 373–375. DOI: 10.1126/science.257.5068.373.

ROEMMICH, D., MCGOWAN, J.A. (1995). Climatic warming and the decline of zooplankton in the California Current. *Science* **267** (5202), 1324–1326. DOI: 10.1126/science.267.5202.1324.

ROMMERSKIRCHEN, F., CONDON, T., MOLLENHAUER, G., DUPONT, L., SCHEFUß, E. (2011). Miocene to Pliocene development of surface and subsurface temperatures in the Benguela Current system. *Paleoceanography and Paleoclimatology* **26** (3). DOI: 10.1029/2010PA002074

ROSELL-MELÉ, A., PRAHL, F.G. (2013). Seasonality of $U^{K'}_{37}$ temperature estimates as inferred from sediment trap data. *Quaternary Science Reviews* **72**, 128–136. DOI: 10.1016/j.quascirev.2013.04.017.

ROSENFELD, R.S., HELLMANN, L. (1971). Reduction and esterification of cholesterol and sitosterol by homogenates of feces. *Journal of Lipid Research* **12** (2), 192–197.

SANGER, J.E. (1988). Fossil pigments in paleoecology and paleolimnology. *Palaeogeography, Palaeoclimatology, Palaeoecology* **62** (1-4), 343–359. DOI: 10.1016/0031-0182(88)90061-2.

SANTORO, A.E., CASCIOTTI, K.L., FRANCIS, C.A. (2010). Activity, abundance and diversity of nitrifying archaea and bacteria in the central California Current. *Environmental Microbiology* **12** (7), 1989–2006. DOI: 10.1111/j.1462-2920.2010.02205.x.

SCHIMMELMANN, A., HENDY, I.L., DUNN, L., PAK, D.K., LANGE, C.B. (2013). Revised~ 2000-year chronostratigraphy of partially varved marine sediment in Santa Barbara Basin, California. *GFF* **135** (3-4), 258–264. DOI: 10.1080/11035897.2013.773066.

SCHIMMELMANN, A., LANGE, C.B. (1996). Tales of 1001 varves: a review of Santa Barbara Basin sediment studies. *Geological Society, London, Special Publications* **116** (1), 121–141. DOI: 10.1144/GSL.SP.1996.116.01.12.

SCHIMMELMANN, A., LANGE, C.B., BERGER, W.H. (1990). Climatically controlled marker layers in Santa Barbara Basin sediments and fine-scale core-to-core correlation. *Limnology and Oceanography* **35** (1), 165–173. DOI: 10.4319/lo.1990.35.1.0165.

SCHIMMELMANN, A., LANGE, C.B., SCHIEBER, J., FRANCUS, P., OJALA, A.E.K., ZOLITSCHKA, B. (2016). Varves in marine sediments: a review. *Earth-Science Reviews* **159**, 215–246. DOI: 10.1016/j.earscirev.2016.04.009.

SCHLITZER, R. Ocean Data View. https://odv.awi.de, 2018.

SCHMIDT, F., HINRICHS, K.-U., ELVERT, M. (2010). Sources, transport, and partitioning of organic matter at a highly dynamic continental margin. *Marine Chemistry* **118** (1-2), 37–55. DOI: 10.1016/j.marchem.2009.10.003.

SCHOUTEN, S., FORSTER, A., PANOTO, F.E., SINNINGHE DAMSTÉ, J.S. (2007). Towards calibration of the TEX_{86} palaeothermometer for tropical sea surface temperatures in ancient greenhouse worlds. *Organic Geochemistry* **38** (9), 1537–1546. DOI: 10.1016/j.orggeochem.2007.05.014.

SCHOUTEN, S., HOPMANS, E.C., FORSTER, A., VAN BREUGEL, Y., KUYPERS, M.M.M., SINNINGHE DAMSTÉ, J.S. (2003). Extremely high sea-surface temperatures at low latitudes during the middle Cretaceous as revealed by archaeal membrane lipids. *Geology* **31** (12), 1069–1072. DOI: 10.1130/G19876.1.

SCHOUTEN, S., HOPMANS, E.C., SCHEFUß, E., SINNINGHE DAMSTÉ, J.S. (2002). Distributional variations in marine crenarchaeotal membrane lipids: a new tool for reconstructing ancient sea water temperatures? *Earth and Planetary Science Letters* **204** (1), 265–274. DOI: 10.1016/S0012-821X(02)00979-2.

SCHOUTEN, S., HOPMANS, E.C., SINNINGHE DAMSTÉ, J.S. (2013). The organic geochemistry of glycerol dialkyl glycerol tetraether lipids: A review. *Organic Geochemistry* **54**, 19–61. DOI: 10.1016/j.orggeochem.2012.09.006.

SCHUBOTZ, F., WAKEHAM, S.G., LIPP, J.S., FREDRICKS, H.F., HINRICHS, K.-U. (2009). Detection of microbial biomass by intact polar membrane lipid analysis in the water column and surface sediments of the Black Sea. *Environmental Microbiology* **11** (10), 2720–2734. DOI: 10.1111/j.1462-2920.2009.01999.x.

SCHWARTZ, S.A., REYZER, M.L., CAPRIOLI, R.M. (2003). Direct tissue analysis using matrix-assisted laser desorption/ionization mass spectrometry: practical aspects of sample preparation. *Journal of Mass Spectrometry* **38** (7), 699–708. DOI: 10.1002/jms.505.

SCHWING, F.B., MENDELSSOHN, R. (1997). Increased coastal upwelling in the California Current System. *Journal of Geophysical Research: Oceans* **102** (C2), 3421–3438. DOI: 10.1029/96JC03591.

SEPÚLVEDA, J., PANTOJA, S., HUGHEN, K.A., BERTRAND, S., FIGUEROA, D., LEÓN, T., DRENZEK, N.J., LANGE, C. (2009a). Late Holocene sea-surface temperature and precipitation variability in northern Patagonia, Chile (Jacaf Fjord, 44°S). *Quaternary Research* **72** (3), 400–409. DOI: 10.1016/j.yqres.2009.06.010.

SEPÚLVEDA, J., WENDLER, J.E., SUMMONS, R.E., HINRICHS, K.-U. (2009b). Rapid resurgence of marine productivity after the Cretaceous-Paleogene mass extinction. *Science* **326** (5949), 129–132. DOI: 10.1126/science.1176233.

SIMONEIT, B.R.T. (2002). Biomass burning – a review of organic tracers for smoke from incomplete combustion. *Applied Geochemistry* **17** (3), 129–162. DOI: 10.1016/S0883-2927(01)00061-0.

SIMPSON, J.J. (1992). Response of the Southern California current system to the mid-latitude North Pacific coastal warming events of 1982–1983 and 1940–1941. *Fisheries Oceanography* **1** (1), 57–79. DOI: 10.1111/j.1365-2419.1992.tb00025.x.

SINNINGHE DAMSTÉ, J.S., RIJPSTRA, W.I.C., HOPMANS, E.C., DEN UIJL, M.J., WEIJERS, J.W.H., SCHOUTEN, S. (2018). The enigmatic structure of the crenarchaeol isomer. *Organic Geochemistry* **124**, 22–28. DOI: 10.1016/j.orggeochem.2018.06.005.

SINNINGHE DAMSTÉ, J.S., SCHOUTEN, S., HOPMANS, E.C., VAN DUIN, A.C.T., GEENEVASEN, J.A.J. (2002). Crenarchaeol: the characteristic core glycerol dibiphytanyl glycerol tetraether membrane lipid of cosmopolitan pelagic crenarchaeota. *Journal of Lipid Research* **43** (10), 1641–1651. DOI: 10.1194/jlr.M200148-JLR200.

SLUIJS, A., SCHOUTEN, S., PAGANI, M., WOLTERING, M., BRINKHUIS, H., SINNINGHE DAMSTÉ, J.S., DICKENS, G.R., HUBER, M., REICHART, G.-J., STEIN, R. (2006). Subtropical Arctic Ocean temperatures during the Palaeocene/Eocene thermal maximum. *Nature* **441** (7093), 610. DOI: 10.1038/nature04668.

SMITH, J.M., DAMASHEK, J., CHAVEZ, F.P., FRANCIS, C.A. (2016). Factors influencing nitrification rates and the abundance and transcriptional activity of ammonia-oxidizing microorganisms in the dark northeast Pacific Ocean. *Limnology and Oceanography* **61** (2), 596–609. DOI: 10.1002/lno.10235.

SOUTAR, A., CRILL, P.A. (1977). Sedimentation and climatic patterns in the Santa Barbara Basin during the 19th and 20th centuries. *Geological Society of America Bulletin* **88** (8), 1161–1172. DOI: 10.1130/0016-7606(1977)88<1161:SACPIT>2.0.CO;2.

SPANG, A., HATZENPICHLER, R., BROCHIER-ARMANET, C., RATTEI, T., TISCHLER, P., SPIECK, E., STREIT, W., STAHL, D.A., WAGNER, M., SCHLEPER, C. (2010). Distinct gene set in two different lineages of ammonia-oxidizing archaea supports the phylum Thaumarchaeota. *Trends in Microbiology* **18** (8), 331–340. DOI: 10.1016/j.tim.2010.06.003.

STEFFENSEN, J.P., ANDERSEN, K.K., BIGLER, M., CLAUSEN, H.B., DAHL-JENSEN, D., FISCHER, H., GOTO-AZUMA, K., HANSSON, M., JOHNSEN, S.J., JOUZEL, J., MASSON-DELMOTTE, V., POPP, T., RASMUSSEN, S.O., RÖTHLISBERGER, R., RUTH, U., STAUFFER, B., SIGGAARD-ANDERSEN, M.-L., SVEINBJÖRNSDÓTTIR, A.E., SVENSSON, A., WHITE, J.W.C. (2008). High-resolution Greenland ice core data show abrupt climate change happens in few years. *Science* **321** (5889), 680–684. DOI: 10.1126/science.1157707.

STOECKLI, M., CHAURAND, P., HALLAHAN, D.E., CAPRIOLI, R.M. (2001). Imaging mass spectrometry: A new technology for the analysis of protein expression in mammalian tissues. *Nature medicine* **7** (4), 493. DOI: 10.1038/86573.

STURT, H.F., SUMMONS, R.E., SMITH, K., ELVERT, M., HINRICHS, K.-U. (2004a). Intact polar membrane lipids in prokaryotes and sediments deciphered by high-performance liquid chromatography/electrospray ionization multistage mass spectrometry—new biomarkers for biogeochemistry and microbial ecology. *Rapid Communications in Mass Spectrometry* **18** (6), 617–628. DOI: 10.1002/rcm.1378.

STURT, H.F., SUMMONS, R.E., SMITH, K., ELVERT, M., HINRICHS, K.-U. (2004b). Intact polar membrane lipids in prokaryotes and sediments deciphered by high-performance liquid chromatography/electrospray ionization multistage mass spectrometry—new biomarkers for biogeochemistry and microbial ecology. *Rapid Communications in Mass Spectrometry* **18** (6), 617–628. DOI: 10.1002/rcm.1378.

SUGIURA, Y., SHIMMA, S., SETOU, M. (2006). Thin sectioning improves the peak intensity and signal-to-noise ratio in direct tissue mass spectrometry. *Journal of the Mass Spectrometry Society of Japan* **54** (2), 45–48. DOI: 10.5702/massspec.54.45.

SUZUKI, T., MIDONOYA, H., SHIOI, Y. (2009). Analysis of chlorophylls and their derivatives by matrix-assisted laser desorption/ionization–time-of-flight mass spectrometry. *Analytical biochemistry* **390** (1), 57–62. DOI: 10.1016/j.ab.2009.04.005.

TABAN, I.M., ALTELAAR, A.M., VAN DER BURGT, Y.E.M., MCDONNELL, L.A., HEEREN, R.M.A., FUCHSER, J., BAYKUT, G. (2007). Imaging of peptides in the rat brain using MALDI-FTICR mass spectrometry. *Journal of the American Society for Mass Spectrometry* **18** (1), 145–151. DOI: 10.1016/j.jasms.2006.09.017.

TALBOT, H.M., FARRIMOND, P. (2007). Bacterial populations recorded in diverse sedimentary biohopanoid distributions. *Organic Geochemistry* **38** (8), 1212–1225. DOI: 10.1016/j.orggeochem.2007.04.006.

TAYLOR, K.W.R., HUBER, M., HOLLIS, C.J., HERNANDEZ-SANCHEZ, M.T., PANCOST, R.D. (2013). Re-evaluating modern and Palaeogene GDGT distributions: Implications for SST reconstructions. *Global and Planetary Change* **108**, 158–174. DOI: 10.1016/j.gloplacha.2013.06.011.

THIEL, V., HEIM, C., ARP, G., HAHMANN, U., SJÖVALL, P., LAUSMAA, J. (2007a). Biomarkers at the microscopic range: ToF-SIMS molecular imaging of Archaea-derived lipids in a microbial mat. *Geobiology* **5** (4), 413–421. DOI: 10.1111/j.1472-4669.2007.00119.x.

THIEL, V., TOPORSKI, J., SCHUMANN, G., SJÖVALL, P., LAUSMAA, J. (2007b). Analysis of archaeal core ether lipids using Time of Flight–Secondary Ion Mass Spectrometry (ToF-SIMS): Exploring a new prospect for the study of biomarkers in geobiology. *Geobiology* **5** (1), 75–83. DOI: 10.1111/j.1472-4669.2006.00093.x.

THUNELL, R.C. (1998). Particle fluxes in a coastal upwelling zone: sediment trap results from Santa Barbara Basin, California. *Deep Sea Research Part II: Topical Studies in Oceanography* **45** (8-9), 1863–1884. DOI: 10.1016/S0967-0645(98)80020-9.

THUNELL, R.C., TAPPA, E., ANDERSON, D.M. (1995). Sediment fluxes and varve formation in Santa Barbara Basin, offshore California. *Geology* **23** (12), 1083–1086. DOI: 10.1130/0091-7613(1995)023<1083:SFAVFI>2.3.CO;2.

TILJANDER, M., OJALA, A., SAARINEN, T., SNOWBALL, I. (2002). Documentation of the physical properties of annually laminated (varved) sediments at a sub-annual to decadal resolution for environmental interpretation. *Quaternary International* **88** (1), 5–12. DOI: 10.1016/S1040-6182(01)00068-4.

TRENBERTH, K.E. (1997). The definition of El Niño. *Bulletin of the American Meteorological Society* **78** (12), 2771–2778. DOI: 10.1175/1520-0477(1997)078<2771:TDOENO>2.0.CO;2.

VENRICK, E.L. (2012). Phytoplankton in the California Current system off southern California: Changes in a changing environment. *Progress in Oceanography* **104**, 46–58. DOI: 10.1016/j.pocean.2012.05.005.

VENRICK, E.L., REID, F.M.H., WEINHEIMER, A.L., LANGE, C.B., DEVER, E.P. (2006). Temporal patterns of the siliceous flux in the Santa Barbara Basin: The influence of North Pacific and local oceanographic processes. *California Cooperative Oceanic Fisheries Investigations Report* **47**, 156.

VERSTEEGH, G.J.M., BOSCH, H.-J., LEEUW, J.W. de (1997). Potential palaeoenvironmental information of C24 to C36 mid-chain diols, keto-ols and mid-chain hydroxy fatty acids; a critical review. *Organic Geochemistry* **27** (1-2), 1–13. DOI: 10.1016/S0146-6380(97)00063-6.

VOLKMAN, J.K. (1986). A review of sterol markers for marine and terrigenous organic matter. *Organic Geochemistry* **9** (2), 83–99. DOI: 10.1016/0146-6380(86)90089-6.

VOLKMAN, J.K., BARRETT, S.M., BLACKBURN, S.I., MANSOUR, M.P., SIKES, E.L., GELIN, F. (1998). Microalgal biomarkers: a review of recent research developments. *Organic Geochemistry* **29** (5), 1163–1179. DOI: 10.1016/S0146-6380(98)00062-X.

VOLKMAN, J.K., BARRETT, S.M., BLACKBURN, S.I., SIKES, E.L. (1995). Alkenones in *Gephyrocapsa oceanica*: Implications for studies of paleoclimate. *Geochimica et Cosmochimica Acta* **59** (3), 513–520. DOI: 10.1016/0016-7037(95)00325-T.

VOLKMAN, J.K., JOHNS, R.B., GILLAN, F.T., PERRY, G.J., BAVOR JR, H.J. (1980). Microbial lipids of an intertidal sediment—I. Fatty acids and hydrocarbons. *Geochimica et Cosmochimica Acta* **44** (8), 1133–1143. DOI: 10.1016/0016-7037(80)90067-8.

WAKEHAM, S.G. (1989). Reduction of stenols to stanols in particulate matter at oxic–anoxic boundaries in sea water. *Nature* **342** (6251), 787. DOI: 10.1038/342787a0.

WANG, Y., HENDY, I.L., NAPIER, T.J. (2017). Climate and anthropogenic controls of coastal deoxygenation on interannual to centennial timescales. *Geophysical Research Letters* **44** (22). DOI: 10.1002/2017GL075443.

WARREN, A.D., CONWAY, U., ARTHUR, C.J., GATES, P.J. (2016). Investigation of colloidal graphite as a matrix for matrix-assisted laser desorption/ionisation mass spectrometry of low molecular weight analytes. *Journal of Mass Spectrometry* **51** (7), 491–503. DOI: 10.1002/jms.3774.

WATROUS, J.D., DORRESTEIN, P.C. (2011). Imaging mass spectrometry in microbiology. *Nature Reviews Microbiology* **9** (9), 683. DOI: 10.1038/nrmicro2634.

WEIJERS, J.W.H., SCHOUTEN, S., VAN DEN DONKER, J.C., HOPMANS, E.C., SINNINGHE DAMSTÉ, J.S. (2007). Environmental controls on bacterial tetraether membrane lipid distribution in soils. *Geochimica et Cosmochimica Acta* **71** (3), 703–713. DOI: 10.1016/j.gca.2006.10.003.

WHITE, D.C., DAVIS, W.M., NICKELS, J.S., KING, J.D., BOBBIE, R.J. (1979). Determination of the sedimentary microbial biomass by extractible lipid phosphate. *Oecologia* **40** (1), 51–62. DOI: 10.1007/BF00388810.

WÖRMER, L., ELVERT, M., FUCHSER, J., LIPP, J.S., BUTTIGIEG, P.L., ZABEL, M., HINRICHS, K.-U. (2014). Ultra-high-resolution paleoenvironmental records via direct laser-based analysis of lipid biomarkers in sediment core samples. *Proceedings of the National Academy of Sciences of the United States of America* **111** (44), 15669–15674. DOI: 10.1073/pnas.1405237111.

WÖRMER, L., LIPP, J.S., HINRICHS, K.-U. (2015). Comprehensive analysis of microbial lipids in environmental samples through HPLC-MS protocols. In: *Hydrocarbon and Lipid Microbiology Protocols*. Springer, pp. 289–317.

WÖRMER, L., LIPP, J.S., SCHRÖDER, J.M., HINRICHS, K.-U. (2013). Application of two new LC–ESI–MS methods for improved detection of intact polar lipids (IPLs) in environmental samples. *Organic Geochemistry* **59**, 10–21. DOI: 10.1016/j.orggeochem.2013.03.004.

WÖRMER, L., WENDT, J., ALFKEN, S., WANG, J.-X., ELVERT, M., HEUER, V.B., HINRICHS, K.-U. (2019). Towards multiproxy, ultra-high resolution molecular stratigraphy: Enabling laser-induced mass spectrometry imaging of diverse molecular biomarkers in sediments. *Organic Geochemistry* **127**, 136–145. DOI: 10.1016/j.orggeochem.2018.11.009.

WUCHTER, C., SCHOUTEN, S., COOLEN, M.J.L., SINNINGHE DAMSTÉ, J.S. (2004). Temperature-dependent variation in the distribution of tetraether membrane lipids of marine Crenarchaeota: Implications for TEX_{86} paleothermometry. *Paleoceanography* (4). DOI: 10.1029/2004PA001041.

YEH, S.-W., KUG, J.-S., DEWITTE, B., KWON, M.-H., KIRTMAN, B.P., JIN, F.-F. (2009). El Niño in a changing climate. *Nature* **461** (7263), 511–514. DOI: 10.1038/nature08316.

YOUNGBLOOD, W.W., BLUMER, M. (1975). Polycyclic aromatic hydrocarbons in the environment: Homologous series in soils and recent marine sediments. *Geochimica et Cosmochimica Acta* **39** (9), 1303–1314. DOI: 10.1016/0016-7037(75)90137-4.

ZABEL, M., AIELLO, I., BECKER, K.W., BRAUM, S., BRODA, N., DIBKE, C., ELVERT, M., GAGEN, E.J., GOLDHAMMER, T., HEUER, V.B., HINRICHS, K.-U., KOCH, B.P., LAZAR, C., LIN, Y.-S., LIPP, J.S., MEADOR, T., PAPE, S., PETERS, C., SCHMAL, J., SCHMIDT, F., SCHRÖDER, J.M., TESKE, A., WENDT, J., WÖRMER, L., YOSHINAGA, M., ZHU, C., KNUTH, E., GOGOU, A., SCHÖN, A. (2012). Biogeochemistry and methane hydrates of the Black Sea; oceanography of the Mediterranean; Shelf sedimentation and cold water carbonates - Cruise No. M84/1 - February 09 – February 22, 2011 – Valletta (Malta) – Istanbul (Turkey). METEOR-Berichte, M84/1, 38 pp. *DFG-Senatskommission für Ozeanographie. DOI:* 10.2312/cr_m84_1.

ZAIMA, N., HAYASAKA, T., GOTO-INOUE, N., SETOU, M. (2010). Matrix-assisted laser desorption/ionization imaging mass spectrometry. *International journal of molecular sciences* **11** (12), 5040–5055. DOI: 10.3390/ijms11125040.

ZHU, C., LIPP, J.S., WÖRMER, L., BECKER, K.W., SCHRÖDER, J.M., HINRICHS, K.-U. (2013). Comprehensive glycerol ether lipid fingerprints through a novel reversed phase liquid chromatography–mass spectrometry protocol. *Organic Geochemistry* **65**, 53–62. DOI: 10.1016/j.orggeochem.2013.09.012.

ZHU, C., WAKEHAM, S.G., ELLING, F.J., BASSE, A., MOLLENHAUER, G., VERSTEEGH, G.J.M., KÖNNEKE, M., HINRICHS, K.-U. (2016). Stratification of archaeal membrane lipids in the ocean and implications for adaptation and chemotaxonomy of planktonic archaea. *Environmental Microbiology* **18** (12), 4324–4336. DOI: 10.1111/1462-2920.13289.

ZOLITSCHKA, B., FRANCUS, P., OJALA, A.E.K., SCHIMMELMANN, A. (2015). Varves in lake sediments – a review. *Quaternary Science Reviews* **117**, 1–41. DOI: 10.1016/j.quascirev.2015.03.019.